A Three-Dimensional Biphasic Finite Element Contact Formulation for Hydrated Soft Tissue

by

Taiseung Yang

A Thesis Submitted to the Graduate
Faculty of Rensselaer Polytechnic Insitute
in Partial Fulfillment of the
Requirements for the Degree of
DOCTOR OF PHILOSOPHY
Major Subject: Mechanical Engineering

Approved by the
Examining Committee:

_____
Robert L. Spilker, Thesis Advisor

_____
John A. Tichy, Member

_____
Mark S. Shephard, Member

_____
Mark H. Holmes, Member

Rensselaer Polytechnic Insitute
Troy, New York

December 2003
(For Graduation December 2003)

© Copyright 2003

by

Taiseung Yang

All Rights Reserved

Table of Contents

Page

Table of Contents ..... **iii**
List of Tables ..... **vi**
List of Figures ..... **viii**
Acknowledgement ..... **xiv**
Abstract ..... **xvi**
Chapter 1: Introduction **1**
1.1 Prologue 1
1.2 Tissue Modeling 2
1.2.1 Articular Cartilage 2
1.2.2 Constitutive Model 3
1.2.3 Contact Model 4
1.3 Finite Element Analysis 6
1.3.1 Selecting FE Formulation for Biphasic Analysis 7
1.3.2 Selecting the Contact Treatment 9
1.4 Summary and Layout of the Thesis 11
Chapter 2: Governing Equations for Biphasic Contact **13**
2.1 Introduction 13
2.2 Kinematics of Biphasic Mixture 13
2.3 Linear Biphasic Equations for Contact Problems 16
2.3.1 Continuity of Solid Displacement 18
2.3.2 Balance of Mass 20
2.3.3 Balance of Linear Momentum 21
2.3.4 Balance of Energy 22
2.4 Constitutive Equations for Biphasic Mixture 23
2.5 Frictionless Contact 25

2.6 Summary of the Governing Equations and Boundary Conditions..... 29
Chapter 3: Finite Element Contact Formulation and Numerical Implementation 32
3.1 Introduction..... 32
3.2 Weighted Residual Statement..... 32
3.2.1 Trial and Weighting Function Spaces..... 34
3.2.2 Weak Form..... 35
3.2.3 Finite Element Matrix Equation..... 38
3.2.4 An Alternative Kinematic Variable Based Formulation..... 44
3.3 Contact Element Matrix Calculations and Contact Iteration..... 48
3.4 Contact Search Algorithm..... 52
Chapter 4: A Biphasic Contact Patch Test to Select the Interpolation Functions for the Lagrange Multipliers..... 53
4.1 Introduction..... 53
4.2 Biphasic Contact Patch Test..... 54
4.3 Selecting Interpolating Functions for Lagrange Multipliers..... 56
4.3.1 Continuous Interpolating Functions..... 64
4.3.2 Discontinuous Interpolating Functions..... 72
4.4 Biphasic Patch Test for the Alternative Kinematic Variable Based Formulation..... 78
4.5 Contact Element Matrix Calculations for Non-matching Meshes..... 81
Chapter 5: Evaluation of Iterative Solution Methods for Linear Biphasic Problems 91
5.1 Introduction..... 91
5.2 Iterative Methods..... 92
5.2.1 *Krylov* Subspace Methods..... 92
5.2.2 Incomplete LU Factorization Preconditioners..... 94
5.2.3 Equation Reordering Methods..... 95
5.3 Example Problems and Numerical Results..... 96
5.3.1 Without Fill-in..... 99
5.3.2 With Fill-in..... 105
Chapter 6: Three-Dimensional Biphasic Contact Problems..... 112

6.1 Introduction 112
6.2 Confined Compression Test 113
6.2.1 CC Creep 117
6.2.2 CC Stress Relaxation 122
6.3 Unconfined Compression Test 123
6.4 Hertz Contact 130
6.5 Biphasic Indentation Test 133
6.5.1 Analysis using a Flat-Ended Cylindrical Indenter 133
6.5.2 Analysis using with a Cylindrical Ended Indenter 141
6.6 Gleno-Humeral Joint (GHJ) Contact 146
Chapter 7: Summary, Concluding Remarks and Future Study 151
7.1 Summary and Concluding Remarks 151
7.2 Suggestions for Future Study 154
References 156

List of Tables

Page

Table 4. 1 Mesh configurations for the biphasic contact patch test. 56
Table 4. 2 A summary of the conditions (i), (ii) and (iii) of the interpolating functions for Lagrange multipliers for the primary variable based formulation. 63
Table 4. 3 Conditions (i), (ii) and (iii) for continuous interpolations for Lagrange multipliers (asterisk * indicates violation of the condition)..... 66
Table 4. 4 Conditions (i), (ii) and (iii) for discontinuous interpolations for Lagrange multipliers (asterisk * indicates violation of the condition)..... 73
Table 4. 5 Conditions (i), (ii) and (iii) for continuous interpolations for Lagrange multipliers with the 'kinematic variable based' formulation (asterisk * indicates violation of the condition)..... 79
Table 4. 6 Conditions (i), (ii) and (iii) for discontinuous interpolations for Lagrange multipliers with the 'kinematic variable based' formulation (asterisk * indicates violation of the condition)..... 80
Table 4. 7 Test cases of the biphasic contact patch tests for non-matching meshes..... 84
Table 5. 1 Description of coefficient matrices from increasingly refined meshes for the biphasic finite element formulation. 98
Table 5. 2 Required number of iterations to solve the test matrices using incomplete LU preconditioning with no fill-in ILU(0). A $*$ indicates that the convergence criteria was not satisfied within 500 iterations. 99
Table 5. 3 Number of flops (the exponent for each mesh case is shown in parentheses) to solve the linear systems using an ILU(0) preconditioner. A $*$ indicates that the convergence criteria was not satisfied within 500 iterations. 103
Table 5. 4 Required number of iterations to solve the linear systems using alternate Krylov methods and ILU(1) preconditioning. 106

Table 5. 5 Number of flops (the exponent for each mesh case is shown in parentheses) to solve the linear systems using alternate Krylov methods and ILU(1) preconditioning. 107
Table 5. 6 Fill ratio of ILU(k) and required number of iteration using BiCGSTAB for MESH4 matrix. 109
Table 6. 1 Geometric and material properties for GHJ. 147

List of Figures

Page

Figure 2.1 Definition of terms for the kinematics of a biphasic mixture..... 15

Figure 2.2 A contact system of two biphasic bodies at t_o and $t > 0$. 17

Figure 2.3 A mixture contact system containing a surface of discontinuity Γ_C 18

Figure 2.4 Decomposition of the traction vector at a point on body 'A' into the normal and tangential components..... 26

Figure 3.1 Finite element discretization with tetrahedral and contact elements for the 3D v-p contact formulation (solid circle represents solid velocity DOF, and hollow circle represents pressure DOF). 48

Figure 3. 2 The closest point projection from a Gauss quadrature point on the contactor surface (on Body 'A') to the target surface (on Body 'B'). 49

Figure 3.3 A contact iteration algorithm for the biphasic contact analysis. 51

Figure 4. 1 (a) The original contact patch test, (b) A biphasic contact patch test in 3D.. 54

Figure 4. 2 Meshes on the contact surface for (a) MESH A, (b) MESH B, (c) MESH C and (d) MESH D. 56

Figure 4. 3 (a) Gradient of element displacement field, (b) Gradient of element pressure field in the Taylor Hood element. 58

Figure 4. 4 Singularity check for the continuous interpolations for λ^f and λ^s (a solid circle represents a DOF of a primary variable, and a hollow circle represents a DOF of Lagrange multiplier variables) (a) MESH A, (b) MESH B, (c) MESH C and (d) MESH D..... 65

Figure 4. 5 (a) u_z, (b) σ_{zz}^E, (c) p and (d) $-\kappa p_{,z} n_z$ on the contact surfaces using continuous interpolations for Lagrange multipliers with MESH A (units are mm for displacement, MPa for normal stress and pressure, mm/sec for relative fluid velocity). 68

Figure 4. 6 (a) u_z, (b) σ_{zz}^E, (c) p and (d) $-\kappa p_{,z} n_z$ on the contact surfaces using continuous interpolations for Lagrange multipliers with MESH B (units are mm for displacement, MPa for normal stress and pressure, mm/sec for relative fluid velocity). 69

Figure 4. 7 (a) u_z, (b) σ_{zz}^E, (c) p and (d) $-\kappa p_{,z} n_z$ on the contact surfaces using continuous interpolations for Lagrange multipliers with MESH C (units are mm for displacement, MPa for normal stress and pressure, mm/sec for relative fluid velocity). 70

Figure 4. 8 (a) u_z, (b) σ_{zz}^E, (c) p and (d) $-\kappa p_{,z} n_z$ on the contact surfaces using continuous interpolations for Lagrange multipliers with MESH D (units are mm for displacement, MPa for normal stress and pressure, mm/sec for relative fluid velocity). 71

Figure 4. 9 Singularity check for the discontinuous interpolations for λ^f and λ^s (a solid circle represents a DOF of a primary variable, and a hollow circle represents a DOF of Lagrange multiplier variables) (a) MESH A, (b) MESH B, (c) MESH C and (d) MESH D..... 72

Figure 4. 10 (a) u_z, (b) σ_{zz}^E, (c) p and (d) $-\kappa p_{,z} n_z$ on the contact surfaces using discontinuous interpolations for Lagrange multipliers with MESH A (units are mm for displacement, MPa for normal stress and pressure, mm/sec for relative fluid velocity). 74

Figure 4. 11 (a) u_z, (b) σ_{zz}^E, (c) p and (d) $-\kappa p_{,z} n_z$ on the contact surfaces using discontinuous interpolations for Lagrange multipliers with MESH B (units are mm for displacement, MPa for normal stress and pressure, mm/sec for relative fluid velocity). 75

Figure 4. 12 (a) u_z, (b) σ_{zz}^E, (c) p and (d) $-\kappa p_{,z} n_z$ on the contact surfaces using discontinuous interpolations for Lagrange multipliers with MESH C (units are mm for displacement, MPa for normal stress and pressure, mm/sec for relative fluid velocity). 76

Figure 4. 13 (a) u_z, (b) σ_{zz}^E, (c) p and (d) $-\kappa p_{,z} n_z$ on the contact surfaces using discontinuous interpolations for Lagrange multipliers with MESH D (units are mm for displacement, MPa for normal stress and pressure, mm/sec for relative fluid velocity). 77
Figure 4. 14 A simple 2D contact example with non-matching mesh: (a) body II as a contactor, (b) body I as a contactor. 81
Figure 4. 15 Non-matching meshes between two contacting surfaces: (a) 2 elements on body I and 4 elements on body II, (b) 32 elements on body I and 30 elements on body II. 84
Figure 4. 16 Distributions of strain, ε_{zz}, on the contacting surfaces for (a) Case 1, (b) Case 2, (c) Case 3 and (d) Case 4. 87
Figure 4. 17 Distributions of strain, ε_{zz}, on the contacting surfaces for (a) Case 5, (b) Case 6, (c) Case 7 and (d) Case 8. 88
Figure 4. 18 (a) u_z, (b) σ_{zz}^E, (c) p and (d) $-\kappa p_{,z} n_z$ on the contact surfaces for Case 8 (units are mm for displacement, MPa for normal stress and pressure, mm/sec for relative fluid velocity). 89
Figure 5. 1 A schematic of the test problem representing the humeral head cartilage layer in the human shoulder. 97
Figure 5. 2 The L_2 norm of the residual for each Krylov subspace method using one-way dissection reordering for case MESH4. 101
Figure 5. 3 Decrease in the L_2 norm of the residual for the matrix reordering methods using BiCGSTAB Krylov method for case MESH4. 101
Figure 5. 4 Elapsed wall-clock time to solve the linear systems using alternate Krylov subspace methods with one-way dissection reordering. 104
Figure 5. 5 Elapsed wall-clock time to solve the linear systems using BiCGSTAB with alternate matrix reorderings. 105
Figure 5. 6 Improvement of convergence rate using higher level of fill-in using BiCGSTAB and one-way dissection reordering for case MESH4. 108
Figure 5. 7 Fill ratio and memory requirement versus level of ILU(k) fill-in using BiCGSTAB and one-way dissection reordering for case MESH4. 110

Figure 5. 8 Elapsed wall-clock time for preconditioning and iterative solution using BiCGSTAB and one-way dissection, versus level of fill in, for case MESH4..... 111
Figure 6. 1 (a) A schematic of the uni-axial confined compression test, (b) traction boundary condition for a creep test, (c) displacement boundary condition for a stress relaxation test. 115
Figure 6. 2 Finite element meshes of (a) 420 tetrahedral elements with 24 matching contactor elements, (b) 363 tetrahedral elements with 32 (left) and 30 (right) contact elements. 116
Figure 6. 3 (a) Normalized displacement in the confined compression creep test at the top of tissue in time (b) normalized displacement through the depth at t = 50, 500 and 1000 sec. 118
Figure 6. 4 Normalized pressure through the depth in the confined compression creep test at t = 50, 500 and 1000 sec. 118
Figure 6. 5 Continuity conditions of (a) solid displacement u_z^s, (b) pressure from the matching and non-matching contact elements in the confined compression creep test. 119
Figure 6. 6 Continuity conditions of solid stress σ_{zz}^s (a) for matching mesh, (b) for non-matching mesh, and of relative fluid velocity $W_z = -\kappa p_{,z}$ (c) for matching mesh, (d) for non-matching mesh in the confined compression creep test. 121
Figure 6. 7 (a) Normalized pressure in the confined compression stress relaxation test through the depth at t = 50 and 500 sec., (b) normalized pressure in time at z/h = 0, 0.5, 0.875..... 122
Figure 6. 8 A schematic of the perfectly lubricated unconfined compression stress relaxation test of a cylindrical disk of hydrated soft tissue..... 123
Figure 6. 9 Finite element meshes for (a) single tissue test with 1994 tetrahedral elements and for (b) contact test with 1639 tetrahedral and 138 contactor elements 125
Figure 6. 10 Solid velocity in radial direction at the mid-height of the outer surface for the unconfined compression stress relaxation test. (time is normalized by t_o = 500 sec.) 127

Figure 6. 11 Solid velocity in axial direction across the contact surface at 250 sec. for the unconfined compression stress relaxation test. 128
Figure 6. 12 (a) Fluid pressure and solid stresses, (b) relative fluid velocity across the contact surface at 250 sec. for the unconfined compression stress relaxation test. 129
Figure 6. 13 (a) A schematic of Hertz contact problem (b) finite element mesh 131
Figure 6. 14 (a) Distribution of displacement, (b) Deformed surface geometry for 0.01 mm displacement of the spherical indenter. 132
Figure 6. 15 (a) Distribution of strain, (b) Distribution of stress (in MPa) for 0.01 mm displacement of the spherical indenter. 132
Figure 6. 16 (a) A schematic of the biphasic indentation test with a flat-ended cylindrical indenter, (b) The finite element mesh with 14647 tetrahedral elements and 294 contact elements. 134
Figure 6. 17 (a) Axial strain and (b) axial stress along the radial position at several depths at 500 sec. in the biphasic indentation test with a flat-ended cylindrical indenter. 135
Figure 6. 18 Pressure along the radial position at several depths at 500 sec. in the biphasic indentation test with a flat-ended cylindrical indenter. 136
Figure 6. 19 (a) Displacement distribution in mm and (b) comparison of displacement on contact surfaces at 250 sec. in the biphasic indentation test with a flat-ended cylindrical indenter. 137
Figure 6. 20 Pressure distribution in MPa and (b) comparison of pressure on contact surfaces at 250 sec. in the biphasic indentation test with a flat-ended cylindrical indenter. 137
Figure 6. 21 Solid stress σ_{zz}^{s} distribution in MPa and (b) comparison of solid stress on contact surfaces at 250 sec. in the biphasic indentation test with a flat-ended cylindrical indenter. 138
Figure 6. 22 Relative fluid velocity $W_z = -\kappa p_{,z}$ distribution in mm/sec and (b) comparison of relative fluid velocity on contact surfaces at 250 sec. in the biphasic indentation test with a flat-ended cylindrical indenter. 138
Figure 6. 23 Displacement through the depth (a) for both the cartilage and the indenter, (b) only for the indenter. 140

Figure 6. 24 Pressure through the depth (a) for both the cartilage and the indenter, (b) only for the indenter. 141
Figure 6. 25 A schematic of the biphasic indentation test with a cylindrical ended indenter. 142
Figure 6. 26 (a) Displacement (in mm) on the deformed configuration and (b) deformed surface at 100 sec. in the biphasic indentation test with a cylindrical ended indenter. 143
Figure 6. 27 Pressure distribution (in MPa) on the deformed configuration for the biphasic indentation at 100 sec. in the biphasic indentation test with a cylindrical ended indenter. 143
Figure 6. 28 Normal traction distributions (in MPa) at 100 sec. in the biphasic indentation test with a cylindrical ended indenter. 144
Figure 6. 29 (a) Maximum and (b) minimum principal stresses in MPa at 100 sec. in the biphasic indentation test with a cylindrical ended indenter. 145
Figure 6. 30 Model geometry and a finite element mesh for glenoid and humeral head cartilages. 147
Figure 6. 31 Displacement (in mm) on the deformed geometry in the GHJ at 5 and 10 sec. of 0.2 mm compressive displacement. 148
Figure 6. 32 Pressure distribution (in MPa) in the GHJ on the deformed geometry at 10 sec. of 0.2 mm compressive displacement. 149
Figure 6. 33 Maximum principal elastic stress in MPa in the GHJ at 10 sec. of 0.2 mm compressive displacement. 150
Figure 6. 34 Minimum principal elastic stress in MPa in the GHJ at 10 sec. of 0.2 mm compressive displacement. 150

Acknowledgement

I am greatly indebted to my thesis advisor, Sc. D. Robert L. Spilker for kindly providing a comprehensive guidance throughout the development of this study. He has been generous and patient of my slow progress and mistakes, and encouraged and eventually guided me up to this point. I wish to give my sincere thanks to him.

I would like to express my gratitude to my other committee members, Ph. D. John A. Tichy in Mechanical Engineering, Ph. D. Mark S. Shephard in Civil Engineering and Ph. D. Mark H. Holmes in Applied Mathematics. They have provided invaluable suggestions and advice for my research work.

I am grateful to my former lab-mates of the Computational Biomechanics Laboratory, Peter Donzelli, Echo Miller, and Kerem Un and Michael Macri. It has been a great pleasure to share the lab with them. Exchanging thoughts and ideas on many academic subjects have expedited our common goals. And, intermittent chatting on various social issues was enjoyable and also helpful to improve my English skill.

I wish to express my special thanks to Pete who passed away one year after I came to the lab. Although I have not spent much time with him, the gifted individual inspired me in many aspects of life. As a professor, colleague and friend, he will be greatly missed for a long time.

I acknowledge Dupre Christophe, Suleyman Kocak and other students in the Scientific Computation Research Center (SCOREC) for their technical support. I also

acknowledge all Korean Student Association (KSA) members at Rensselaer Polytechnic Institute for their friendship.

Lastly but certainly not least, I have been always indebted to love and caring of my family. I could not have survived the last seven years in the United States without their support in many ways. I am very anxious to face them all together, and also anxious to start my new career in Korea. Finally, I would like to thank all whose direct and indirect support helped me completing my thesis.

Abstract

A fully three-dimensional contact finite element formulation has been developed for the biological soft tissue-to-tissue contact analysis. The linear biphasic theory of Mow *et at*., based on continuum mixture theory, is adopted to describe the hydrated soft tissue as the continua of solid and fluid phases. Four contact continuity conditions derived for biphasic mixtures by Hou *et al*. are introduced on the assumed contact surface. Under the assumption of small deformation and frictionless contact, the governing differential equations and boundary conditions represent the strong form of problem.

The Galerkin weighted residual method has been applied to this strong form to derive alternate velocity-pressure finite element contact formulations. The Lagrange multiplier method is used, and enforces two of the four contact continuity conditions, while the other two conditions are introduced directly into the weighted residual statement. The alternate formulations differ in the choice of continuity conditions to enforce with Lagrange multipliers. In one they enforce the normal solid traction and relative fluid flow continuity conditions on the contact surface, and in the other the multipliers enforce normal solid traction and pressure continuity conditions. The contact nonlinearity is treated with an iterative algorithm, where the assumed area is either extended or reduced based on the validity of the solution relative to contact conditions such as impenetrability and intensility. The resulting first order system of equations is solved in time using the generalized finite difference scheme.

In an independent study, various combinations of the Krylov iterative solvers have been tested with alternate equation re-ordering schemes and levels of pre-conditioning. An extensive study has been performed using the 3D linear biphasic equations, without contact, the results of which have provided guidance for efficiently solving the symmetric indefinite system found in the present v-p contact formulations.

A biphasic contact patch test has been used to select interpolation functions for the Lagrange multipliers and to confirm that the formulations are capable of transmitting the constant normal traction as a finite element completeness check. Then, the preferred formulation has been validated by a series of increasingly complex canonical problems including the confined and unconfined compression tests, the Hertz contact problem and two biphasic indentation tests. As a clinical demonstration of the capability of the contact analysis, the gleno-humeral joint contact of human shoulders has been analyzed using an idealized 3D geometry. In the joint, both glenoid and humeral head cartilage experience maximum tensile and compressive stresses at the cartilage-bone interface, away from the center of the contact area.

Chapter 1: Introduction

1.1 Prologue

The history of *Biomechanics*, *mechanics* applied to *biology*, goes back to around 300 B.C. when the science of body movement called *Kinesiology* was first discoursed. This study paid a broad attention on structures and functions of the living creature such as; 'movement of animals' by Aristotle (384-322 B.C.), 'the hydrostatic principles governing floating bodies' by Archimedes (287-212 B.C.), 'health and scientific hygiene' by Galen (131-201 B.C.), and so forth. Since this early study, many scientists have directed their efforts to the understanding of the normal functions of living things or their organs, so called *physiology*. More recently, emphasis has been given by biomechanical engineers to a continuum approach in the science of physiology. In this approach, the functions of human organs are described by mathematical models, and then solved by analytical and numerical procedures.

As a natural consequence of the improved understanding of function, the average life expectancy of our generation is extended, and organs are expected to keep their normal functionalities for more years. However, failure (degeneration or degradation) is often found due to aging, abnormal use or injury. Articular cartilage is one of the sites where failures such as osteoarthritis (OA) are observed. Before the proper treatment is applied, the functionalities of cartilage should be fully understood first. As a

biomechanical engineer, in this study, mechanical response of articular cartilage contact is of the main concern.

1.2 Tissue Modeling

In the recent history of biomechanics, researchers have tried to develop precise mathematical models for soft tissues of the human body. Early attention has been given to blood vessels and muscles, and later on, to bone and articular cartilage. Fung describes the development of tissue modeling in his survey article [25], and provides a sequence of physiological problems and examples of biomechanics in a textbook [26]. In the next subsections, discussion is presented on articular cartilage, its constitutive model and the contact model.

1.2.1 Articular Cartilage

Articular cartilage is an avascular, aneural, connective tissue that covers articulating (sometimes called diathrodial or synovial) joints such as the knee, shoulder, etc. It is normally white and 1 to 6 millimeter thick [59, 75, 89]. Unlike ordinary engineering materials, articular cartilage is multi-phase, non-homogeneous, and anisotropic. Its fluid component, called interstitial fluid or synovial fluid, is non-Newtonian, and the solid component behaves beyond the limit of a Hookean assumption. For normal cartilage, the fluid content ranges from 60 to 85 % of its total wet weight. The remaining wet weight of cartilage is occupied by two major structural macromolecular materials, collagen (15 to 22 %), proteoglycan (4 to 7 %), and several other molecules such as lipid, phospholipid, protein, and glycoprotein. Details on the

macro and micro structure and the composition of articular cartilage can be found in literature [29, 68] .

This soft tissue shows superior characteristics of load bearing, friction, lubrication and wear. Under normal physiological loading conditions, articular cartilage may last more than 8 or 9 decades without severe wear and tear [55]. Several theories explain how the tissue behaves so efficiently. McCutchen [56] advocates *Fluid Transport Effects* such that the synovial fluid carries initial loading and takes long time to squeeze out, and that the compressed cartilage rebounds quickly when the loading is removed. In addition to the load bearing role, the fluid in cartilage reduces frictional effects. MacConaill [52] explains *Fluid Lubrication Effect* where the highly viscous synovial fluid between contacting cartilages is considered to experience high pressure and support the loading. For more accurate representation of the cartilage contact, further research is needed.

1.2.2 Constitutive Model

In early studies in biomechanics, articular cartilage was modeled as a conventional single phase elastic material [31, 45]. From a two-phase perspective, this single phase model is only meaningful at equilibrium when flow stops, the fluid pressure decays and all the load is carried by the solid phase of the tissue. But it is a rare case in physiological loading conditions where events occur at much shorter times. As the elastic model could not describe the time-dependent response of the tissue, a viscoelastic model was suggested by some researchers [30, 66]. However, the model was still not able to explain the transient stresses resulting from the interstitial fluid inside the tissue. In order to include the fluid effects into cartilage deformation, Mow *et al*. [58] developed

the *biphasic theory* based on the mixture theory by Truesdell and Toupin [82]. In the biphasic theory, the hydrated soft tissue is modeled as an immiscible binary mixture of two continua: an intrinsically incompressible elastic solid phase representing collagen and proteoglycan, and an intrinsically incompressible inviscid fluid phase representing the interstitial fluid. This model describes well the apparent viscoelastic behavior by the interaction between the solid and fluid phases, and has been validated from experimental data for cartilage under various loading conditions [2, 59].

Later, the biphasic theory was extended to include nonlinearities resulting from finite deformation [46, 60, 80], strain-dependent permeability [34, 48], intrinsic solid phase viscoelasticity [53] and a hyperelastic [16] solid phase.

Lai *et al*. [49] proposed the *triphasic theory* that includes an additional ion phase, representing cation and anion concentrations of a single salt, to predict the swelling of articular cartilage. The theory explains that the applied compressive stress is shared by Donnan osmotic pressure and chemical expansion stress along with elastic stress of the solid phase. Recently, Huyghe et al. [39] extended the theory into the *quadriphasic theory* where cations and anions of the ion phase are considered as independent phases to appreciate electrical effects such as electro-osmosis and streaming currents.

1.2.3 Contact Model

For most contact problems, the contact area and distribution of the traction over the area are unknown prior to analysis. They are intrinsically nonlinear such that the contact boundary conditions change under deformation, and must be determined as a part of the solution. For this reason, closed form solutions are generally not available except

for a few simple problems. Hertz [33] developed the first analytic contact solutions for elastic solid contact problems under certain assumptions: (i) contacting surfaces are continuous and non-conforming, (ii) small strain, (iii) frictionless contact and (iv) each solid should be considered as an elastic half-space where the stresses away from contact surface are negligible. Due to these restrictions, his solution is not directly applicable to many practical problems.

In biomechanics, researchers have developed contact models to simulate contact of articulating joints. Most of the early works are, however, restricted to elastic models or incapable of fully nonlinear contact analysis for physiologic situations. Eberhardt *et al*. [21] proposed an analytical model for frictionless elastic contact. The model is used to predict the failure site of cartilage by high stresses that are considered as a function of the ratio of contact radius to total tissue thickness (a/h). But, neglecting the role of interstitial fluid results in a lack of agreement with experimental observations. Ateshian *et al*. [3] approximated a closed-form analytical solution using an asymptotic approach for solving joint contact problems. The solution concludes that the fluid phase of cartilage plays a crucial role in load support during the first 100-200 sec after contact loading. Also, the analysis supports the hypothesis that cartilage failure due to a sudden loading occurs at the cartilage-bone interface in either parallel or perpendicular direction to this interface.

Hou *et al*. [36] developed contact boundary conditions at the interface between a biphasic mixture and a Newtonian (or Non-Newtonian) fluid to simulate cartilage-to-cartilage lubrication. In synovial joints, the interstitial fluid in cartilage has relatively low viscosity, while the synovial fluid between cartilage layers has a high viscosity. They

conclude, under these conditions, the fluid transport is not likely to be rapid in the cartilage layer, and that the lower viscous interstitial fluid enhances the fluid flow in cartilage. Later, they observed that the applied load through a thin film is distributed on cartilage according to the volume fractions [37]. Using the contact boundary conditions by Hou *et al.* [36] and a linear form of the biphasic theory, Donzelli [18] has developed a finite element formulation to implement 2D axisymmetric contact between hydrated soft tissues. The validity of the formulation is verified through several canonical examples for evolving biphasic contact problems. Then he used axisymmetric models to solve some clinical applications such as the gleno-humeral joint of the shoulder and the meniscus of the knee joint.

1.3 Finite Element Analysis

Although the biphasic theory accurately represents the mechanical response of hydrated soft tissue, the analytical solution is not often available under physiologically meaningful conditions. This is more evident when contact analysis is involved. Also, experimental studies have certain limitations such that data acquisition is extremely difficult at some clinically interesting sites. Hence, numerical techniques can be used as an alternative method, or in conjunction with experimental studies, to study the behavior of cartilage in human joints. The finite element method, in particular, has been widely used to solve the governing partial differential equations for these problems.

The standard procedure of the finite element method leads to a linear algebraic system, $\boldsymbol{Ax} = \boldsymbol{b}$. In general, direct solution methods like Gauss Elimination are effective only for small systems due to their robustness. However, they become prohibitive to

solve large sparse systems that are often observed for 3D analysis on complex geometries. As Givoli [27] listed the *Iterative Linear Algebraic Solvers* as the second most important method in computational mechanics in 20th century (FEM is listed as the first), they are extremely important in many practical finite element analyses. Among many iterative solution techniques, *Krylov subspace methods* have been widely used for the last couple of decades along with hardware capability improvement. Surveys and extensive experimental studies on *Krylov* methods for the current formulation are presented in Chapter 5.

1.3.1 Selecting FE Formulation for Biphasic Analysis

Finite element formulations for mixture were first developed in soil mechanics based on the Biot's poroelastic theory [11, 12]. Recently, many researchers proposed FE formulations to study a quasi-static analysis of biphasic continua. Depending on the enforcement of the continuity equation on the weighted residuals, three broad groups of finite element formulation have been developed and available for biphasic problems: the penalty or mixed-penalty formulation [77, 78, 80], the mixed *v-p* formulation [63, 88, 1], and the hybrid formulation [87].

In the penalty method by Suh [80], a penalized form of the continuity equation is used to eliminate pressure as an independent variable. In this formulation, solid and fluid velocities are the primary variables and pressure and stresses can be calculated from them. For a two dimensional analysis, non-rectangular quadrilateral elements based on the formulation give very poor results especially for fluid velocity. To overcome this shortcoming for irregular geometries, Spilker and Maxian [77] choose a six-node

triangular element from the mixed-penalty formulation where the penalty term is introduced into the weighted residual statement. However, since this formulation keeps both solid/fluid velocities and pressure as primary variables, it is not attractive for large three-dimensional analysis. Also, this kind of formulation requires a discontinuous pressure interpolation between elements.

The hybrid methods are a special class of mixed methods. But they are different in the sense that the kinetic variables such as pressure and stresses are forced to satisfy an equilibrium relation [76]. While the kinetic variables are represented as the derivatives of the kinematic variables in conventional methods, the hybrid method specifies the kinetic variables through independent interpolations. Although Vermilyea [87] reports a better convergence rate for the hybrid element than that for mixed-penalty elements, computational cost of this approach seems to be too expensive to constitute a strain-stress relation. This type of method is also found in the solution of incompressible fluid flow [90].

In the velocity-pressure (*v-p*) formulation, the fluid velocity is eliminated from the governing equations using the linear momentum for the fluid phase. Since the scalar variable of pressure substitutes for the vector variables of fluid velocity, the assembled global matrix results in the smaller number of degrees of freedom. Almeida [1] notes that 2D and 3D elements used in the formulation are more robust than those in the mixed-penalty formulation for confined compression creep problem. However, Almeida [1] and Wayne [88] observe that the solution contains spatial oscillation near the loaded surface at early time steps. The *v-p* formulation and its variant, the displacement-pressure (*u-p*) formulation, have been widely used in soil mechanics [57, 72] and biomechanics [63, 88].

Among the above, the velocity-pressure (v-p) formulation is chosen for the present contact analysis because of its advantage of computational efficiency.

1.3.2 Selecting the Contact Treatment

Much effort has been devoted to developing solution methods for contact problems using the finite element method. They are successful in many applications, from the classical manufacturing process such as metal forming and machining, as well as for automobile crash simulations, fluid-solid interactions, and the analysis of human joint systems. In finite element contact methods, two of main issues are the contact search algorithms and the methods used to enforce the interface boundary conditions. Recently, the first issue attracted increasing attention in order to reduce excessive computing time. For large finite element analyses with a fine mesh, as much as 50 percent of the total CPU time is spent in contact detections [32]. Consequently, many algorithms have been proposed in the last decade [32, 61, 62, 9, 64].

In order to satisfy the contact constraints, three types of methods have been widely used: the penalty method, Lagrange multiplier method, and augmented Lagrange method. In general, the interface boundary conditions for a single phase contact problem consist of the Kuhn-Tucker inequality conditions [51] and the equality conditions for displacement and traction. Unlike a single phase problem, there are two more additional equality conditions on relative fluid flow and pressure in the biphasic contact problem. Therefore, it is not viable to directly adopt one of the above three methods for biphasic mixture contact. Donzelli [18] proposed a mixed-penalty contact formulation using Lagrange multipliers for two-dimensional biphasic contact analysis. In his formulation,

equality constraints are introduced into the weighted residual; the two constraints on kinematic variables are introduced directly into the weighted residual, and other two constrains on kinetic variables are satisfied using Lagrange multipliers as the additional variables. He used an iterative technique to eliminate physically unacceptable solutions that violate the inequality constraints.

The penalty method could be another choice with the advantage that there is no additional variable leading to additional unknowns. In that method, the kinetic variables such as traction and pressure are deduced from a product of the penalty parameter and the corresponding kinematic constraints. Increasing the penalty number results in a more accurate satisfaction of constraints. As the penalty parameters goes to infinity, the kinematic constraints are exactly satisfied. Realistically, for a finite value of penalty parameter, the kinetic variables are proportional to the violation of the kinematic constraints. Inevitably, this causes ill-conditioning of the global system, which is problematic at the solution stage with both direct and iterative methods.

The augmented Lagrange method combines good features from the penalty and Lagrange multiplier methods. This method includes both the penalty parameter and the Lagrange multiplier, but the latter is not an additional variable any more. The initial guess for the multiplier is closely determined to the defined quantity over iterations with a relatively small penalty parameter. This improves the ill-conditioning compared with the penalty method. However, the additional iterative scheme might be expensive with the contact iteration for the correct contact surface determination. Also, for nonlinear problems in future studies, since another nonlinear iteration procedure nested within those two iterations might be unduely demanding. Consequently, the Lagrange multiplier

method is chosen and the general idea in Donzelli [18] is followed to develop the current formulations.

1.4 Summary and Layout of the Thesis

In summary, clinically important problems involving the biomechanical responses of soft hydrated tissues, like cartilage, in human diarthrodial joints involve 3D contact of deformable biphasic tissues over complex 3D physiological geometries. To date, analyses of soft tissue contact have involved approximations such as axisymmetric geometry, single phase materials, estimates of contact traction based on rigid overlap of layers. This thesis aims to take the first steps toward more realistic 3D contact analysis by developing and validating a finite element formulation for 3D contact of linear biphasic tissues. The organization of the thesis is briefly summarized next.

Chapter 2 presents a brief overview of the biphasic model and presents the governing equations and boundary conditions for mixture contact analysis. Contact constraints by Hou *et al*. [36] are simplified for the frictionless contact assumption used in this study. The initial boundary value problem is summarized in the strong form at the end.

In Chapter 3, a finite element formulation is derived using Galerkin weighted residual methods. The *v-p* formulation is used for biphasic theory, and Lagrange multiplier constraints are used to satisfy contact constraints. Numerical integration of the contact contributions and contact iteration technique are described.

In Chapter 4, a biphasic contact patch test is suggested for the finite element completeness check. The interpolating functions for Lagrange multipliers are selected in such a way that contact constraint conditions are accurately satisfied without causing singularity of the global system.

An experimental study on iterative solvers is given in Chapter 5. Combinations of preconditioned Krylov subspace methods with matrix reordering techniques are tested for a linear system resulting from the biphasic theory when not considering contact. The results, while of fundamental interest in biphasic problems, also are used to guide the choice of iterative solver for the contact analysis.

Chapter 6 illustrates the validity of the current methodology for biphasic contact analysis using various canonical problems including confined and unconfined compression tests, the Hertz contact problem, and biphasic indentation tests. Then, the gleno-humeral joint contact in human shoulders is solved as a clinically relevant example. Finally, Chapter 7 includes summary, concluding remarks and future directions

Chapter 2: Governing Equations for Biphasic Contact

2.1 Introduction

Two deformable bodies simulating hydrate soft tissues are considered in frictionless contact under the assumption of infinitesimal deformation. Based on the biphasic theory of Mow *et al*. [58], the governing equations and boundary conditions for contacting biphasic tissues have been developed by Hou *et al*. [36]. Hou and coworkers allow both material properties and tissue composition to be discontinuous at the contact surface, and applied the conservation laws to each body. It is assumed that, permeability and volume fraction of each phase within each tissue do not change with deformation.

Before introducing the governing equations, the kinematics of biphasic mixtures is briefly discussed to help in understanding the physics of such continua. A standard nomenclature is adopted as in the continuum mechanics, and the indicial notation is used. Indices (i, j, k and m) represent components in the spatial direction ranging 1, 2, … n_{sd} , in which repeated indices imply summation.

2.2 Kinematics of Biphasic Mixture

In the linear biphasic theory [58], articular cartilage is considered as a mixture of an intrinsically incompressible, linearly elastic solid phase, representing the collagen-proteoglycan matrix, and an intrinsically incompressible, inviscid fluid phase, representing the interstitial fluid. Each phase is assumed to be non-dissipative; the only

dissipation comes from the frictional drag of relative motion between the phases. For linear biphasic tissues, this dissipation gives rise to the time-dependent viscoelastic behavior of a biphasic tissue. Finally, both phases are assumed to be immiscible, chemically inert, isothermal, and to experience no heat supply.

A biphasic continuum can be considered as the superposition of the two phases (or constituents or continua). Let Ω^α and Γ^α denote the domain and boundary, respectively, of the α phase of the mixture in the current configuration. The superscript α denotes the solid and fluid phases by *s* and *f*, respectively. The domain and boundary of one phase is simultaneously shared with the other. In other words, a solid particle and a fluid particle can occupy the same infinitesimal volume at the same time. However, as a matter of convenience, the geometric boundary of the biphasic mixture is defined by the solid phase. This means that all the kinetic and kinematic boundary conditions will be applied on the solid material surface.

In order to express the motion of the mixture, a particle is identified by the position that it occupies at the reference time, instead of identifying every particle with the path line function as in particle mechanics. Let X_i^α denote the position of a particle (material position) of the α phase in the reference configuration at initial time t_o, and x_i^α denote its position (spatial position) in current configuration at the current time *t*. The motion of each continuum can be described by a deformation function (or mapping) χ^α, given as

$$x_i^\alpha(t) = x_i = \chi^\alpha\left(X_i^\alpha, t\right),\ \alpha = s, f, \tag{2.1}$$

The deformation function is assumed to be smooth and invertible, *i.e.*, $X_i^\alpha = (\chi^\alpha)^{-1}(x_i, t)$.

And the displacement for the particle is defined as

$$u_i^\alpha(t) = x_i(t) - X_i^\alpha(t),\ \alpha = s, f. \tag{2.2}$$

Figure 2.1 depicts general motion of a biphasic mixture. It is illustrated that material positions of X_i^s and X_i^f at time t_o move to their common spatial position x_i at time t. Velocity is defined as the material time derivative of the displacement with respect to the fixed phase material position.

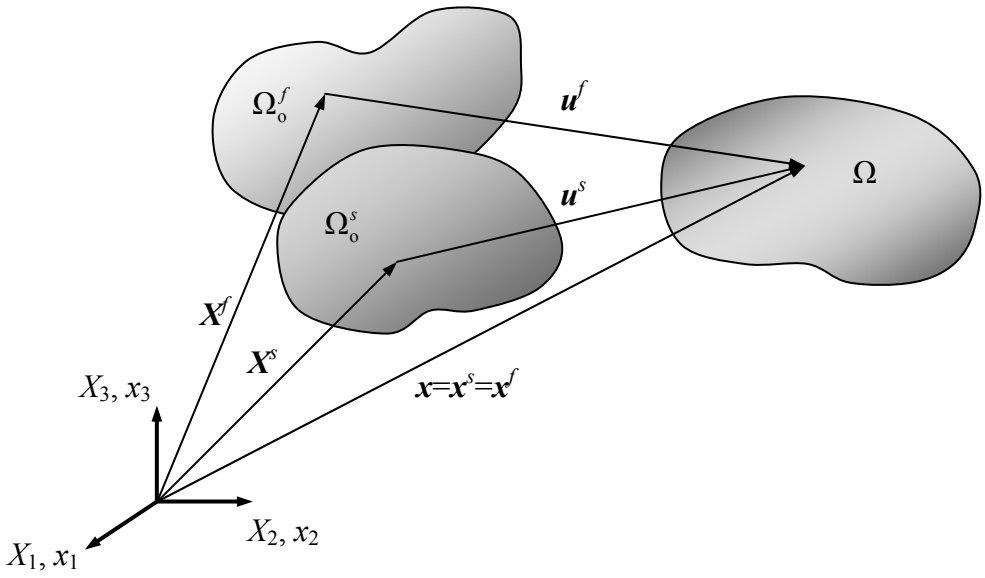

Figure 2.1 Definition of terms for the kinematics of a biphasic mixture.

For an immiscible mixture, two kinds of densities can be defined. The true density ρ_T^α is defined as the mass of a constituent per unit volume of that constituent, and the apparent density ρ^α as the mass of a constituent per unit volume of the mixture,

$$\rho_T^\alpha = \frac{dm^\alpha}{dV^\alpha},\ \alpha = s, f, \tag{2.3}$$

$$\rho^\alpha = \frac{dm^\alpha}{dV},\ \alpha = s, f. \tag{2.4}$$

Since each phase is assumed to be intrinsically incompressible, its true density remains constant during deformation. The volume faction of each phase is defined as

$$\phi^\alpha = \frac{dV^\alpha}{dV} = \frac{\rho^\alpha}{\rho_T^\alpha},\ \alpha = s, f. \tag{2.5}$$

When the mixture is saturated, the sum of both volume fractions is equal to 1, i.e., $\phi^s + \phi^f = 1$. As a consequence of Eq. (2.5), the true and apparent density are related by

$$\rho^\alpha = \phi^\alpha \rho_T^\alpha,\ \alpha = s, f. \tag{2.6}$$

2.3 Linear Biphasic Equations for Contact Problems

Consider a general contact system of two deformable biphasic bodies, as illustrated in Fig. 2.2. The reference configurations of body 'A' and body 'B' are denoted by Ω_o^A and Ω_o^B, respectively. It is assumed that the two bodies either do not touch at initial time t_o or touch such that no contact force is generated. As the configuration of each body changes along its deformation function of χ^A or χ^B at $t > 0$, contact can in theory occur between the two bodies or through self-contact within a single body, and contact pressure is developed. Note that self-contact does not occur in the physiological joints we consider and therefore it is not considered in this study. When the two bodies reside in ¡ $^{n_{sd}}$, i.e., $\Omega^A \subset$ ¡ $^{n_{sd}}$ and $\Omega^B \subset$ ¡ $^{n_{sd}}$, the geometric boundary is defined by the solid phase boundary, $\Gamma^A \subset$ ¡ $^{n_{sd}-1}$ and $\Gamma^B \subset$ ¡ $^{n_{sd}-1}$.

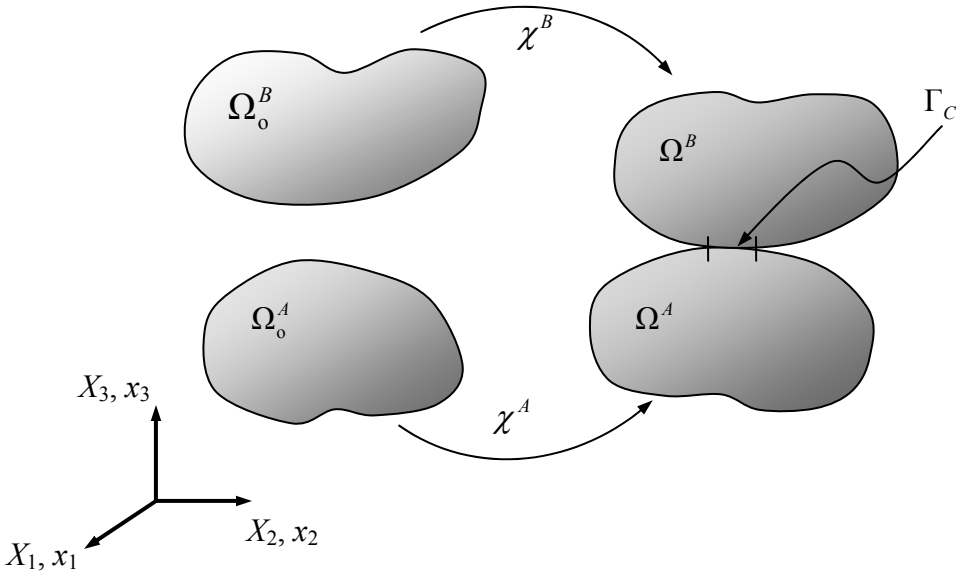

Figure 2.2 A contact system of two biphasic bodies at t_o and $t > 0$.

The motion of the system of bodies is subject to the principle of impenetrability of matter, which implies that at all times

$$\Omega^A \bigcap \Omega^B = \varnothing . \tag{2.7}$$

At any given time, two bodies are considered to be in contact along a subset $\Gamma_C \subset$ ¡ $^{n_{sd}-1}$ of their boundaries, if and only if

$$\Gamma_C \equiv \Gamma^A \bigcap \Gamma^B \neq \varnothing . \tag{2.8}$$

With the above definition, the boundary of each body can be uniquely decomposed into three parts,

$$\Gamma^\gamma = \Gamma_D^\gamma \bigcup \Gamma_N^\gamma \bigcup \Gamma_C , \ \gamma = A \ or \ B , \tag{2.9}$$

with Dirichlet and Neumann boundary conditions enforced on Γ_D^γ and Γ_N^γ, respectively. In the form of the biphasic equations used for this study, Dirichlet boundary condition

will be given as either prescribed solid displacement (or solid velocity), $\Gamma_{u^s}^{\gamma}$, or prescribed pressure, Γ_p^{γ} , and Neumann boundary condition will be in terms of prescribed traction, Γ_t^{γ} , or prescribed relative fluid flow, Γ_Q^{γ} . Therefore, in order for the initial-boundary value problem to be solvable, the boundary should satisfy

$$\Gamma^{\gamma} = \Gamma_{u^s}^{\gamma} \bigcup \Gamma_t^{\gamma} \bigcup \Gamma_C \text{ or } \Gamma^{\gamma} = \Gamma_p^{\gamma} \bigcup \Gamma_Q^{\gamma} \bigcup \Gamma_C \,.\ \gamma = A \text{ or } B \,. \tag{2.10}$$

2.3.1 Continuity of Solid Displacement

The balance equations and contact boundary conditions for a mixture contact system, $\Omega^A \bigcup \Omega^B$, will be developed in the following subsections. Besides those contact boundary conditions from balance equations, an additional kinematic condition should be satisfied over the contact area, so as to assure the continuity of solid displacement. In Figure 2.3, 'surface of discontinuity', Γ_C , is defined in a mixture contact system. Across this boundary, there exist discontinuities of material properties defining biphasic mixture.

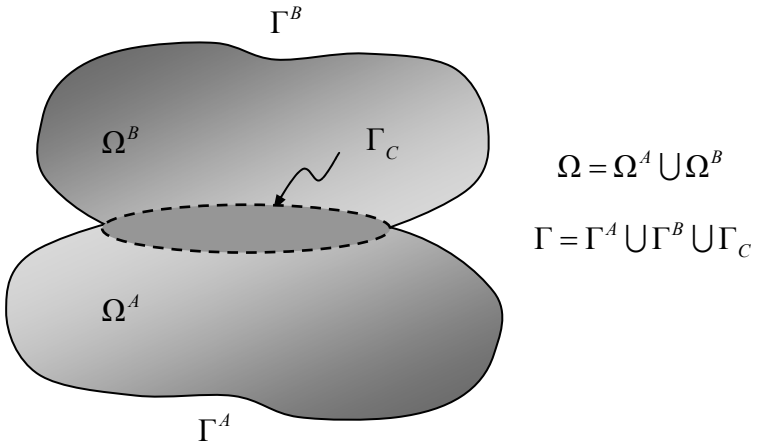

Figure 2.3 A mixture contact system containing a surface of discontinuity Γ_C

As stated earlier, the boundary of a mixture is defined by that of the solid phase. Therefore, when contact occurs, the current solid position of the contact boundary is shared by two bodies without any interpenetration. In other words, points of each body in persistent contact will have the same normal solid displacement and normal solid velocity. To update evolving contact, the first constraint is expressed in terms of the initial position X_i and the displacement u_i,

$$\left[\left(u_i^{sA} + X_i^{sA}\right) - \left(u_i^{sB} + X_i^{sB}\right)\right] n_i = 0, \quad \text{on } \Gamma_C, \tag{2.11}$$

where n_i is a unique unit outward normal on the surface. The time derivative of Eq. (2.11) gives the constraint of normal velocity as,

$$\left(v_i^{sA} - v_i^{sB}\right) n_i = 0, \quad \text{on } \Gamma_C. \tag{2.12}$$

Since sliding contact is allowed on Γ_C, there is no restriction on the tangential components of velocity. By noting that the unit outward normal vectors of n_i^A and n_i^B are opposite, i.e., $n_i^A = -n_i^B$, Eqs. (2.11) and (2.12) can be expressed in the convenient form.

$$\left(u_i^{sA} + X_i^{sA}\right) n_i^A + \left(u_i^{sB} + X_i^{sB}\right) n_i^B = 0, \quad \text{on } \Gamma_C, \tag{2.13}$$

$$v_i^{sA} n_i^A + v_i^{sB} n_i^B = 0, \quad \text{on } \Gamma_C. \tag{2.14}$$

Eq. (2.13) is considered as the first contact boundary condition. In the following subsections, three more contact constraints originally developed by Hou *et al*. [36] will be introduced from balance equations for mass, linear momentum and energy.

2.3.2 Balance of Mass

The integral statement of balance of mass for the biphasic mixture in a contact system is given as

$$\frac{d}{dt}\int_{\Omega}(\rho^{s}+\rho^{f})\,d\Omega=-\int_{\Gamma}\rho^{f}(v_{i}^{f}-v_{i}^{s})n_{i}\,d\Gamma\,. \tag{2.15}$$

The statement explains that the time rate of change of the mixture mass in the spatial volume is equivalent to the mass flux of fluid phase across the boundary. Since the mixture domain, $\Omega=\Omega^{A}\bigcup\Omega^{B}$, includes the surface of discontinuity, Γ_{C}, both fluid density and fluid velocity are expected to be discontinuous across the surface. Therefore, integrals of two portions of the domains separated by Γ_{C} can be separately considered. Next, applying the Reynolds' Transport Theorem yields the differential statement of mass balance,

$$\frac{\partial(\rho^{s}+\rho^{f})}{\partial t}+\left(\rho^{s}v_{i}^{s}+\rho^{f}v_{i}^{f}\right)_{,i}=0\,,\quad\text{on }\Omega^{A}\bigcup\Omega^{B}-\Gamma_{C}\,, \tag{2.16}$$

and the second contact boundary condition,

$$\rho^{fA}(v_{i}^{fA}-v_{i}^{sA})n_{i}^{A}+\rho^{fB}(v_{i}^{fB}-v_{i}^{sB})n_{i}^{B}=0\,,\quad\text{on }\Gamma_{C}\,. \tag{2.17}$$

It is often convenient to deal with volume fractions instead of densities of the constituents. This can be accomplished by applying the conditions of immiscibility ($\rho^{\alpha}=\phi^{\alpha}\rho_{T}^{\alpha}$) and intrinsic incompressibility, which yields

$$\frac{\partial(\phi^{\alpha})}{\partial t}+\left(\phi^{\alpha}v_{i}^{\alpha}\right)_{,i}=0\,,\quad\alpha=s,f,\text{ on }\Omega^{A}\bigcup\Omega^{B}-\Gamma_{C}\,, \tag{2.18}$$

In the linear biphasic theory, volume fractions are assumed to remain constant under deformation, and the above equation further reduces to,

$$\left(\phi^s v_i^s + \phi^f v_i^f\right)_{,i} = 0\,, \quad \text{on } \Omega^A \bigcup \Omega^B - \Gamma_C\,. \tag{2.19}$$

The boundary condition on a contact surface can be similarly reduced. Since the true density of the fluid phase does not experience a discontinuity across Γ_C, i.e., $\rho_T^{fA} = \rho_T^{fB}$, Eq. (2.17) can be written as

$$\phi^{fA}(v_i^{fA} - v_i^{sA})n_i^A + \phi^{fB}(v_i^{fB} - v_i^{sB})n_i^B = 0\,, \quad \text{on } \Gamma_C\,. \tag{2.20}$$

Next, assuming a saturated mixture ($\phi^{fA} + \phi^{sA} = 1$) and recognizing the continuity of normal solid velocity, Eq. (2.14), yields

$$(\phi^{fA} v_i^{fA} + \phi^{sA} v_i^{sA})n_i^A + (\phi^{fB} v_i^{fB} + \phi^{sB} v_i^{sB})n_i^B = 0\,, \quad \text{on } \Gamma_C\,. \tag{2.21}$$

This can be equivalently expressed in terms of displacement and reference position,

$$\left[\phi^{fA}(u_i^{fA} + X_i^{fA}) + \phi^{sA}(u_i^{sA} + X_i^{sA})\right]n_i^A + \left[\phi^{fB}(u_i^{fB} + X_i^{fB}) + \phi^{sB}(u_i^{sB} + X_i^{sB})\right]n_i^B = 0\,,$$

$$\text{on } \Gamma_C\,. \tag{2.22}$$

2.3.3 Balance of Linear Momentum

The integral statement of balance of linear momentum for a biphasic mixture in a contact system is given as

$$\frac{d}{dt}\int_\Omega (\rho^s v_i^s + \rho^f v_i^f)\, d\Omega = -\int_\Gamma \rho^f v_i^f (v_j^f - v_j^s) n_j\, d\Gamma$$

$$+\int_\Gamma (\sigma_{ij}^f + \sigma_{ij}^s) n_j\, d\Gamma + \int_\Omega (B_i^f + B_i^s) d\Omega + \int_\Omega (\boldsymbol{\Pi}_i^f + \boldsymbol{\Pi}_i^s) d\Omega\,. \tag{2.23}$$

where σ_{ij}^α is the Cauchy stress tensor, B_i^α is the external body force, and $\boldsymbol{\Pi}_i^\alpha$ is the momentum supply vector for the α phase. Since the momentum exchange is balanced

between the two phases ($\boldsymbol{\Pi}_i^f + \boldsymbol{\Pi}_i^s = 0$), the last term in Eq. (2.23) vanishes. Again, dividing the integrals into the two domains (Ω^A and Ω^B) and boundaries (Γ^A and Γ^B) and applying the Reynolds' Transport Theorem results in the differential statement of momentum balance for the mixture,

$$(\sigma_{ij}^f + \sigma_{ij}^s)_{,j} = -B_i^f - B_i^s + \rho^s \frac{\partial v_i^s}{\partial t} + \rho^s v_i^s v_{j,j}^s + \rho^f \frac{\partial v_i^f}{\partial t} + \rho^f v_i^f v_{j,j}^f ,$$

$$\text{on } \Omega^A \bigcup \Omega^B - \Gamma_C . \quad (2.24)$$

and the third contact boundary condition can be obtained as,

$$(\sigma_{ij}^{sA} + \sigma_{ij}^{fA}) n_j^A + (\sigma_{ij}^{sB} + \sigma_{ij}^{fB}) n_j^B = \rho^{fA} v_i^{fA} (v_j^{fA} - v_j^{sA}) n_j^A + \rho^{fB} v_i^{fB} (v_j^{fB} - v_j^{sB}) n_j^B ,$$

$$\text{on } \Gamma_C . \quad (2.25)$$

Under the assumption of no body force, no inertial terms and no convective effect, the right hand sides of Eqs. (2.24) and (2.25) vanish. And the momentum equations for the solid and fluid phases become,

$$\sigma_{ij,j}^{\alpha} + \boldsymbol{\Pi}_i^{\alpha} = 0 , \quad \alpha = s, f, \text{ on } \Omega^A \bigcup \Omega^B - \Gamma_C . \quad (2.26)$$

2.3.4 Balance of Energy

The integral statement of energy balance for the biphasic mixture in a contact system is given as

$$\frac{\partial}{\partial t} \int_\Omega (e^f + \frac{1}{2} \rho^f v_i^f v_i^f + e^s + \frac{1}{2} \rho^s v_i^s v_i^s) \, d\Omega$$

$$= -\int_\Gamma \rho^f (e^f + \frac{1}{2} v_i^f v_i^f)(v_j^f - v_j^s) n_j d\Gamma + \int_\Gamma (v_i^f \sigma_{ij}^f + v_i^s \sigma_{ij}^s) n_j d\Gamma + \int_\Omega (B_i^f v_i^f + B_i^s v_i^s) d\Omega$$

$$-\int_{\Gamma}(h_i^f - h_i^s)n_i d\Gamma + \int_{\Omega}(\Pi_i^f v_i^f + \Pi_i^s v_i^s)d\Omega + \int_{\Omega}(\tilde{e}^f + \tilde{e}^s)d\Omega\,, \tag{2.27}$$

where e^α is the internal energy density (or specific internal energy), h_i^α is the hear flux vector, and $\tilde{e}^\alpha$ is the energy supply to the α phase, which can be considered as energy interaction similar to the momentum supply vector Π_i^α as linear momentum interaction.

Through a procedure similar to that as in the previous sections, the differential statement of energy balance equation and the contact boundary condition can be obtained. After the application of the assumptions of isothermal deformation, no body forces, and no heat flux, the energy balance equation is reduced to

$$\left(\sigma_{ij}^f v_j^f\right)_{,i} - \rho^s\left(\frac{\partial e^s}{\partial t} + v_i^s e_{,i}^s\right) + \left(\sigma_{ij}^s v_j^s\right)_{,i} - \rho^f\left(\frac{\partial e^f}{\partial t} + v_i^f e_{,i}^f\right) = 0\,,\ \text{on}\ \Omega^A \bigcup \Omega^B - \Gamma_C\,. \tag{2.28}$$

And the fourth contact boundary condition is

$$\sigma_{ij}^{sA} v_j^{sA} n_i^A + \sigma_{ij}^{fA} v_j^{fA} n_i^A + \sigma_{ij}^{sB} v_j^{sB} n_i^B + \sigma_{ij}^{fB} v_j^{fB} n_i^B = 0\,,\quad \text{on}\ \Gamma_C\,. \tag{2.29}$$

2.4 Constitutive Equations for Biphasic Mixture

The kinematics and the balance equations in the previous sections are valid regardless of the structure and material properties of the biphasic materials. In order to characterize the response of the constituents, the stresses of each phase need to be expressed in terms of a certain measure of deformation, and the momentum exchange between phases needs to be related by certain biphasic properties.

There are several restrictions imposed on these constitutive equations. At first, the solution must be *objective*, also called the axiom of *material frame indifference* [83]. It states that the constitutive equations must be invariant under changes of reference

frame. Secondly, it must satisfy the second law of thermodynamics, also known as the *entropy inequality* [14]. Lastly, the governing equations and constitutive equations must be well-posed, and not allow any physically unrealistic behavior. Although there are many other aspects that need to be taken into consideration in the derivation of constitutive equations, they are not fully discussed in-depth here. A set of constitute equations satisfying the above criteria has been presented by Mow *et al*. [58] for the linear theory, and summarized below.

The constitutive relation for solid and fluid phases of a linear biphasic material are given as,

$$\sigma_{ij}^{s} = -\phi^{s} p\delta_{ij} + C_{ijkl}^{s}\varepsilon_{kl}\,, \tag{2.30}$$

$$\sigma_{ij}^{f} = -\phi^{f} p\delta_{ij}\,, \tag{2.31}$$

where δ_{ij} is the Kronecker delta and C_{ijkl}^{s} is the fourth-order elasticity tensor of the portion of the solid phase stress related to deformation. The hydrostatic pressure p, also called *pore pressure*, contributes to both stresses according to their volume fractions. The solid stress is composed of the elastic stress by *Hook's law* and the solid portion of pressure, and the fluid stress is proportional to the fluid portion of the pressure.

The momentum exchanges between the phases are defined as,

$$\boldsymbol{\Pi}_{i}^{s} = -\boldsymbol{\Pi}_{i}^{f} = p\phi_{,i}^{s} + K\left(v_{i}^{f} - v_{i}^{s}\right) \tag{2.32}$$

where K is the diffusive drag coefficient, related to the tissue permeability κ through [47],

$$K = \frac{\left(\phi^{f}\right)^{2}}{\kappa} \tag{2.33}$$

The first term of the right hand side of Eq. (2.32) corresponds to a buoyancy force arising from the gradient of solid volume fraction. The second term represents a momentum transfer from one phase to the other when a relative velocity exists between the two phases.

2.5 Frictionless Contact

Although the four contact boundary conditions of Eqs. (2.14), (2.20), (2.25) and (2.29) define a mathematically well-posed problem, it is not convenient to apply them directly to numerical analysis. For instance, the products of kinematic and kinetic quantities in Eq. (2.29) cause difficulties in constructing a finite element formulation. The product of solid stress and solid velocity leads nonlinearity in terms of solid displacement. Simple mathematical manipulations will transform the contact boundary conditions to an equivalent set of conditions that are easier to implement in numerical procedures. The conditions can be further reduced under the assumption of frictionless contact. Note that articular cartilage in diathrodial joints is well known for its extremely low friction coefficient [50], and thus the assumption of frictionless contact is reasonable.

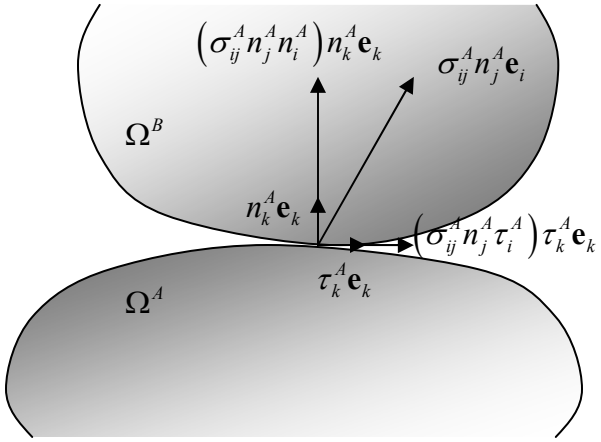

Figure 2.4 Decomposition of the traction vector at a point on body 'A' into the normal and tangential components

A traction vector $\sigma_{ij}^{A} n_j^{A} \mathbf{e}_i$ at a point on body 'A' can be decomposed into the normal and tangential components (Fig. 2.4):

$$\sigma_{ij}^{A} n_j^{A} \mathbf{e}_i = \left(\sigma_{ij}^{A} n_j^{A} n_i^{A}\right) n_k^{A} \mathbf{e}_k + \left(\sigma_{ij}^{A} n_j^{A} \tau_i^{A}\right) \tau_k^{A} \mathbf{e}_k \,. \tag{2.34}$$

Since the tangential components of traction are zero for frictionless contact, those components can be eliminated in the contact boundary conditions.

Beginning with Eq. (2.25), the right hand side is set to zero under the modeling assumptions previously noted. The total stress, defined as the sum of the fluid and solid stresses for each body, i.e., $\sigma_{ij}^{T\gamma} = \sigma_{ij}^{s\gamma} + \sigma_{ij}^{f\gamma}$, can be decomposed into the normal and tangential directions. Eliminating the tangential components and noting that $n_i^{A} = -n_i^{B}$, the third contact boundary condition becomes,

$$\left(\sigma_{ij}^{sA} + \sigma_{ij}^{fA}\right) n_i^{A} n_j^{A} - \left(\sigma_{ij}^{sB} + \sigma_{ij}^{fB}\right) n_i^{B} n_j^{B} = 0 \,. \tag{2.35}$$

Similar reduction is applied to Eq. (2.29). After decomposing tractions and velocities in the normal and tangential directions, and eliminating the tangential components of tractions, the fourth contact boundary condition reduces to,

$$\begin{aligned}&\left(\sigma_{ki}^{sA}n_i^A n_k^A\right)\left(v_m^{sA}n_m^A\right)+\left(\sigma_{ki}^{fA}n_i^A n_k^A\right)\left(v_m^{fA}n_m^A\right)\\&+\left(\sigma_{ki}^{sB}n_i^B n_k^B\right)\left(v_m^{sB}n_m^B\right)+\left(\sigma_{ki}^{fB}n_i^B n_k^B\right)\left(v_m^{fB}n_m^B\right)=0.\end{aligned} \tag{2.36}$$

Further algebraic manipulations on Eqs. (2.35) and (2.36) yield two kinetic conditions across the contact interface that express continuity of pressure and the normal component of the elastic part of the solid traction across the contact interface Γ_C (see Donzelli [18] for details):

$$p^A - p^B = 0\,, \tag{2.37}$$

$$\sigma_{ij}^{EA}n_i^A n_j^A - \sigma_{ij}^{EB}n_i^B n_j^B = 0\,. \tag{2.38}$$

In order to uniquely determine the correct contact area, another set of contact conditions, termed the *Kuhn-Tucker optimality conditions*, must be satisfied [51]:

$$\boldsymbol{g}\left(\boldsymbol{x}^A\right)\cdot\boldsymbol{n}\left(\boldsymbol{x}^A\right)\geq 0\,, \tag{2.39}$$

$$\boldsymbol{t}\left(\boldsymbol{x}^A\right)\cdot\boldsymbol{n}\left(\boldsymbol{x}^A\right)\leq 0\,, \tag{2.40}$$

$$\left\{\boldsymbol{t}\left(\boldsymbol{x}^A\right)\cdot\boldsymbol{n}\left(\boldsymbol{x}^A\right)\right\}\left\{\boldsymbol{g}\left(\boldsymbol{x}^A\right)\cdot\boldsymbol{n}\left(\boldsymbol{x}^A\right)\right\}=0\,, \tag{2.41}$$

where $\boldsymbol{g}\left(\boldsymbol{x}^A\right)$ is a closest point projection, also called the *gap function*, from a point $\boldsymbol{x}^A$ on Body 'A' to an opposing surface, $\boldsymbol{n}\left(\boldsymbol{x}^A\right)$ is a surface normal, and $\boldsymbol{t}\left(\boldsymbol{x}^A\right)$ is a total traction. Note that the vector notation is used to avoid confusion of summation convention in indicial notation for the repeated indices. Eq. (2.39) implies that interpenetration is not allowed between contacting bodies (*impenetrability*), and Eq.

(2.40) requires that all contact interactions should be compressive (*intensility*). The last condition, Eq. (2.41), rquires compressive traction on a contacting point and a traction-free condition at a non-contacting point (*complementarity*).

2.6 Summary of the Governing Equations and Boundary Conditions

The governing equations and contact boundary conditions are derived for the biphasic contact problem. Bearing these in mind, an initial-boundary value problem is summarized (the so-called *strong form* in finite element methodology). This will be used to develop the *weak form* for finite element methods. But before doing so, a modification on the continuity equation is necessary to derive the specific *v-p* finite element formulation used in this study. Derivation of the finite element contact formulations for biphasic analysis is presented in the next chapter.

The *v-p* formulation has solid displacement/velocity and pressure as primary variables, and thus fluid velocity v_i^f must be eliminated from the governing equations. This is accomplished by solving the fluid momentum equation, Eq. (2.26), for fluid velocity, substituting into the continuity equation, Eq. (2.19), and noting that the mixture is saturate ($\phi^s + \phi^f = 1$), giving the modified continuity equation,

$$\left(v_i^s - \kappa p_{,i}\right)_{,i} = 0\,. \tag{2.42}$$

Also, the boundary conditions on fluid velocity need to be correspondingly changed. Consequently, the strong form of the initial boundary value problem is as follows:

For the prescribed initial/boundary conditions, find the pressure, *p*, and solid displacement, $u_i^{s\gamma}$, fields: $\Omega^{\alpha\gamma} \times [0,T] \to ¡^{n_{sd}}$, $\alpha = s, f$ and $\gamma = A, B$ such that they satisfy:

1. Continuity and total linear momentum equations in $\Omega^A \bigcup \Omega^B - \Gamma_C$:

$$\left(v_i^s - \kappa p_{,i}\right)_{,i} = 0\,, \tag{2.43}$$

$$\sigma^s_{ij,j} + \sigma^f_{ij,j} = \left(C^s_{ijkl}\varepsilon_{kl} - p\delta_{ij} \right)_{,j} = 0 . \tag{2.44}$$

2. Initial and boundary conditions on either $\Gamma_D = \Gamma_u, \Gamma_p$ or $\Gamma^\gamma_N = \Gamma^\gamma_t, \Gamma^\gamma_Q$:

$$u^s_i \left(t = 0 \right) = \overline{u}^s_{io} \text{ and } u^s_i = \overline{u}^s_i \text{ on } \Gamma_u , \tag{2.45}$$

$$v^s_i \left(t = 0 \right) = \overline{v}^s_{io} \text{ and } v^s_i = \overline{v}^s_i \text{ on } \Gamma_v , \tag{2.46}$$

$$p = \overline{p} \text{ on } \Gamma_p , \tag{2.47}$$

$$\sigma^T_{ij} n_j = t^T_i = \overline{t}^T_i \text{ on } \Gamma_t , \tag{2.48}$$

$$\phi^f \left(v^f_i - v^s_i \right) n_i = -\kappa p_{,i} n_i = \overline{Q} \text{ on } \Gamma_Q . \tag{2.49}$$

where total stress is defined as the sum of the fluid and solid stresses, $\sigma^T_{ij} = \sigma^s_{ij} + \sigma^f_{ij}$, and the relative fluid flow is defined as $\phi^f \left(v^f_i - v^s_i \right) n_i$ or $-\kappa p_{,i} n_i$.

3. Strain-displacement relation:

$$\varepsilon_{ij} = u^s_{(i,j)} = \frac{1}{2} \left(u^s_{i,j} + u^s_{j,i} \right) . \tag{2.50}$$

4. Constitutive relations:

$$\sigma^s_{ij} = -\phi^s p\delta_{ij} + C^s_{ijkl}\varepsilon_{kl} , \tag{2.51}$$

$$\sigma^f_{ij} = -\phi^f p\delta_{ij} , \tag{2.52}$$

$$\Pi^s_i = -\Pi^f_i = p\phi^s_{,i} + K \left(v^f_i - v^s_i \right) . \tag{2.53}$$

5. Contact boundary conditions on Γ_C:

From the balance equations,

$$\left(u^{sA}_i + X^{sA}_i \right) n^A_i + \left(u^{sB}_i + X^{sB}_i \right) n^B_i = 0 \quad \text{or}$$

$$v_i^{sA} n_i^A + v_i^{sB} n_i^B = 0 \tag{2.54}$$

$$\phi^{fA}(v_i^{fA} - v_i^{sA}) n_i^A + \phi^{fB}(v_i^{fB} - v_i^{sB}) n_i^B = 0 \quad \text{or}$$

$$\kappa^A p_{,i}^A n_i^A + \kappa^B p_{,i}^B n_i^B = 0\,, \tag{2.55}$$

$$p^A - p^B = 0\,, \tag{2.56}$$

$$\sigma_{ij}^{EA} n_i^A n_j^A - \sigma_{ij}^{EB} n_i^B n_j^B = 0\,, \tag{2.57}$$

Kuhn-Tucker optimality conditions,

$$\boldsymbol{g}\left(\boldsymbol{x}^A\right) \cdot \boldsymbol{n}\left(\boldsymbol{x}^A\right) \geq 0\,, \tag{2.58}$$

$$\boldsymbol{t}\left(\boldsymbol{x}^A\right) \cdot \boldsymbol{n}\left(\boldsymbol{x}^A\right) \leq 0\,, \tag{2.59}$$

$$\left\{\boldsymbol{t}\left(\boldsymbol{x}^A\right) \cdot \boldsymbol{n}\left(\boldsymbol{x}^A\right)\right\}\left\{\boldsymbol{g}\left(\boldsymbol{x}^A\right) \cdot \boldsymbol{n}\left(\boldsymbol{x}^A\right)\right\} = 0\,. \tag{2.60}$$

Chapter 3: Finite Element Contact Formulation and Numerical Implementation

3.1 Introduction

In the present chapter, two finite element biphasic contact formulations will be developed based on the governing equations and boundary conditions presented in the previous chapter, and the implementation and contact algorithm for 3-D biphasic contact will be discussed. The velocity-pressure (*v-p*) finite element formulation is adopted in this study based on its robustness with tetrahedral elements in 3-D biphasic analysis. A Lagrange multiplier technique is used to introduce the contact conditions. It should be noted that while this approach follows in the broadest of definitions the overall technique used by Donzelli [18, 19] for 2-D biphasic contact, it differs in many important ways; the underlying finite element formulation, the contact conditions treated by Lagrange multiplier, and algorithms for contact inspection and integral calculation. As a result, issues related to stability and convergence will necessarily differ.

3.2 Weighted Residual Statement

The weighted residual approach is used to derive the current *v-p* finite element formulation. Two alternate formulations are proposed, differing in which of the contact constraints are introduced into the weighted residual statement directly and which are introduced using Lagrange multipliers. Note that if the resulting finite element equations

are symmetric, an equivalent energy functional exists that produces the equivalent variational equation [93]. With proper choice of the Lagrange multipliers, symmetric systems are obtained for both formulations.

Among the four equality contact constraints, Eqs. (2.54)-(2.57), Lagrange multipliers are used in this first formulation to introduce the constraints on the derived quantities, relative fluid flow and normal elastic traction, Eqs. (2.55) and (2.57). Note that the primary variables in the underlying *v-p* formulation are solid displacement and pressure. The scalar Lagrange multiplier λ^f is used to introduce the relative fluid flow continuity across Γ_C, by writing

$$\lambda^f \equiv -\kappa^A p^A_{,i} n^A_i \text{ on } \Gamma_C, \tag{3.1}$$

$$\lambda^f \equiv \kappa^B p^B_{,i} n^B_i \text{ on } \Gamma_C. \tag{3.2}$$

Similarly, the scalar Lagrange multiplier λ^s is defined for normal elastic stress continuity on Γ_C, as

$$\lambda^s \equiv \sigma^{EA}_{ij} n^A_i n^A_j \text{ on } \Gamma_C, \tag{3.3}$$

$$\lambda^s \equiv \sigma^{EB}_{ij} n^B_i n^B_j \text{ on } \Gamma_C. \tag{3.4}$$

Mathematically, the above equations are equivalent to the original contact continuity conditions. In the finite element formulation, the Lagrange multipliers become additional variables that are defined on the contact surface. At this stage, it is not clearly noticeable, but worthwhile to mention that this choice of λ^s will results in the non-symmetry of global system. To preserve the global symmetry, hydrostatic pressure is added in the definition of λ^s,

$$\lambda^s \equiv \sigma_{ij}^{E\gamma} n_i^\gamma n_j^\gamma - p^\gamma \,. \quad \gamma = A \text{ or } B \tag{3.5}$$

It is a mathematically legitimate substitute as the pressure continuity condition is satisfied within the formulation. This choice yields a symmetric global system of equations, as will be seen later.

Alternatively, Lagrange multipliers can be defined for the constraints on the kinetic variables, Eqs. (2.56) and (2.57). This choice also produces a symmetric global system. A finite element formulation based on this choice will be developed in a later section.

3.2.1 Trial and Weighting Function Spaces

To develop the weak form using the weighted residual method, two classes of functions need to be characterized [38, 42]; the first is the trial, or candidate, function, and the second is the weighting function. The trial function spaces for the solid velocity, pressure and Lagrange multipliers, respectively, are defined as

$$\delta_{v^s} = \left\{ w \middle| \; w \in H^1, \; w = \overline{w} \text{ on } \Gamma_{v^s} \right\}, \tag{3.6}$$

$$\delta_p = \left\{ w \middle| \; w \in H^1, \; w = \overline{w} \text{ on } \Gamma_p \right\}, \tag{3.7}$$

$$\delta_C = \left\{ w \middle| \; w \in H^0, \; w = 0 \text{ on } \Omega \setminus \Gamma_C \right\}. \tag{3.8}$$

The Sobolev space of degree *k*, denoted by H^k, is defined as

$$H^k(\Omega) = \left\{ w \middle| \; w \in L_2; \; w_{,x} \in L_2; \; \ldots; \; w_{,\underbrace{x \ldots x}_{k \text{ times}}} \in L_2 \right\}. \tag{3.9}$$

where $L_2(\Omega)$ is the space of square-integrable functions:

$$L_2(\Omega) = \left\{ w \middle| \int_\Omega w(x)^2 < \infty,\ x \in \Omega \right\}. \tag{3.10}$$

Similarly, three weighting function spaces are defined as,

$$\upsilon_{v^s} = \left\{ w \middle| \ w \in H^1,\ w = 0 \ on \ \Gamma_{v^s} \right\}, \tag{3.11}$$

$$\upsilon_p = \left\{ w \middle| \ w \in H^1,\ w = 0 \ on \ \Gamma_p \right\}, \tag{3.12}$$

$$\upsilon_C = \left\{ w \middle| \ w \in H^0,\ w = 0 \ on \ \Omega \setminus \Gamma_C \right\}. \tag{3.13}$$

The trial functions satisfy the Dirichlet boundary conditions, and the weighting functions satisfy the homogeneous counterparts.

3.2.2 Weak Form

In the *v-p* contact formulation, the total linear momentum equation, continuity equation, natural boundary conditions (on Γ_t or Γ_Q), and Lagrange multiplier – based contact continuity constraints are introduced into the weighted residual for each body, and the remaining two contact constraints on primary variables are introduced directly into the weighted residual on the contact boundary. Therefore, the complete weighted residual statement is composed of terms from body 'A', body 'B' and the contact surface Γ_C, and will be in the form,

$$G^A + G^B + G^C = 0 \tag{3.14}$$

The contributions from body 'A' is

$$G^A = \int_{\Omega^A} w_i^A \left(\sigma_{ij,j}^{EA} - p_{,i}^A \right) \mathrm{d}\Omega + \int_{\Omega^A} q^A \left(v_i^{sA} - \kappa^A p_{,i}^A \right)_{,i} \mathrm{d}\Omega$$

$$+\int_{\Gamma_t^A} s_i^A\left(\bar{t}_i^A-\left(\sigma_{ij}^{EA}-p^A\delta_{ij}\right)n_j^A\right)\mathrm{d}\Gamma+\int_{\Gamma_Q^A} o^A\left(\bar{Q}^A+\kappa^A p_{,i}^A n_i^A\right)\mathrm{d}\Gamma \tag{3.15}$$

$$\int_{\Gamma_C^A} r^{fA}\left(\lambda^f+\kappa^A p_{,i}^A n_i^A\right)\mathrm{d}\Gamma+\int_{\Gamma_C^A} r^{sA}\left(\lambda^s-\sigma_{ij}^{EA}n_i^A n_j^A+p^A\right)\mathrm{d}\Gamma\,.$$

The weighting functions are restricted such as $w_i^A\in\upsilon_{v^s}$, $q^A\in\upsilon_p$, $s_i^A\in\upsilon_{v^s}$, $o^A\in\upsilon_p$, $r^{fA}\in\upsilon_C$ and $r^{sA}\in\upsilon_C$. Similarly, the trial solutions are restricted such as $v_i^{sA}\in\delta_{v^s}$ $u_i^{sA}\in\delta_{v^s}$, $p\in\delta_p$ and $\lambda^\alpha\in\delta_C$ for $\alpha=s,f$. The elastic stress σ_{ij}^{EA} is expressed in terms of solid displacement, u_i^{sA}, which is related to solid velocity v_i^{sA}, and is therefore not an additional unknown. Note that δ_{ij} is the Kronecker delta and should not be confused with the trial function spaces. Note also that Γ_C^A is simply used as an indication of the contribution from body 'A', and has the same physical meaning as Γ_C.

To develop the weak form from the weighted residual statement, terms including high order derivatives need to be integrated by parts. After applying the Divergence theorem, the first, second and fourth terms in Eq. (3.15) become, respectively,

$$\int_{\Omega^A} w_i^A\sigma_{ij,j}^{EA}\,\mathrm{d}\Omega=\int_{\Gamma^A} w_i^A\sigma_{ij}^{EA}n_j^A\mathrm{d}\Gamma-\int_{\Omega^A} w_{(i,j)}^A\sigma_{ij}^{EA}\mathrm{d}\Omega\,, \tag{3.16}$$

$$\int_{\Omega^A} w_i^A p_{,i}^A\,\mathrm{d}\Omega=\int_{\Gamma^A} w_i^A p^A n_i^A\mathrm{d}\Gamma-\int_{\Omega^A} w_{i,i}^A p^A\mathrm{d}\Omega\,, \tag{3.17}$$

$$\int_{\Omega^A} q^A\kappa^A p_{,ii}^A\mathrm{d}\Omega=\int_{\Gamma^A} q^A\kappa^A p_{,i}^A n_i^A\mathrm{d}\Gamma-\int_{\Omega^A} q_{,i}^A\kappa^A p_{,i}^A\mathrm{d}\Omega\,, \tag{3.18}$$

where the parenthesis around indices indicates the symmetric part of the second order tensor. These are substituted into Eq. (3.15). Also, since the weighting functions are arbitrary, they are chosen to satisfy $s_i^A=w_i^A$, $o^A=q^A$, $r^{fA}=q^A$ and $r^{sA}=w_k^A n_k^A$, which

results in the cancellation of several terms. Note that the boundary is composed of either $\Gamma^A = \Gamma_u^A \bigcup \Gamma_t^A \bigcup \Gamma_C^A$ or $\Gamma^A = \Gamma_p^A \bigcup \Gamma_Q^A \bigcup \Gamma_C^A$. Since the weighting functions each satisfy the homogenous form of one of the essential boundary conditions, the boundary integrals on essential boundary vanish.

Following these choices and manipulations, the contributions from body 'A' become,

$$G^A = -\int_{\Omega^A} w^A_{(i,j)} \sigma_{ij}^{EA} \mathrm{d}\Omega + \int_{\Omega^A} w^A_{i,i} p^A \mathrm{d}\Omega + \int_{\Omega^A} q^A v^{sA}_{i,i} \mathrm{d}\Omega + \int_{\Omega^A} q^A_{,i} \kappa^A p^A_{,i} \mathrm{d}\Omega$$

$$+ \int_{\Gamma_t^A} w_i^A \overline{t}_i^A \mathrm{d}\Gamma + \int_{\Gamma_Q^A} q^A \overline{Q}^A \mathrm{d}\Gamma + \int_{\Gamma_C^A} q^A \lambda^f \mathrm{d}\Gamma + \int_{\Gamma_C^A} w_k^A n_k^A \lambda^s \mathrm{d}\Gamma \tag{3.19}$$

When *n*th-order derivative occurs in any term of integrands in Eqs. (3.15) and (3.19), the function has to be such that its *n*-1 derivatives are continuous (C_{n-1} continuity). Hence, C_0 continuity is required for the trial functions v_i^{sA} and p and the weighting functions, w_i^A and q^A. Contributions from body 'B', G^B, can be derived in the same manner. The only difference is the negative sign on the integral involving λ^f (see Eqs. (3.1) and (3.2)).

Contributions from the contact surface, G^C, consist of the weighted contact constraints related to continuity of current solid position and pressure, Eqs. (2.54) and (2.56), which is given as

$$G^C = \int_{\Gamma_C} s^s \left\{ \left(u_i^{sA} + X_i^{sA} \right) n_i^A + \left(u_i^{sB} + X_i^{sB} \right) n_i^B \right\} \mathrm{d}\Gamma + \int_{\Gamma_C} s^f \left(p^A - p^B \right) \mathrm{d}\Gamma, \tag{3.20}$$

where the scalar weighting functions are chosen such that $s^s, s^f \in \upsilon_C$.

The complete weak form of the weighted residual statements can be formed as the sum of the contributions from body 'A', body 'B' and the contact boundary. After multiplying by '-1', the weak form is

$$\int_{\Omega^A} w^A_{(i,j)}\sigma^{EA}_{ij}\mathrm{d}\Omega - \int_{\Omega^A} w^A_{i,i}p^A\mathrm{d}\Omega - \int_{\Omega^A} q^A v^{sA}_{i,i}\mathrm{d}\Omega - \int_{\Omega^A} q^A_{,i}\kappa^A p^A_{,i}\mathrm{d}\Omega$$

$$-\int_{\Gamma^A_t} w^A_i \overline{t}^A_i\mathrm{d}\Gamma - \int_{\Gamma^A_Q} q^A\overline{Q}^A\mathrm{d}\Gamma - \int_{\Gamma^A_C} q^A\lambda^f\mathrm{d}\Gamma - \int_{\Gamma^A_C} w^A_k n^A_k\lambda^s\mathrm{d}\Gamma$$

$$\int_{\Omega^B} w^B_{(i,j)}\sigma^{EB}_{ij}\mathrm{d}\Omega - \int_{\Omega^B} w^B_{i,i}p^B\mathrm{d}\Omega - \int_{\Omega^B} q^B v^{sB}_{i,i}\mathrm{d}\Omega - \int_{\Omega^B} q^B_{,i}\kappa^B p^B_{,i}\mathrm{d}\Omega$$

$$-\int_{\Gamma^B_t} w^B_i \overline{t}^B_i\mathrm{d}\Gamma - \int_{\Gamma^B_Q} q^B\overline{Q}^B\mathrm{d}\Gamma + \int_{\Gamma^B_C} q^B\lambda^f\mathrm{d}\Gamma - \int_{\Gamma^B_C} w^B_k n^B_k\lambda^s\mathrm{d}\Gamma$$

$$-\int_{\Gamma_C} s^s\left\{\left(u^{sA}_i + X^{sA}_i\right)n^A_i + \left(u^{sB}_i + X^{sB}_i\right)n^B_i\right\}\mathrm{d}\Gamma - \int_{\Gamma_C} s^f\left(p^A - p^B\right)\mathrm{d}\Gamma = 0\,. \qquad (3.21)$$

3.2.3 Finite Element Matrix Equation

As a matter of convenience, the indicial notation is now discarded and the vector-matrix notation is used. The problem domain is divided into the biphasic finite elements and solid displacement, solid velocity (time derivative of displacement, not an independent variable) and pressure are interpolated in terms of nodal values, with subscript 'e' indicating the element number. Also, the Lagrange multipliers are interpolated within the contact element.

$$\boldsymbol{v}^{s\gamma} = \mathbf{N}^\gamma \boldsymbol{v}^{s\gamma}_e\,, \quad \gamma = A, B\,, \qquad (3.22)$$

$$\boldsymbol{u}^{s\gamma} = \mathbf{N}^\gamma \boldsymbol{u}^{s\gamma}_e\,, \quad \gamma = A, B\,, \qquad (3.23)$$

$$p^\gamma = \mathbf{N}^\gamma_p \boldsymbol{p}^\gamma_e\,, \quad \gamma = A, B\,, \qquad (3.24)$$

$$\lambda^{\alpha} = \mathbf{M}^{\alpha} \boldsymbol{\lambda}_e^{\alpha}, \quad \alpha = s, f, \tag{3.25}$$

where the interpolation functions are chosen such that $\mathbf{N}^{\gamma} \in \delta_{v^s}^h \subset \delta_{v^s}$, $\mathbf{N}_p^{\gamma} \in \delta_p^h \subset \delta_p$ and $\mathbf{M}^{\alpha} \in \delta_C^h \subset \delta_C$, and where the superscript '*h*' refers to the finite dimensional subspace. In the Galerkin weighted residual method (*Bubnov-Galerkin*), the same interpolation functions are used for the corresponding weighting functions. This method often leads to symmetric matrices, as is the current formulation. For that reason, the weight functions for the solid velocity (or solid displacement), pressure and Lagrange multipliers are given as

$$\boldsymbol{w}^{s\gamma} = \mathbf{N}^{\gamma} \boldsymbol{w}_e^{s\gamma}, \quad \gamma = A, B, \tag{3.26}$$

$$q^{\gamma} = \mathbf{N}_p^{\gamma} \boldsymbol{q}_e^{\gamma}, \quad \gamma = A, B, \tag{3.27}$$

$$s^{\alpha} = \mathbf{M}^{\alpha} \boldsymbol{s}_e^{\alpha}, \quad \alpha = s, f, \tag{3.28}$$

where the interpolation functions are chosen such that $\mathbf{N}^{\gamma} \in \upsilon_{v^s}^h \subset \upsilon_{v^s}$, $\mathbf{N}_p^{\gamma} \in \upsilon_p^h \subset \upsilon_p$ and $\mathbf{M} \in \upsilon_C^h \subset \upsilon_C$.

The elastic stress is expressed in terms of solid displacement through the constitutive relations, Eq. (2.51). The reduced index notation for stress and strain is used, with independent components of the symmetric tensor arranged in a vector. The fourth-order elasticity tensor C_{ijkl}^s is accordingly represented in matrix form as a square, symmetric matrix $\boldsymbol{C}$. Also, the divergence, gradient, and symmetric gradient operations are defined in matrix form, respectively, as

$$\mathrm{L}_{div}=\begin{bmatrix}\dfrac{\partial}{\partial x} & \dfrac{\partial}{\partial y} & \dfrac{\partial}{\partial z}\end{bmatrix},\ \mathrm{L}_{\nabla}^{sca}=\begin{bmatrix}\dfrac{\partial}{\partial x}\\ \dfrac{\partial}{\partial y}\\ \dfrac{\partial}{\partial z}\end{bmatrix},\mathrm{L}_{\nabla}^{sym}=\begin{bmatrix}\dfrac{\partial}{\partial x} & 0 & 0\\ 0 & \dfrac{\partial}{\partial y} & 0\\ 0 & 0 & \dfrac{\partial}{\partial z}\\ \dfrac{\partial}{\partial y} & \dfrac{\partial}{\partial x} & 0\\ \dfrac{\partial}{\partial z} & 0 & \dfrac{\partial}{\partial x}\\ 0 & \dfrac{\partial}{\partial z} & \dfrac{\partial}{\partial y}\end{bmatrix} \tag{3.29}$$

After substituting the interpolations into Eq. (3.21) for n_{el} elements in the domain $\Omega^A \bigcup \Omega^B$, the matrix form of the weighted residual is

$$\sum_{e=1}^{n_{el}}\Bigg\{ \boldsymbol{w}_e^{A^T}\int_{\Omega_e^A}\left(L_{\nabla}^{sym}\mathbf{N}^A\right)^T\boldsymbol{C}^A\left(L_{\nabla}^{sym}\mathbf{N}^A\right)\mathrm{d}\Omega\,\boldsymbol{u}_e^{sA}-\boldsymbol{w}_e^{A^T}\int_{\Omega_e^A}\left(L_{div}\mathbf{N}^A\right)^T\mathbf{N}_p^A\mathrm{d}\Omega\,\boldsymbol{p}_e^A$$

$$-\boldsymbol{q}_e^{A^T}\int_{\Omega_e^A}\mathbf{N}_p^{A^T}\left(L_{div}\mathbf{N}^A\right)\mathrm{d}\Omega\,\boldsymbol{v}_e^{sA}-\boldsymbol{q}_e^{A^T}\int_{\Omega_e^A}\left(L_{\nabla}^{sca}\mathbf{N}_p^A\right)^T\boldsymbol{\kappa}^A\left(L_{\nabla}^{sca}\mathbf{N}_p^A\right)\mathrm{d}\Omega\,\boldsymbol{p}_e^A$$

$$-\boldsymbol{w}_e^{A^T}\int_{\Gamma_{t_e}^A}\mathbf{N}^{A^T}\overline{\boldsymbol{t}}^A\mathrm{d}\Gamma-\boldsymbol{q}_e^{A^T}\int_{\Gamma_{Q_e}^A}\mathbf{N}_p^{A^T}\overline{\boldsymbol{Q}}^A\mathrm{d}\Gamma-\boldsymbol{q}_e^{A^T}\int_{\Gamma_{C_e}}\mathbf{N}_p^{A^T}\mathbf{M}^f\mathrm{d}\Gamma\boldsymbol{\lambda}_e^f-\boldsymbol{w}_e^{A^T}\int_{\Gamma_{C_e}}\mathbf{N}^{A^T}\boldsymbol{n}^A\mathbf{M}^s\mathrm{d}\Gamma\boldsymbol{\lambda}_e^s$$

$$+\boldsymbol{w}_e^{B^T}\int_{\Omega_e^B}\left(L_{\nabla}^{sym}\mathbf{N}^B\right)^T\boldsymbol{C}^B\left(L_{\nabla}^{sym}\mathbf{N}^B\right)\mathrm{d}\Omega\,\boldsymbol{u}_e^{sB}-\boldsymbol{w}_e^{B^T}\int_{\Omega_e^B}\left(L_{div}\mathbf{N}^B\right)^T\mathbf{N}_p^B\,\mathrm{d}\Omega\,\boldsymbol{p}_e^B$$

$$-\boldsymbol{q}_e^{B^T}\int_{\Omega_e^B}\mathbf{N}_p^{B^T}\left(L_{div}\mathbf{N}^B\right)\mathrm{d}\Omega\,\boldsymbol{v}_e^{sB}-\boldsymbol{q}_e^{B^T}\int_{\Omega_e^B}\left(L_{\nabla}^{sca}\mathbf{N}_p^B\right)^T\boldsymbol{\kappa}^A\left(L_{\nabla}^{sca}\mathbf{N}_p^B\right)\mathrm{d}\Omega\,\boldsymbol{p}_e^B$$

$$-\boldsymbol{w}_e^{B^T}\int_{\Gamma_{t_e}^B}\mathbf{N}^{B^T}\overline{\boldsymbol{t}}^B\mathrm{d}\Gamma-\boldsymbol{q}_e^{B^T}\int_{\Gamma_{Q_e}^B}\mathbf{N}_p^{B^T}\overline{\boldsymbol{Q}}^B\mathrm{d}\Gamma+\boldsymbol{q}_e^{B^T}\int_{\Gamma_{C_e}}\mathbf{N}_p^{B^T}\mathbf{M}^f\mathrm{d}\Gamma\boldsymbol{\lambda}_e^f-\boldsymbol{w}_e^{B^T}\int_{\Gamma_{C_e}}\mathbf{N}^{B^T}\boldsymbol{n}^B\mathbf{M}^s\mathrm{d}\Gamma\boldsymbol{\lambda}_e^s$$

$$-\boldsymbol{s}_e^{s^T}\int_{\Gamma_{C_e}}\mathbf{M}^{s^T}\boldsymbol{n}^{A^T}\mathbf{N}^A\mathrm{d}\Gamma\left(\boldsymbol{u}_e^{sA}+\boldsymbol{X}_e^{sA}\right)-\boldsymbol{s}_e^{s^T}\int_{\Gamma_{C_e}}\mathbf{M}^{s^T}\boldsymbol{n}^{B^T}\mathbf{N}^B\mathrm{d}\Gamma\left(\boldsymbol{u}_e^{sB}+\boldsymbol{X}_e^{sB}\right)$$

$$-\boldsymbol{s}_e^{f^T}\int_{\Gamma_{C_e}}\mathbf{M}^{f^T}\mathbf{N}_p^A\mathrm{d}\Gamma\,\boldsymbol{p}_e^A+\boldsymbol{s}_e^{f^T}\int_{\Gamma_{C_e}}\mathbf{M}^{f^T}\mathbf{N}_p^B\mathrm{d}\Gamma\,\boldsymbol{p}_e^B\Bigg\}=0\,. \tag{3.30}$$

Note that the nodal degrees of freedom have already been brought outside of the integrals, since they are independent of the coordinates. The integrals in Eq. (3.30) give rise to the following element matrices:

$$\boldsymbol{a}_e^\gamma=\int_{\Omega_e^\gamma}\left(L_{div}\mathbf{N}^\gamma\right)^T\mathbf{N}_p^\gamma\mathrm{d}\Omega\,,\quad\gamma=A,B\,, \tag{3.31}$$

$$\boldsymbol{b}_e^\gamma=\int_{\Omega_e^\gamma}\left(L_\nabla^{sca}\mathbf{N}_p^\gamma\right)^T\boldsymbol{\kappa}^\gamma\left(L_\nabla^{sca}\mathbf{N}_p^\gamma\right)\mathrm{d}\Omega\,,\quad\gamma=A,B\,, \tag{3.32}$$

$$\boldsymbol{k}_e^\gamma=\int_{\Omega_e^\gamma}\left(L_\nabla^{sym}\mathbf{N}^\gamma\right)^T\boldsymbol{C}^\gamma\left(L_\nabla^{sym}\mathbf{N}^\gamma\right)\mathrm{d}\Omega\,,\quad\gamma=A,B\,, \tag{3.33}$$

$$\boldsymbol{q}_e^{s\gamma}=\int_{\Gamma_{C_e}}\mathbf{N}^{\gamma^T}\boldsymbol{n}^\gamma\mathbf{M}^s\mathrm{d}\Gamma\,,\quad\gamma=A,B\,, \tag{3.34}$$

$$\boldsymbol{q}_e^{f\gamma}=\int_{\Gamma_{C_e}}\mathbf{N}_p^{\gamma^T}\mathbf{M}^f\mathrm{d}\Gamma\,,\quad\gamma=A,B\,, \tag{3.35}$$

$$\boldsymbol{f}_{t_e}^\gamma=\int_{\Gamma_{t_e}^\gamma}\mathbf{N}^{\gamma^T}\overline{\boldsymbol{t}}^\gamma\mathrm{d}\Gamma\,,\quad\gamma=A,B\,, \tag{3.36}$$

$$\boldsymbol{f}_{Q_e}^\gamma=\int_{\Gamma_{Q_e}^\gamma}\mathbf{N}_p^{\gamma^T}\overline{\boldsymbol{Q}}^\gamma\mathrm{d}\Gamma\,,\quad\gamma=A,B\,. \tag{3.37}$$

With these definitions, Eq. (3.30) becomes,

$$
\sum_{e=1}^{n_{el}}
\begin{bmatrix}
\boldsymbol{w}_e^A \\ \boldsymbol{q}_e^A \\ \hdashline \boldsymbol{w}_e^B \\ \boldsymbol{q}_e^B \\ \hdashline \boldsymbol{s}_e^s \\ \boldsymbol{s}_e^f
\end{bmatrix}^T
\left[\begin{array}{cc:cc:cc}
\boldsymbol{0} & -\boldsymbol{a}_e^A & \boldsymbol{0} & \boldsymbol{0} & -\boldsymbol{q}_e^{sA} & \boldsymbol{0} \\
-\boldsymbol{a}_e^{AT} & -\boldsymbol{b}_e^A & \boldsymbol{0} & \boldsymbol{0} & \boldsymbol{0} & -\boldsymbol{q}_e^{fA} \\ \hdashline
\boldsymbol{0} & \boldsymbol{0} & \boldsymbol{0} & -\boldsymbol{a}_e^B & -\boldsymbol{q}_e^{sB} & \boldsymbol{0} \\
\boldsymbol{0} & \boldsymbol{0} & -\boldsymbol{a}_e^{BT} & -\boldsymbol{b}_e^B & \boldsymbol{0} & \boldsymbol{q}_e^{fB} \\ \hdashline
\boldsymbol{0} & \boldsymbol{0} & \boldsymbol{0} & \boldsymbol{0} & \boldsymbol{0} & \boldsymbol{0} \\
\boldsymbol{0} & -\boldsymbol{q}_e^{fAT} & \boldsymbol{0} & \boldsymbol{q}_e^{fBT} & \boldsymbol{0} & \boldsymbol{0}
\end{array}\right]
\begin{bmatrix}
\boldsymbol{v}_e^{sA} \\ \boldsymbol{p}_e^A \\ \hdashline \boldsymbol{v}_e^{sB} \\ \boldsymbol{p}_e^B \\ \hdashline \boldsymbol{\lambda}_e^s \\ \boldsymbol{\lambda}_e^f
\end{bmatrix}
$$

$$
+\sum_{e=1}^{n_{el}}
\begin{bmatrix}
\boldsymbol{w}_e^A \\ \boldsymbol{q}_e^A \\ \hdashline \boldsymbol{w}_e^B \\ \boldsymbol{q}_e^B \\ \hdashline \boldsymbol{s}_e^s \\ \boldsymbol{s}_e^f
\end{bmatrix}^T
\left[\begin{array}{cc:cc:cc}
\boldsymbol{k}_e^A & \boldsymbol{0} & \boldsymbol{0} & \boldsymbol{0} & \boldsymbol{0} & \boldsymbol{0} \\
\boldsymbol{0} & \boldsymbol{0} & \boldsymbol{0} & \boldsymbol{0} & \boldsymbol{0} & \boldsymbol{0} \\ \hdashline
\boldsymbol{0} & \boldsymbol{0} & \boldsymbol{k}_e^B & \boldsymbol{0} & \boldsymbol{0} & \boldsymbol{0} \\
\boldsymbol{0} & \boldsymbol{0} & \boldsymbol{0} & \boldsymbol{0} & \boldsymbol{0} & \boldsymbol{0} \\ \hdashline
-\boldsymbol{q}_e^{sAT} & \boldsymbol{0} & -\boldsymbol{q}_e^{sBT} & \boldsymbol{0} & \boldsymbol{0} & \boldsymbol{0} \\
\boldsymbol{0} & \boldsymbol{0} & \boldsymbol{0} & \boldsymbol{0} & \boldsymbol{0} & \boldsymbol{0}
\end{array}\right]
\begin{bmatrix}
\boldsymbol{u}_e^{sA} \\ \boldsymbol{p}_e^A \\ \hdashline \boldsymbol{u}_e^{sB} \\ \boldsymbol{p}_e^B \\ \hdashline \boldsymbol{\lambda}_e^s \\ \boldsymbol{\lambda}_e^f
\end{bmatrix}
$$

$$
=\sum_{e=1}^{n_{el}}
\begin{bmatrix}
\boldsymbol{w}_e^A \\ \boldsymbol{q}_e^A \\ \hdashline \boldsymbol{w}_e^B \\ \boldsymbol{q}_e^B \\ \hdashline \boldsymbol{s}_e^s \\ \boldsymbol{s}_e^f
\end{bmatrix}^T
\begin{bmatrix}
\boldsymbol{f}_{t_e}^A \\ \boldsymbol{f}_{Q_e}^A \\ \hdashline \boldsymbol{f}_{t_e}^B \\ \boldsymbol{f}_{Q_e}^B \\ \hdashline -\boldsymbol{q}_e^{sAT}\boldsymbol{X}^{sA} - \boldsymbol{q}_e^{sBT}\boldsymbol{X}^{sB} \\ \boldsymbol{0}
\end{bmatrix}
\tag{3.38}
$$

The matrix system corresponds to first-order ordinary differential system in time. Before assemble element contributions into a global system, the generalized trapezoidal finite difference scheme is applied to the time-dependent portion or the problem. The time domain is divided into increments Δt between times t_i and t_{i+1} which could be non-uniform. The solid displacement at the current time step is expressed in terms of the displacement at the previous step and a linearly interpolated velocity within the time step,

$$
\boldsymbol{u}_{i+1}^{s\gamma} = \left(\omega \boldsymbol{v}_{i+1}^{s\gamma} + \left(1-\omega\right)\boldsymbol{v}_i^{s\gamma}\right)\Delta t + \boldsymbol{u}_i^{s\gamma}, \quad i = 0,1,2,... \tag{3.39}
$$

The parameter ω ($0 \le \omega \le 1$) controls the accuracy and stability of the integration scheme. For $\omega \ge 0.5$, the integration is implicit, and stable for any time step size. To

preserve the symmetry of the global system, the fifth equation of Eq. (3.38) is divided by $\omega\Delta t$. After substituting Eq. (3.39) into Eq. (3.38), the global system is

$$\left[\begin{array}{cc|cc|cc} \omega\Delta t\boldsymbol{k}^A & -\boldsymbol{a}^A & \boldsymbol{0} & \boldsymbol{0} & -\boldsymbol{q}^{sA} & \boldsymbol{0} \\ -\boldsymbol{a}^{A^T} & -\boldsymbol{b}^A & \boldsymbol{0} & \boldsymbol{0} & \boldsymbol{0} & -\boldsymbol{q}^{fA} \\ \hline \boldsymbol{0} & \boldsymbol{0} & \omega\Delta t\boldsymbol{k}^B & -\boldsymbol{a}^B & -\boldsymbol{q}^{sB} & \boldsymbol{0} \\ \boldsymbol{0} & \boldsymbol{0} & -\boldsymbol{a}^{B^T} & -\boldsymbol{b}^B & \boldsymbol{0} & \boldsymbol{q}^{fB} \\ \hline -\boldsymbol{q}^{sA^T} & \boldsymbol{0} & -\boldsymbol{q}^{sB^T} & \boldsymbol{0} & \boldsymbol{0} & \boldsymbol{0} \\ \boldsymbol{0} & -\boldsymbol{q}^{fA^T} & \boldsymbol{0} & \boldsymbol{q}^{fB^T} & \boldsymbol{0} & \boldsymbol{0} \end{array}\right] \left[\begin{array}{c} \boldsymbol{v}_{i+1}^{sA} \\ \boldsymbol{p}_{i+1}^{A} \\ \hline \boldsymbol{v}_{i+1}^{sB} \\ \boldsymbol{p}_{i+1}^{B} \\ \hline \boldsymbol{\lambda}_{i+1}^{s} \\ \boldsymbol{\lambda}_{i+1}^{f} \end{array}\right] = \left[\begin{array}{c} \boldsymbol{f}_t^A - \boldsymbol{k}^A\left\{(1-\omega)\Delta t\boldsymbol{v}_i^{sA} + \boldsymbol{u}_i^{sA}\right\} \\ \boldsymbol{f}_Q^A \\ \hline \boldsymbol{f}_t^B - \boldsymbol{k}^B\left\{(1-\omega)\Delta t\boldsymbol{v}_i^{sB} + \boldsymbol{u}_i^{sB}\right\} \\ \boldsymbol{f}_Q^B \\ \hline \boldsymbol{f}_C \\ \boldsymbol{0} \end{array}\right] \tag{3.40}$$

where,

$$\boldsymbol{f}_C = -\frac{\boldsymbol{q}_e^{sA^T}}{\omega\Delta t}\left\{(1-\omega)\Delta t\boldsymbol{v}_i^{sA} + \boldsymbol{u}_i^{sA} + \boldsymbol{X}^{sA}\right\} - \frac{\boldsymbol{q}_e^{sB^T}}{\omega\Delta t}\left\{(1-\omega)\Delta t\boldsymbol{v}_i^{sB} + \boldsymbol{u}_i^{sB} + \boldsymbol{X}^{sB}\right\}. \tag{3.41}$$

For an evolving contact problem, the fully implicit time integration scheme ($\omega = 1$) is recommended so that the solid velocity can be precisely traced [18].

The matrices are assembled by a standard finite element assembly procedure, and results in a system of equations comparable to the above, but without the subscript '*e*'. At each time step, the solution from the previous time step is used to update the right hand side of Eq. (3.40). For an evolving contact problem, since the correct contact area is not known *a priori*, the problem is solved iteratively using estimated contact areas, while updating the left hand side, until the solution satisfies the Kuhn-Tucker conditions. Details of this procedure are given later.

3.2.4 An Alternative Kinematic Variable Based Formulation

Among the four contact continuity conditions, Eqs. (2.54) - (2.57), the Lagrange multipliers were used in the previous formulation to enforce continuity of the two derived quantities (relative fluid velocity and normal traction). The other two conditions on the primary variables in the *v-p* formulation (current solid position and pressure) were directly introduced in the weighted residual. This strategy groups the four contact continuity conditions into those involving primary variables and those involving derived variables. Symmetry of the global system is obtained.

Alternatively, the contact continuity conditions can be classified as those involving kinematic variables (current solid position and relative fluid velocity) and those involving kinetic variables (pressure and normal traction) continuities. In the alternate formulation, the Lagrange multipliers are defined on the kinetic variables,

$$\lambda^f = p^A, \tag{3.42}$$

$$\lambda^f = p^B. \tag{3.43}$$

$$\lambda^s = \sigma_{ij}^{EA} n_i^A n_j^A, \tag{3.44}$$

$$\lambda^s = \sigma_{ij}^{EB} n_i^B n_j^B. \tag{3.45}$$

Note that the Lagrange multiplier for solid phase λ^s remains unchanged from the previous formulation. The finite element formulation from these definitions is called the 'kinematic variable based' formulation, and the previous is called the 'primary variable based' formulation.

The weighted residual statement is similarly stated. Contributions from body 'A' are now,

$$G^A = \int_{\Omega^A} w_i^A \left(\sigma_{ij,j}^{EA} - p_{,i}^A\right) \mathrm{d}\Omega + \int_{\Omega^A} q^A \left(v_i^{sA} - \kappa^A p_{,i}^A\right)_{,i} \mathrm{d}\Omega$$

$$+ \int_{\Gamma_t^A} s_i^A \left(\overline{t}_i^A - \left(\sigma_{ij}^{EA} - p^A \delta_{ij}\right) n_j^A\right) \mathrm{d}\Gamma + \int_{\Gamma_Q^A} o^A \left(\overline{Q}^A + \kappa^A p_{,i}^A n_i^A\right) \mathrm{d}\Gamma \tag{3.46}$$

$$\int_{\Gamma_C^A} r^{fA} \left(\lambda^f - p^A\right) \mathrm{d}\Gamma + \int_{\Gamma_C^A} r^{sA} \left(\lambda^s - \sigma_{ij}^{EA} n_i^A n_j^A\right) \mathrm{d}\Gamma .$$

Following the same procedures as in the primary variable based formulation, and choosing the weighting functions as $s_i^A = w_i^A$, $o^A = q^A$, $r^{fA} = q_{,i}^A n_i^A \kappa^A$ and $r^{sA} = w_k^A n_k^A$, Eq. (3.46) becomes,

$$G^A = -\int_{\Omega^A} w_{(i,j)}^A \sigma_{ij}^{EA} \mathrm{d}\Omega + \int_{\Omega^A} w_{i,i}^A p^A \mathrm{d}\Omega + \int_{\Omega^A} q^A v_{i,i}^{sA} \mathrm{d}\Omega - \int_{\Gamma_C} q^A \kappa^A p_{,i}^A n_i^A \mathrm{d}\Omega + \int_{\Omega^A} q_{,i}^A \kappa^A p_{,i}^A \mathrm{d}\Omega$$

$$+ \int_{\Gamma_t^A} w_i^A \overline{t}_i^A \mathrm{d}\Gamma + \int_{\Gamma_Q^A} q^A \overline{Q}^A \mathrm{d}\Gamma + \int_{\Gamma_C^A} q_{,i}^A n_i^A \kappa^A \lambda^f \mathrm{d}\Gamma - \int_{\Gamma_C^A} q_{,i}^A n_i^A \kappa^A p^A \mathrm{d}\Gamma + \int_{\Gamma_C^A} w_k^A n_k^A \lambda^s \mathrm{d}\Gamma$$

(3.47)

Contributions from body 'B', G^B, can be derived in the same manner. With the alternative definitions of Lagrange multipliers, contributions from the contact boundary, G^C, are composed of the weighted continuity constraints of current solid position and relative fluid velocity. The complete weak form of the kinematic variable based formulation is given by,

$$\int_{\Omega^A} w_{(i,j)}^A \sigma_{ij}^{EA} \mathrm{d}\Omega - \int_{\Omega^A} w_{i,i}^A p^A \mathrm{d}\Omega - \int_{\Omega^A} q^A v_{i,i}^{sA} \mathrm{d}\Omega + \int_{\Gamma_C} q^A \kappa^A p_{,i}^A n_i^A \mathrm{d}\Omega - \int_{\Omega^A} q_{,i}^A \kappa^A p_{,i}^A \mathrm{d}\Omega$$

$$- \int_{\Gamma_t^A} w_i^A \overline{t}_i^A \mathrm{d}\Gamma - \int_{\Gamma_Q^A} q^A \overline{Q}^A \mathrm{d}\Gamma - \int_{\Gamma_C^A} q_{,i}^A n_i^A \kappa^A \lambda^f \mathrm{d}\Gamma + \int_{\Gamma_C^A} q_{,i}^A n_i^A \kappa^A p^A \mathrm{d}\Gamma - \int_{\Gamma_C^A} w_k^A n_k^A \lambda^s \mathrm{d}\Gamma$$

$$\int_{\Omega^B} w_{(i,j)}^B \sigma_{ij}^{EB} \mathrm{d}\Omega - \int_{\Omega^B} w_{i,i}^B p^B \mathrm{d}\Omega - \int_{\Omega^B} q^B v_{i,i}^{sB} \mathrm{d}\Omega + \int_{\Gamma_C} q^B \kappa^B p_{,i}^B n_i^B \mathrm{d}\Omega - \int_{\Omega^B} q_{,i}^B \kappa^B p_{,i}^B \mathrm{d}\Omega$$

$$-\int_{\Gamma_t^B} w_i^B \overline{t}_i^B \mathrm{d}\Gamma - \int_{\Gamma_Q^B} q^B \overline{Q}^B \mathrm{d}\Gamma - \int_{\Gamma_C^B} q_{,i}^B n_i^B \kappa^B \lambda^f \mathrm{d}\Gamma + \int_{\Gamma_C^B} q_{,i}^B n_i^B \kappa^B p^B \mathrm{d}\Gamma - \int_{\Gamma_C^B} w_k^B n_k^B \lambda^s \mathrm{d}\Gamma$$

$$-\int_{\Gamma_C} s^s \left\{ \left(u_i^{sA} + X_i^{sA} \right) n_i^A + \left(u_i^{sB} + X_i^{sB} \right) n_i^B \right\} \mathrm{d}\Gamma - \int_{\Gamma_C} s^f \left(\kappa^A p_{,i}^A n_i^A + \kappa^B p_{,i}^B n_i^B \right) \mathrm{d}\Gamma = 0 \,. \tag{3.48}$$

The global matrix form can then be constructed as,

$$\left[\begin{array}{cc|cc|cc} \omega\Delta t \boldsymbol{k}^A & -\boldsymbol{a}^A & \boldsymbol{0} & \boldsymbol{0} & -\boldsymbol{q}^{sA} & \boldsymbol{0} \\ -\boldsymbol{a}^{A^T} & -\boldsymbol{b}^A + \boldsymbol{c}^A + \boldsymbol{c}^{A^T} & \boldsymbol{0} & \boldsymbol{0} & \boldsymbol{0} & -\boldsymbol{q}^{fA} \\ \hline \boldsymbol{0} & \boldsymbol{0} & \omega\Delta t \boldsymbol{k}^B & -\boldsymbol{a}^B & -\boldsymbol{q}^{sB} & \boldsymbol{0} \\ \boldsymbol{0} & \boldsymbol{0} & -\boldsymbol{a}^{B^T} & -\boldsymbol{b}^B + \boldsymbol{c}^B + \boldsymbol{c}^{B^T} & \boldsymbol{0} & \boldsymbol{q}^{fB} \\ \hline -\boldsymbol{q}^{sA^T} & \boldsymbol{0} & -\boldsymbol{q}^{sB^T} & \boldsymbol{0} & \boldsymbol{0} & \boldsymbol{0} \\ \boldsymbol{0} & -\boldsymbol{q}^{fA^T} & \boldsymbol{0} & \boldsymbol{q}^{fB^T} & \boldsymbol{0} & \boldsymbol{0} \end{array}\right] \left[\begin{array}{c} \boldsymbol{v}_{i+1}^{sA} \\ \boldsymbol{p}_{i+1}^A \\ \hline \boldsymbol{v}_{i+1}^{sB} \\ \boldsymbol{p}_{i+1}^B \\ \hline \boldsymbol{\lambda}_{i+1}^s \\ \boldsymbol{\lambda}_{i+1}^f \end{array}\right]$$

$$= \left[\begin{array}{c} \boldsymbol{f}_t^A - \boldsymbol{k}^A \left\{ \left(1-\omega\right) \Delta t \boldsymbol{v}_i^{sA} + \boldsymbol{u}_i^{sA} \right\} \\ \boldsymbol{f}_Q^A \\ \hline \boldsymbol{f}_t^B - \boldsymbol{k}^B \left\{ \left(1-\omega\right) \Delta t \boldsymbol{v}_i^{sB} + \boldsymbol{u}_i^{sB} \right\} \\ \boldsymbol{f}_Q^B \\ \hline \boldsymbol{f}_C \\ \boldsymbol{0} \end{array}\right]. \tag{3.49}$$

The element matrices, $\boldsymbol{a}_e^\gamma$, $\boldsymbol{b}_e^\gamma$, $\boldsymbol{k}_e^\gamma$, $\boldsymbol{q}_e^{s\gamma}$, and force vectors, $\boldsymbol{f}_{t_e}^\gamma$, $\boldsymbol{f}_{Q_e}^\gamma$, $\boldsymbol{f}_C$ are identical to the primary variable based formulation (see Eqs. (3.36), (3.37) and (3.41)), but the element contact matrix for the fluid phase, $\boldsymbol{q}_e^{f\gamma}$, and additional element matrix, $\boldsymbol{c}_e^\gamma$, are now given by,

$$\boldsymbol{q}_e^{f\gamma} = \int_{\Gamma_{C_e}} \left(L_\nabla^{sca} \mathbf{N}_p^\gamma \right)^T \boldsymbol{n}^\gamma \boldsymbol{\kappa}^\gamma \mathbf{M}^f \mathrm{d}\Gamma \,, \quad \gamma = A, B \,, \tag{3.50}$$

$$\boldsymbol{c}_e^\gamma = \int_{\Gamma_{C_e}^\gamma} \left(L_\nabla^{sca} \mathbf{N}_p^\gamma \right)^T \boldsymbol{n}^\gamma \boldsymbol{\kappa}^\gamma \mathbf{N}_p^\gamma \mathrm{d}\Gamma \,, \quad \gamma = A, B \,, \tag{3.51}$$

Note that this formulation also preserves symmetry of the global system. Comparison of the two formulations will be discussed in Chapter 4 in terms of issues such as stability and convergence.

Figure 3.1 illustrates that the domain and boundary are discretized into n_{el} finite elements of domain Ω_e^γ and boundary Γ_e^γ. In the *v-p* contact formulation, a ten-node tetrahedral element is used for the 3D analysis of each biphasic body; quadratic interpolation is used for solid velocity and linear interpolation for pressure. Solid velocity degrees of freedom (DOF) are specified on all four vertices and six mid-edges (10 nodes × 3 DOF per node), and pressure DOF are specified at four vertices (4 nodes × 1 DOF). Hence, total DOF per element is 34. This class of element is called a Taylor-Hood element and satisfies the *Babuska-Brezzi*, or *LBB*, *stability condition* for mixed formulations [38]. The contact surface is discretized in such a way that the contact element coincides with one of four triangular surfaces of the tetrahedron from the body '*A*'. This idea becomes clear when contact surface calculations are explained in a later section. Also, details of selecting interpolation functions for the Lagrange multipliers will be discussed in the next chapter, where the finite element completeness and stability are considered.

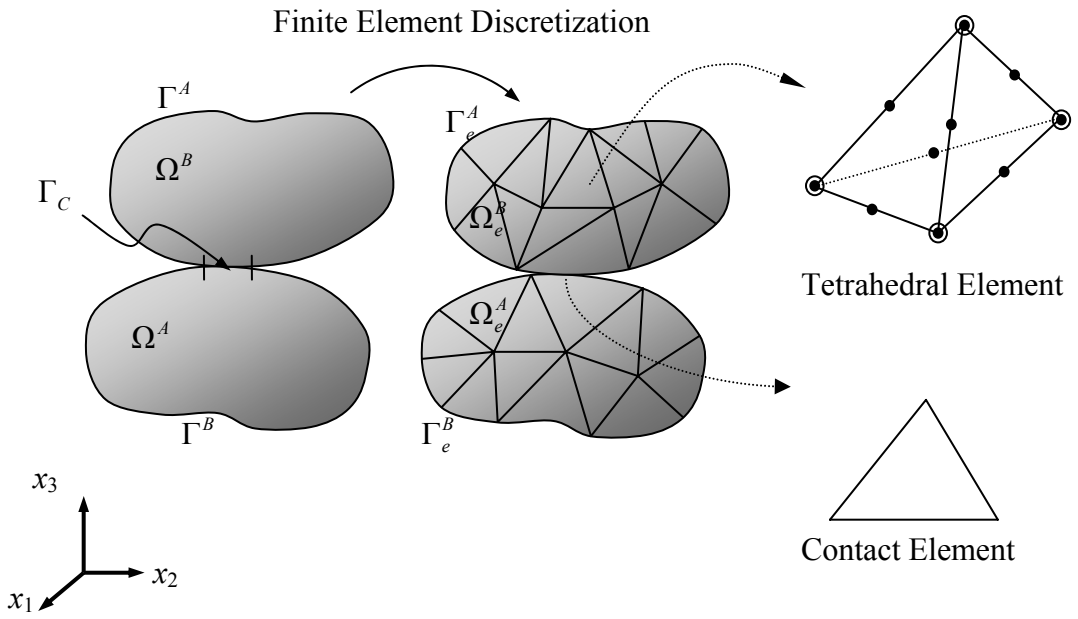

Figure 3.1 Finite element discretization with tetrahedral and contact elements for the 3D v-p contact formulation (solid circle represents solid velocity DOF, and hollow circle represents pressure DOF).

3.3 Contact Element Matrix Calculations and Contact Iteration

There are several steps in the numerical procedure used to calculate the contact matrices. First, an assumption is made that a specific pair of surfaces of body 'A' and 'B' is known to be in contact prior to the next step of the analysis. One of the surfaces plays a role of the contactor surface, and the other becomes the target surface. As a matter of convenience, the contactor surface is always defined on body 'A' and the target surface on body 'B'. The contact surface (on which Lagrange multipliers are interpolated) is aligned with the contactor surface (on body "A') and is discretized into the 2D triangular elements aligned to the mesh faces of the tetrahedral elements of body 'A'.

For purposes of describing the numerical procedures, the element contact matrices are repeated here,

$$\boldsymbol{q}_e^{s\gamma} = \int_{\Gamma_{C_e}} \mathbf{N}^{\gamma T} \boldsymbol{n}^{\gamma} \mathbf{M}^{s} \mathrm{d}\Gamma \,, \quad \gamma = A, B \,, \tag{3.52}$$

$$\boldsymbol{q}_e^{f\gamma} = \int_{\Gamma_{C_e}} \mathbf{N}_p^{\gamma T} \mathbf{M}^{f} \mathrm{d}\Gamma \;\text{ or }\; \int_{\Gamma_{C_e}} \left(L_{\nabla}^{sca} \mathbf{N}_p^{\gamma} \right)^T \boldsymbol{n}^{\gamma} \boldsymbol{\kappa}^{\gamma} \mathbf{M}^{f} \mathrm{d}\Gamma \,, \quad \gamma = A, B \,. \tag{3.53}$$

Since the contact matrices will be numerically integrated, all necessary information for calculation needs to be referenced to the Gauss quadrature points. Note that all contact integrals, regardless of its polynomial order, are numerically evaluated using 7-point Gauss quadrature formula [38] with degree of precision of 4. At each quadrature point in the contactor elements, the closest point projection to the target elements, also called the gap function, is calculated (illustrated in Fig. 3.2).

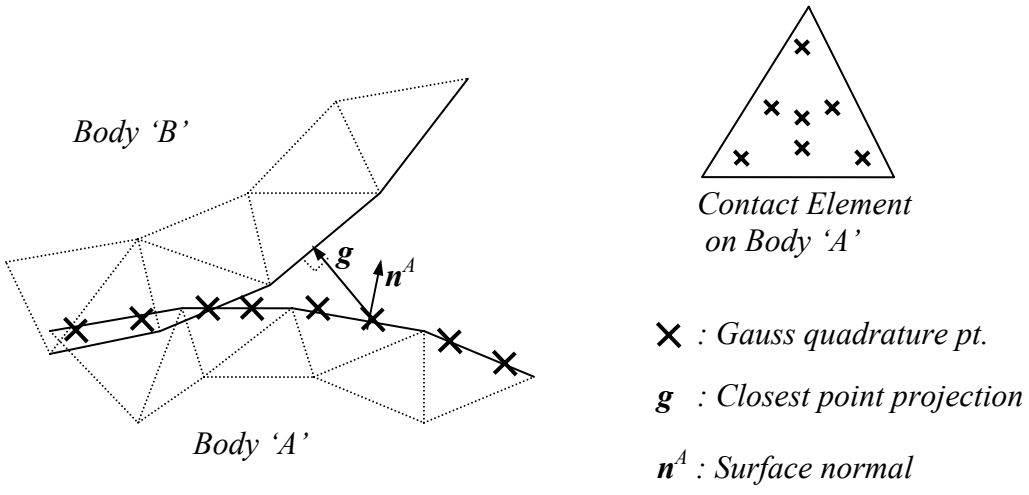

Figure 3. 2 The closest point projection from a Gauss quadrature point on the contactor surface (on Body 'A') to the target surface (on Body 'B').

If the gap function is smaller than the user specified gap tolerance, the contact status of that quadrature point is assumed to be 'active'. Otherwise, the point is assumed to be 'inactive'. If more than three quadrature points out of the seven points within a contact element is classified as active, the contact element becomes an active element and the degrees of freedom for the Lagrange multipliers are created. The number 'three' has been practically chosen to avoid matrix singularity due to numerical integration [93]. For the active contact elements, the integrations of Eqs. (3.52) and (3.53) are numerically evaluated at the active quadrature points, but there is no contribution from the other inactive points.

Once the contact element matrices are calculated for the assumed contact surface, the global system, Eq. (3.40) (or Eq. (3.49)), is solved, and the contact status of each quadrature point is re-evaluated based on the Kuhn-Tucker conditions. In both formulations, the continuity constraints are satisfied on the assumed contact surface. If the assumed contact surface is larger than the correct contact area, the solution may result in tensile tractions in the assumed contact area. On the other hand, if the assumed contact surface is smaller than the actual contact surface, penetration may occur outside of the assumed area. Both cases violate the Kuhn-Tucker conditions and require that the contact status be adjusted, and the contact matrices be calculated upon the updated status. This iterative process continues until the solution excludes all physically unacceptable behaviors. Figure 3.3 illustrate the algorithm for contact calculation.

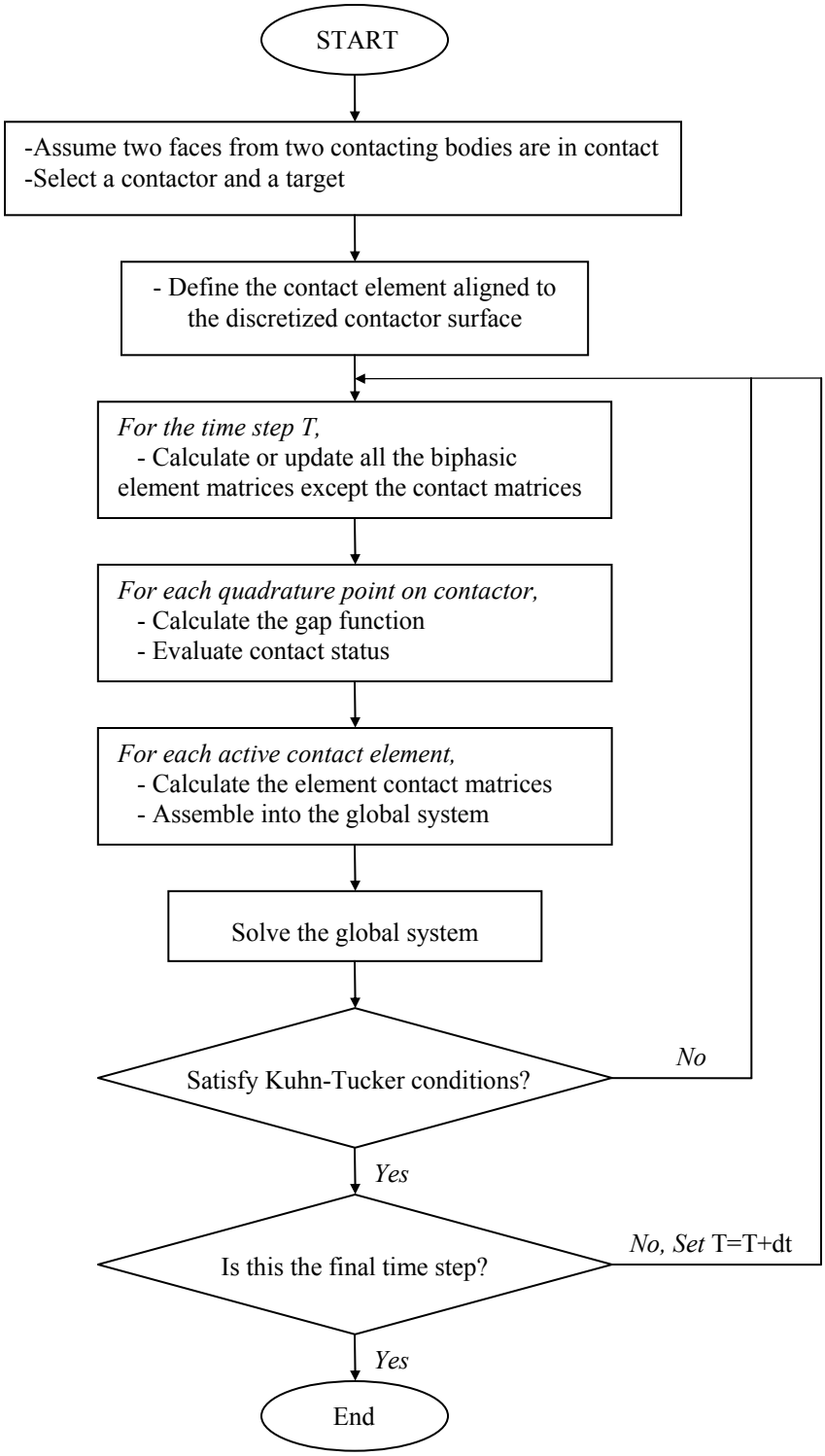

Figure 3.3 A contact iteration algorithm for the biphasic contact analysis.

3.4 Contact Search Algorithm

Contact searching algorithms can contribute substantially to the CPU time of a contact analysis. They can be broadly categorized as either global or local searches [32, 62]. Global searches group the candidate target elements with every contactor point. Local searches calculate the gap function from a contactor point to the candidate target elements, and store the necessary information for contact matrix calculations.

In the current study, minimal attention has been given to optimizing the search methods, and the two search procedures are combined as briefly described in the following. For each quadrature point on the contactor elements, projection is made normal to the candidate target elements. Once the closest point projection is found (see Figure 3.2), five sets of data are stored for the contact matrix calculation: the closest point projection (or gap function), a surface normal on the contactor element, a flag for contact status, the local coordinate of the quadrature point and the local coordinate of the projected point on the target element. Next, if the product of gap function and surface normal is smaller than the user specified gap tolerance, the contact status flag is classified as ‘active’. Otherwise, it is classified as ‘inactive’. Thereafter, the contact matrices will be calculated.

During the linear analysis, solving the global linear system is observed to be more critical bottle-neck in terms of CPU time compared to the contact search. The needs for the more efficient search algorithm are inevitable, when the size of problem increases with mesh refinement, or when repetitive solution is necessary for nonlinear analysis.

Chapter 4: A Biphasic Contact Patch Test to Select the Interpolation Functions for the Lagrange Multipliers

4.1 Introduction

In the current contact formulations, two contact continuity conditions among four are introduced using Lagrange multipliers. The other two are introduced directly in the weighted residual. The constraints introduced by Lagrange multipliers are enforced by solving for a common Lagrange multiplier on the shared contact surface. In order to ensure that the approximate Galerkin solution from this strategy converge to the exact solution with mesh refinement, shape functions for the Lagrange multipliers must be selected so that convergence requirements are satisfied.

Convergence requires that the shape functions be *conforming* (or *compatible*) and *complete* [38, 93]. However, these requirements are rarely guaranteed in contact problems since, among other reasons, the finite element meshes are generally not node-to-node aligned between two contacting surfaces. In such a case, it is difficult to choose a shape function within the contact element that satisfies the above convergence requirements. An exception would involve remeshing bodies 'A' and 'B' in the assumed contact area to produce node to node contact. Such an approach was not explored in this study.

Another, more practical, way to ensure convergence is to verify *consistency* and *stability* of an algorithm. Zienkiewicz *et al*. [92] extended the idea of Irons' patch test

[41] to mixed formulations to identify the necessary and sufficient conditions for convergence. Later, Taylor *et al.* [81] proposed the contact patch test shown in Figure 4.1 (a) to assess the robustness of their contact methodology. In the test, exact transmission of constant normal traction, as calculated by the contact algorithm across the contact surface, is examined as a finite element completeness check.

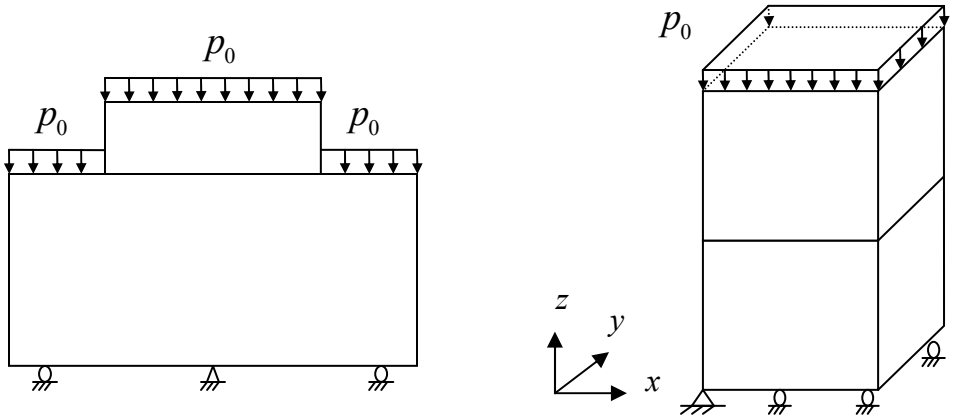

Figure 4. 1 (a) The original contact patch test, (b) A biphasic contact patch test in 3D

4.2 Biphasic Contact Patch Test

In order to examine the current three-dimensional biphasic contact formulations, the biphasic contact patch test depicted in Figure 4.1 (b) was devised. In the test, two biphasic cubes ($1\times1\times1$ mm^3) are positioned vertically with an initial gap of 0.0001 mm. A uniform traction, $p_0 = -0.00675$ MPa, is applied on the uppermost surface through which fluid can freely exude with a zero hydrostatic pressure boundary condition. The surfaces on the *x*-, *y*- and *z*-planes (*i.e.*, $x = 0$, $y = 0$ and $z = 0$) are prescribed with the *x*-,

y- and *z*-symmetry boundary conditions, respectively, thus allowing no flow or motion normal to the surface. To simplify the test, material properties are chosen to preclude time-dependent behavior of a biphasic material. This, of course, has the tendency to emphasize the solid-related Lagrange multiplier and minimize the influence of the fluid-related Lagrange multiplier. However, as will be seen, the same strategy is used for selecting interpolations for both Lagrange multipliers, and the constraint counts and ratios therefore show similar trends. This computationally more efficient near-solid version of a biphasic contact patch test was therefore found to provide reliable guidance for both Lagrange multipliers. However, in principle, there is no limitation on the use of physiological appropriate biphasic tissue properties. For the present test, both cubes have the same properties: Young's modulus E = 0.675 MPa, Poisson's ratio ν = 0.125, permeability $\kappa = 5.0\times10^{3}$ mm^4/N/sec and solid content $\phi^s = 0.99$.

With the above problem setup, the finite element solution is expected to yield a total strain of 1 %, i.e., $\varepsilon_{zz} = 0.01$, that is uniformly developed throughout both cubes. Normal stress and current position should be continuous across the contact surface. Also, pressure and relative fluid flow continuity conditions should be satisfied, although fluid effect is minimal here.

The strategy used in this test was to first screen interpolation functions using meshes with node-to-node alignment on the contact surface, then consider non-aligned meshes. Table 4.1 lists the finite element meshes for the test where all contact elements are node-to-node aligned. Figure 4.2 shows the each mesh on the contact surface. Although this configuration is restrictive for general contact situations, many important

issues will be discussed in regard of choosing interpolating functions for Lagrange multipliers.

	MESH A	MESH B	MESH C	MESH D
Total Number of Tetrahedral Biphasic Elements	12	24	118	152
Total Number of Triangular Contact Elements	2	4	8	12

Table 4. 1 Mesh configurations for the biphasic contact patch test.

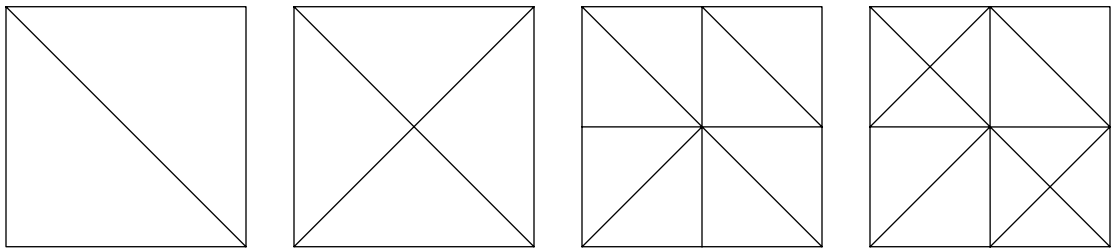

Figure 4. 2 Meshes on the contact surface for (a) MESH A, (b) MESH B, (c) MESH C and (d) MESH D.

4.3 Selecting Interpolating Functions for Lagrange Multipliers

The interpolations for Lagrange multipliers should be chosen in such a way that the defined quantities are well approximated and also that the associated contact continuity conditions are accurately satisfied within the formulation. There are three

conditions that the interpolating function should satisfy: (i) The interpolating function for the Lagrange multipliers should have sufficient interpolating power to reproduce the defined quantities. (ii) There should be sufficient constraining equations to enforce the contact continuity conditions not associated with the Lagrange multipliers. (iii) The resulting global system should be non-singular. In the first part of this chapter, the primary variable based formulation will be used to develop the conceptual framework, then the kinematic variable based formulation will be studied.

Condition (i) suggests that the interpolating functions be able to appropriately approximate the defined quantities. For the tetrahedral element used with the *v-p* formulation in this study, a continuous quadratic function is used to interpolate solid velocity and displacement, and a continuous linear function is used for pressure. Therefore, normal solid stress becomes a discontinuous linear function in terms of the gradient of solid displacement. The relative fluid flow becomes a discontinuous constant function in terms of the pressure gradient on element surfaces. Figure 4.3 illustrates the gradient of element displacement field and the gradient of element pressure field on the contact surface.

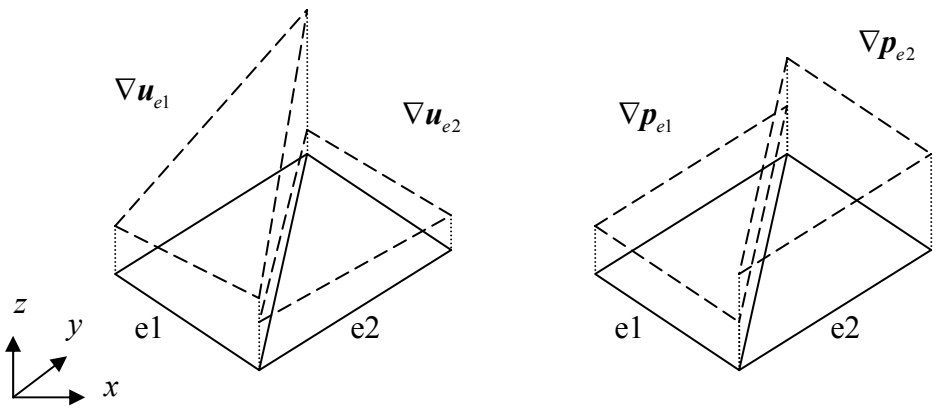

(a) (b)

Figure 4. 3 (a) Gradient of element displacement field, (b) Gradient of element pressure field in the Taylor Hood element.

A more mathematical argument can also be made for condition (i). For illustration purpose, consider λ^s and normal traction continuity on Γ_C. This continuity is enforced by the term in the weighted residual, Eq. (3.15),

$$\int_{\Gamma_C^A} r^{sA}\left(\lambda^s - \sigma_{ij}^{EA} n_i^A n_j^A\right) \mathrm{d}\Gamma = 0\,, \tag{4.1}$$

on Γ_C^A from body 'A'. Eventually, interpolations are introduced in the weak form, Eq. (3.21), which if introduced here, would produce

$$\boldsymbol{c}_e^{\,T} \int_{\Gamma_{C_e}^A} \mathbf{M}^{sT} \mathbf{M}^s \mathrm{d}\Gamma \boldsymbol{\lambda}_e^s - \boldsymbol{c}_e^{\,T} \int_{\Gamma_{C_e}^A} \mathbf{M}^{sT} \mathbf{N}_t^A \mathrm{d}\Gamma\, \boldsymbol{t}_e^{sA}\,. \tag{4.2}$$

Note that the term, $\mathbf{N}_t^A \boldsymbol{t}_e^{sA}$, is used to represent that normal traction on Γ_C^A could be written as polynomial of known order and in terms of independent traction-type coefficients that are in fact a subset of the displacement degrees of freedom (DOF). For

example, in our quadratic displacement tetrahedral elements, $\mathbf{N}_t^A \boldsymbol{t}_e^{sA}$ is a discontinuous linear function with three independent traction coefficients.

After assembling all contributions on Γ_C^A, Eq. (4.2) takes on the form,

$$\boldsymbol{c}^T \left(\boldsymbol{P}^A \boldsymbol{\lambda}^s - \boldsymbol{R}^A \boldsymbol{t}_e^{sA} \right) = 0 . \tag{4.3}$$

The matrices, $\boldsymbol{P}^A$ and $\boldsymbol{R}^A$, come from the appropriate integrals in Eq. (4.2). A similar construction can be made for body 'B' on Γ_C^B,

$$\boldsymbol{c}^T \left(\boldsymbol{P}^B \boldsymbol{\lambda}^s - \boldsymbol{R}^B \boldsymbol{t}_e^{sB} \right) = 0 . \tag{4.4}$$

Assuming node to node contact, the matrices become $\boldsymbol{P}^A = \boldsymbol{P}^B = \boldsymbol{P}$ and $\boldsymbol{R}^A = \boldsymbol{R}^B = \boldsymbol{R}$. Substituting, assuming $\boldsymbol{c}$ is arbitrary and non-zero, and subtracting Eq. (4.4) from Eq. (4.3) yields

$$\boldsymbol{R}\left(\boldsymbol{t}^{sA} - \boldsymbol{t}^{sB} \right) = 0 . \tag{4.5}$$

Since the interpolation of r^s and λ^s use the same polynomials, the number of equations in Eq. (4.5) will be equal to the number of independent λ^s parameters. Thus, in order for Eq. (4.5) to suggest a unique satisfaction of normal traction continuity on Γ_C, the number of independent λ^s parameters must be greater than or equal to the number of independent traction parameters on Γ_C. A similar argument can be made for the fluid part of condition (i).

Condition (ii) requires that there be a sufficient number of constraining equations to enforce those contact continuity conditions introduced directly into the weighted residual, namely for current position of the solid phase and the pressure. From Eqs.

(3.20), (3.25) and (3.28), note that the continuity condition of current position is weighted by a function that uses the same order interpolating functions as for λ^s. Also, the weighting function applied to the pressure continuity uses the same order interpolating function as for λ^f. Consequently, the number of constraining equations is equal to the number of Lagrange multiplier degrees of freedom. This choice, it should be noted, preserves symmetry of the global system of Eq. (3.40).

Condition (iii) can be monitored using a simple algebraic observation suggested by Zienkiewicz et al. [92]. First, consider λ^s from the global matrix system, Eq. (3.40). Using the first and third equations, $\boldsymbol{v}^{sA}$ and $\boldsymbol{v}^{sB}$ can be eliminated from the fifth equation, which can be written as,

$$\left(\boldsymbol{q}^{sA\mathrm{T}}\boldsymbol{k}^{A^{-1}}\boldsymbol{q}^{sA}+\boldsymbol{q}^{sB\mathrm{T}}\boldsymbol{k}^{B^{-1}}\boldsymbol{q}^{sB}\right)\boldsymbol{\lambda}^s=-\boldsymbol{q}^{sA\mathrm{T}}\boldsymbol{k}^{A^{-1}}\left(\boldsymbol{f}_t^A+\boldsymbol{a}^A\boldsymbol{p}^A\right)-\boldsymbol{q}^{sB\mathrm{T}}\boldsymbol{k}^{B^{-1}}\left(\boldsymbol{f}_t^B+\boldsymbol{a}^B\boldsymbol{p}^B\right). \tag{4.6}$$

Among DOF in the $\boldsymbol{v}^{sA}$ and $\boldsymbol{v}^{sB}$ variables, only the *z*-direction DOF on the contact surface contribute to calculating $\boldsymbol{\lambda}^s$ in the above equation. This is seen by noting the scalar product by the surface normal, $\boldsymbol{n}^A$, in $\boldsymbol{q}^{sA}$, which eliminates contributions from the other directions. This is also true for body 'B'.

If m is the number of *z*-direction DOF in the $\boldsymbol{v}^{sA}$ or $\boldsymbol{v}^{sB}$ variables and n is the number of DOF in the $\boldsymbol{\lambda}^s$ variable, then a necessary condition for non-singularity is

$$m \geq n\,. \tag{4.7}$$

Since $\boldsymbol{k}^A$ (or $\boldsymbol{k}^B$) is non-singular and positive definite, the rank of $\boldsymbol{k}^{A^{-1}}$ (or $\boldsymbol{k}^{B^{-1}}$) cannot be greater than m, nor can the rank of $\boldsymbol{q}^{sA\mathrm{T}}\boldsymbol{k}^{A^{-1}}\boldsymbol{q}^{sA}$ (or $\boldsymbol{q}^{sB\mathrm{T}}\boldsymbol{k}^{B^{-1}}\boldsymbol{q}^{sB}$). This guarantees that

there are more equations than unknowns. Otherwise, if n is greater than m, the global system is rank deficit and will be singular. However, it should be observed that Eq. (4.7) works against the needs of condition (ii). Therefore, if m is excessively larger than n, the contact continuity constraints introduced directly in the weighted residual may not be accurately satisfied.

Also, a sufficient condition for a unique solution, addressed by Zienkiewicz *et al*. [92], can be rewritten as,

$$\boldsymbol{q}^{sA}\boldsymbol{\lambda}^{s} \neq 0 \text{ and } \boldsymbol{q}^{sB}\boldsymbol{\lambda}^{s} \neq 0 \quad \text{for all } \boldsymbol{\lambda}^{s} \neq 0 . \tag{4.8}$$

The proof of this statement can be easily made by pre-multiplying the left hand side of Eq. (4.6) by $\boldsymbol{\lambda}^{s\mathrm{T}}$. Since $\boldsymbol{k}^{A^{-1}}$ and $\boldsymbol{k}^{B^{-1}}$ are positive definite,

$$\boldsymbol{\lambda}^{s\mathrm{T}}\boldsymbol{q}^{sA\mathrm{T}}\boldsymbol{k}^{A^{-1}}\boldsymbol{q}^{sA}\boldsymbol{\lambda}^{s} + \boldsymbol{\lambda}^{s\mathrm{T}}\boldsymbol{q}^{sB\mathrm{T}}\boldsymbol{k}^{B^{-1}}\boldsymbol{q}^{sB}\boldsymbol{\lambda}^{s} > 0 . \tag{4.9}$$

Therefore, the solution of Eq. (4.6) is unique. This condition is equivalent to the statement that the rank of matrix $\boldsymbol{q}^{sA}$ (or $\boldsymbol{q}^{sB}$) is equal to n, which is automatically preserved by a standard finite element descretization. The condition is also called the *solvability* condition [22].

Similarly, the necessary and sufficient conditions for $\boldsymbol{\lambda}^{f}$ can be determined. Using the second and fourth equations of the global system, Eq. **(3.40)**, $\boldsymbol{p}^{A}$ and $\boldsymbol{p}^{B}$ can be eliminated from the sixth equation, which can be written as,

$$\left(\boldsymbol{q}^{fA\mathrm{T}}\boldsymbol{b}^{A^{-1}}\boldsymbol{q}^{fA} + \boldsymbol{q}^{fB\mathrm{T}}\boldsymbol{b}^{B^{-1}}\boldsymbol{q}^{fB}\right)\boldsymbol{\lambda}^{f} = -\boldsymbol{q}^{fA\mathrm{T}}\boldsymbol{b}^{A^{-1}}\left(\boldsymbol{f}_{Q}^{A} + \boldsymbol{a}^{A\mathrm{T}}\boldsymbol{v}^{sA}\right) + \boldsymbol{q}^{fB\mathrm{T}}\boldsymbol{b}^{B^{-1}}\left(\boldsymbol{f}_{Q}^{B} + \boldsymbol{a}^{B\mathrm{T}}\boldsymbol{v}^{sB}\right). \tag{4.10}$$

If o is the number of DOF in the $\boldsymbol{p}^A$ or $\boldsymbol{p}^B$ variables on the contact surface and r is the number of DOF in the $\boldsymbol{\lambda}^f$ variable, then a necessary condition for non-singularity is

$$o \geq r \,. \tag{4.11}$$

Similarly, a sufficient condition becomes

$$\boldsymbol{q}^{fA}\boldsymbol{\lambda}^f \neq 0 \text{ and } \boldsymbol{q}^{fB}\boldsymbol{\lambda}^f \neq 0 \quad \text{for all } \boldsymbol{\lambda}^f \neq 0 \,. \tag{4.12}$$

The pair of necessary and sufficient conditions is often called the stability conditions for the mixed variable problem [92].

Table 4.2 summarizes the descriptions, required ratio and independent parameters for the interpolating functions to satisfy each condition. For the condition (i), the number of λ^s DOF should be larger than the number of independent quantities to define the discontinuous linear function of normal elastic stress. Also, the number of λ^f DOF should be larger than the number of independent quantities to define the discontinuous constant function of relative fluid velocity. In the condition (ii), N_{d_con} and N_{d_eqn} are the number of solid normal displacement DOF to be constrained and the number of equations to enforce this constraint, respectively. And, N_{p_con} and N_{p_eqn} are the numbers of pressure DOF on the contact surface and the number of equations to enforce the pressure constraint, respectively. The condition (iii) examines the necessary condition for non-singularity.

	Condition (i)		Condition (ii)		Condition (iii)	
Description	Enough to approximate the normal elastic stress and relative fluid flow?		Enough equations to constrain the displacement and pressure continuity?		Is it singular?	
Required Ratio	$\frac{\lambda^s}{\sigma_{ij}^E n_i n_j} \geq 1$	$\frac{\lambda^f}{\kappa p_{,i} n_i} \geq 1$	$\frac{N_{d_eqn}}{N_{d_con}} \geq 1$	$\frac{N_{p_eqn}}{N_{p_con}} \geq 1$	$\frac{m}{n} \geq 1$	$\frac{o}{r} \geq 1$
Independent Parameters on Γ_C	$\frac{\lambda^s}{\sigma_{ij}^E n_i n_j} \geq 1$	$\frac{\lambda^f}{\kappa p_{,i} n_i} \geq 1$	$\frac{s^s \text{ or } \lambda^s}{u_z} \geq 1$	$\frac{s^f \text{ or } \lambda^f}{p} \geq 1$	$\frac{u_z}{\lambda^s} \geq 1$	$\frac{p}{\lambda^f} \geq 1$

Table 4. 2 A summary of the conditions (i), (ii) and (iii) of the interpolating functions for Lagrange multipliers for the primary variable based formulation.

There are two strategies that were considered in selecting the interpolations for the Lagrange multiplies. The first possibility is to choose the functions so that the number of independent coefficients in the Lagrange multipliers, and thus the functions that weight the position and pressure continuity conditions introduced directly into the weighted residual, is equal to the number of normal velocity and pressure parameters on the contact surface. This approach will satisfy conditions (ii) and (iii) for all mesh configurations. A natural choice would therefore be a continuous quadratic function for λ^s and a continuous linear function for λ^f. Another possibility is to choose interpolations for Lagrange multipliers based on the continuity quantity they are used to introduce. As shown in Figure 4.3, a natural choice would be a discontinuous linear function for λ^s and a discontinuous constant function for λ^f. In this scenario, condition (i) is automatically satisfied for all mesh configurations, but conditions (ii) and (iii) need to be more closely examined.

Practically, there can be other possibilities to choose the shape functions. The higher order shape functions, such as cubic or quartic, used, the closer satisfaction can be obtained for the condition (i). But, this choice easily violates the condition (iii) and results in severe singularity.

4.3.1 Continuous Interpolating Functions

First consider a set of continuous interpolating functions for the Lagrange multipliers; namely quadratic for λ^s and linear for λ^f. Checking the singularity condition (condition (iii)) is trivial for these functions, as illustrated in Figure 4.4, since the number of u_z^s DOF and λ^s DOF are equal for all test meshes, as are the number of pressure DOF and the number of λ^f.

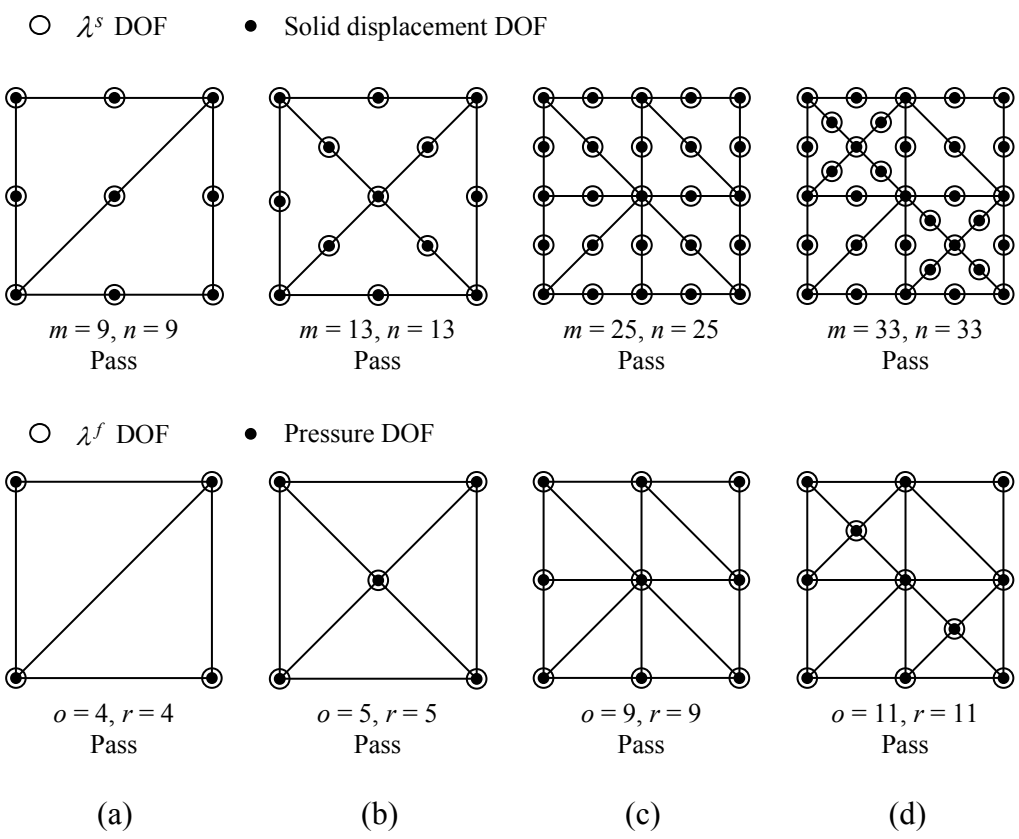

Figure 4. 4 Singularity check for the continuous interpolations for λ^f and λ^s (a solid circle represents a DOF of a primary variable, and a hollow circle represents a DOF of Lagrange multiplier variables) (a) MESH A, (b) MESH B, (c) MESH C and (d) MESH D.

Table 4.3 summarizes the conditions (i), (ii) and (iii) for the four mesh configurations. For condition (i), three DOF for λ^s are needed for each contact element to determine the discontinuous linear stress (see Fig. 4.3). And, one DOF of λ^f is needed to determine the discontinuous constant fluid velocity. For MESH A, B and C, the continuous interpolations are sufficient to approximate the defined quantities. However, as the mesh is further refined, the number of parameters to determine $\sigma_{ij}^E n_i n_j$

and $\kappa p_{,i} n_i$ grow more quickly than the number of DOF for the continuous λ^s and λ^f fields, respectively. For MESH D, there are insufficient Lagrange multiplier DOF.

	Condition (i) Enough Approximating Power		**Condition (ii) Enough Constraining Equations**		**Condition (iii) Non-singularity**	
	$\frac{\lambda^s}{\sigma^E_{ij} n_i n_j} \geq 1$	$\frac{\lambda^f}{\kappa p_{,i} n_i} \geq 1$	$\frac{N_{d_eqn}}{N_{d_con}} \geq 1$	$\frac{N_{p_eqn}}{N_{p_con}} \geq 1$	$\frac{m}{n} \geq 1$	$\frac{o}{r} \geq 1$
	$\frac{\lambda^s}{\sigma^E_{ij} n_i n_j} \geq 1$	$\frac{\lambda^f}{\kappa p_{,i} n_i} \geq 1$	$\frac{s^s \text{ or } \lambda^s}{u_z} \geq 1$	$\frac{s^f \text{ or } \lambda^f}{p} \geq 1$	$\frac{u_z}{\lambda^s} \geq 1$	$\frac{p}{\lambda^f} \geq 1$
MESH A	$\frac{9}{6}$	$\frac{4}{2}$	$\frac{9}{9}$	$\frac{4}{4}$	$\frac{9}{9}$	$\frac{4}{4}$
MESH B	$\frac{13}{12}$	$\frac{5}{4}$	$\frac{13}{13}$	$\frac{5}{5}$	$\frac{13}{13}$	$\frac{5}{5}$
MESH C	$\frac{25}{24}$	$\frac{9}{8}$	$\frac{25}{25}$	$\frac{9}{9}$	$\frac{25}{25}$	$\frac{9}{9}$
MESH D	$\frac{33}{36}$ *	$\frac{11}{12}$ *	$\frac{33}{33}$	$\frac{11}{11}$	$\frac{33}{33}$	$\frac{11}{11}$

*Table 4. 3 Conditions (i), (ii) and (iii) for continuous interpolations for Lagrange multipliers (asterisk * indicates violation of the condition).*

Figures 4.5 – 4.8 show the results for the biphasic contact patch test on the contact boundaries for MESH A to D, respectively. For ease of visualization, results are displayed only on the contact surfaces and the gap between two cubes is exaggerated. For MESH A, the displacement u_z is uniformly developed across the contact surfaces in

Fig. 4.5 (a). As two cubes come in contact, the top surface displaces more than the bottom surface, corresponding to the initial gap of 0.0001 mm. In the figure, however, the amount of initial gap is excluded from the displacement on the top cube, to show the variation of displacement on two contact surfaces with the same scale. Fig. 4.5 (b) shows that the applied compressive traction of 0.00675 MPa is uniformly reproduced on the contact surface. The top surface experiences slightly higher stress, but the difference is negligible.

Although no physical significance is associated with fluid results, given the large permeability, it is worthwhile to examine its continuity. Fig. 4.5 (c) shows that pressure is not uniform on the contact surfaces but its variation is negligibly small. Pressure is continuous between the two bodies. The relative fluid velocity, $w_z = -\kappa p_{,z} n_z$, shown in Fig. 4.5 (d) is uniform across the contact surfaces, but not continuous from the contactor (lower surface) to the target (upper surface). The difference can be explained by the fact that pressure is not uniformly developed in z-direction at the end of one time step, even with a very high permeability. The upper body experience a larger pressure gradient than the lower body does, and it is therefore not surprising to have the observed discrepancy in w_z with only one element through the thickness.

The same observation can be made on the results for MESH B, C and D in Figs 4.6-8. The lack of interpolating power for MESH D (condition (i)) does not degrade the continuity conditions. The discrepancy in w_z is reduced with two elements through the thickness (for MESH C and D). Consequently, it can be concluded that the continuous interpolating functions for λ^s and λ^f show good performance for the current biphasic contact patch test.

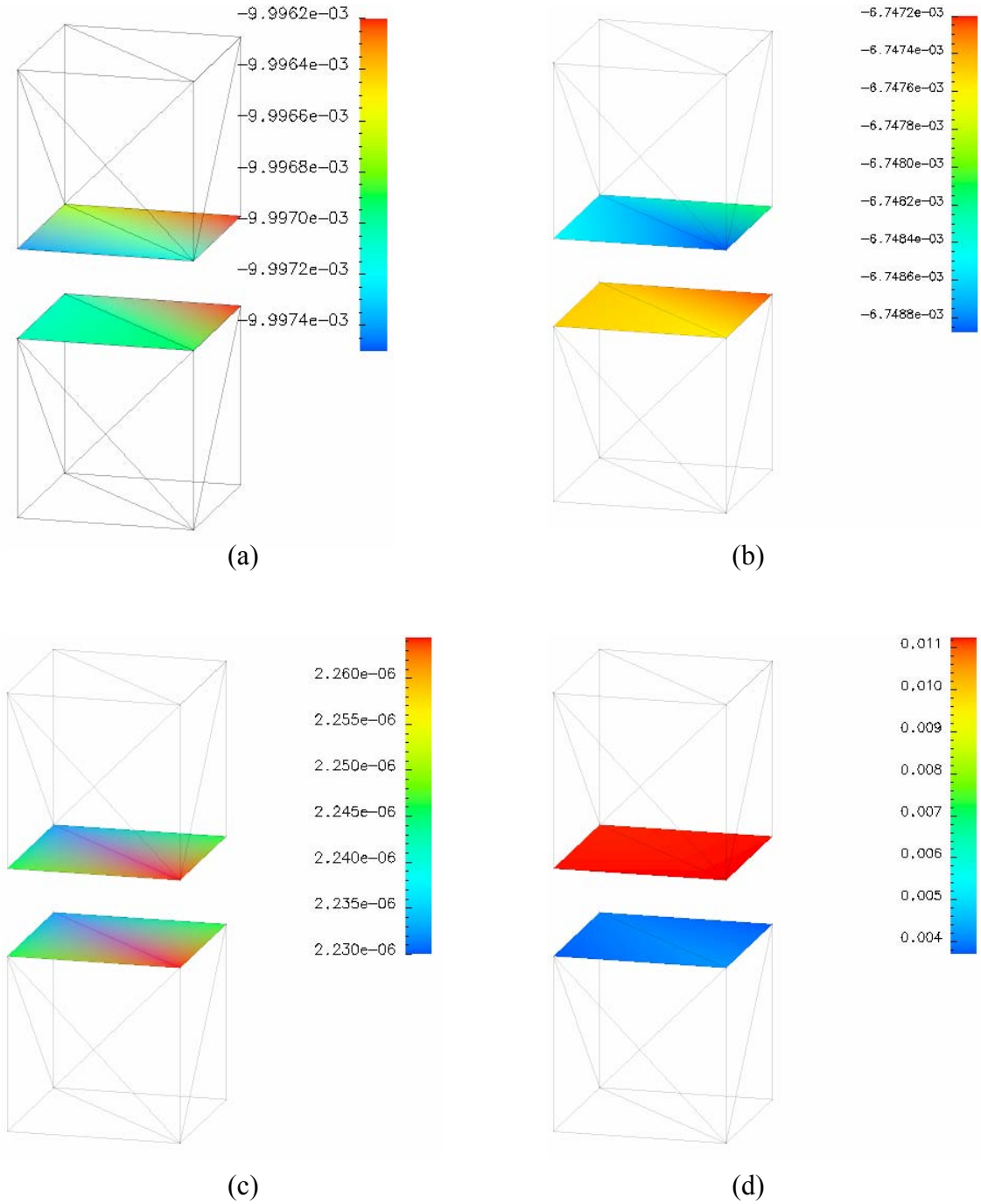

Figure 4. 5 (a) u_z, (b) σ_{zz}^E, (c) p and (d) $-\kappa p_{,z} n_z$ on the contact surfaces using continuous interpolations for Lagrange multipliers with MESH A (units are mm for displacement, MPa for normal stress and pressure, mm/sec for relative fluid velocity).

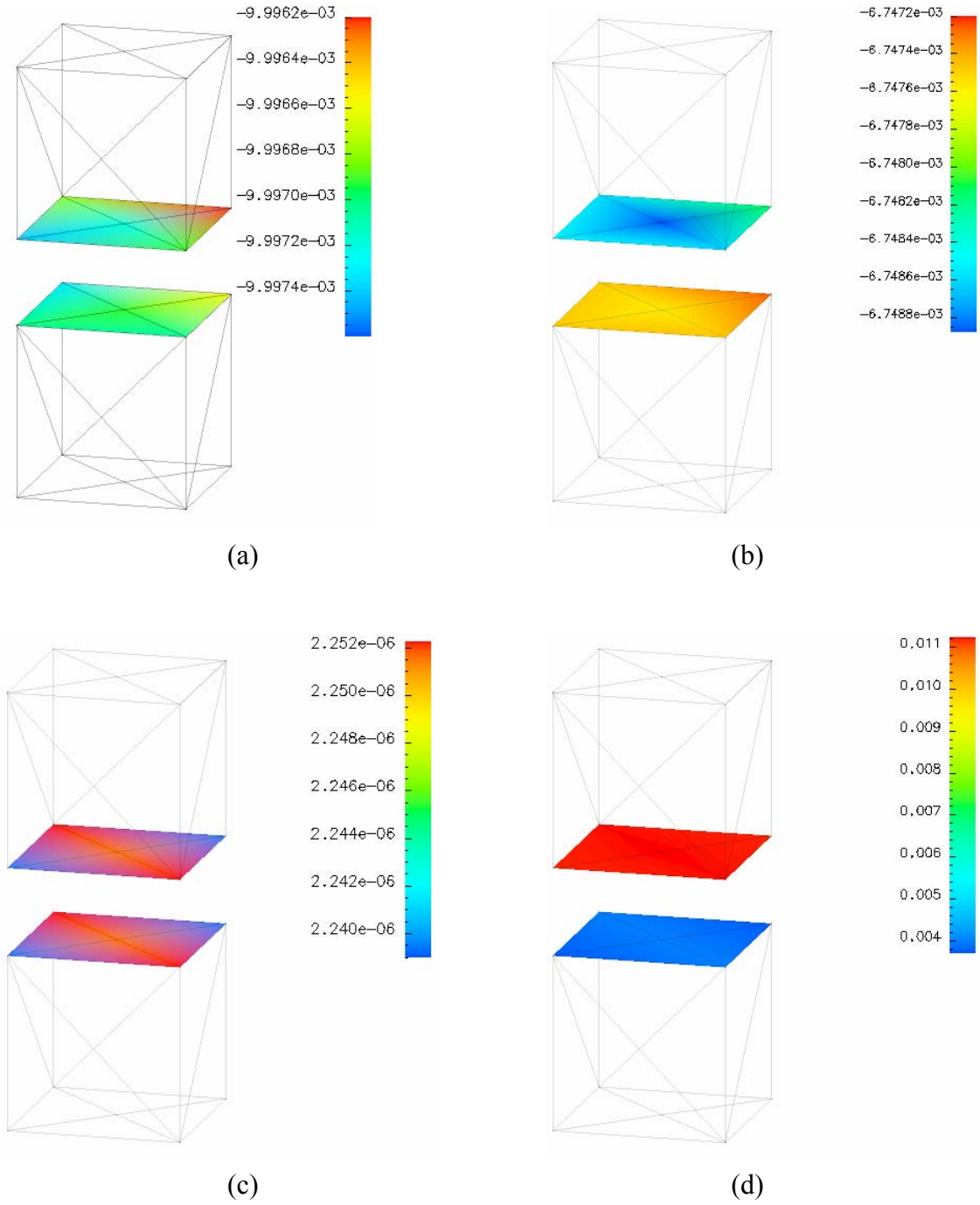

Figure 4. 6 (a) u_z, (b) σ_{zz}^{E}, (c) p and (d) $-\kappa p_{,z} n_z$ on the contact surfaces using continuous interpolations for Lagrange multipliers with MESH B (units are mm for displacement, MPa for normal stress and pressure, mm/sec for relative fluid velocity).

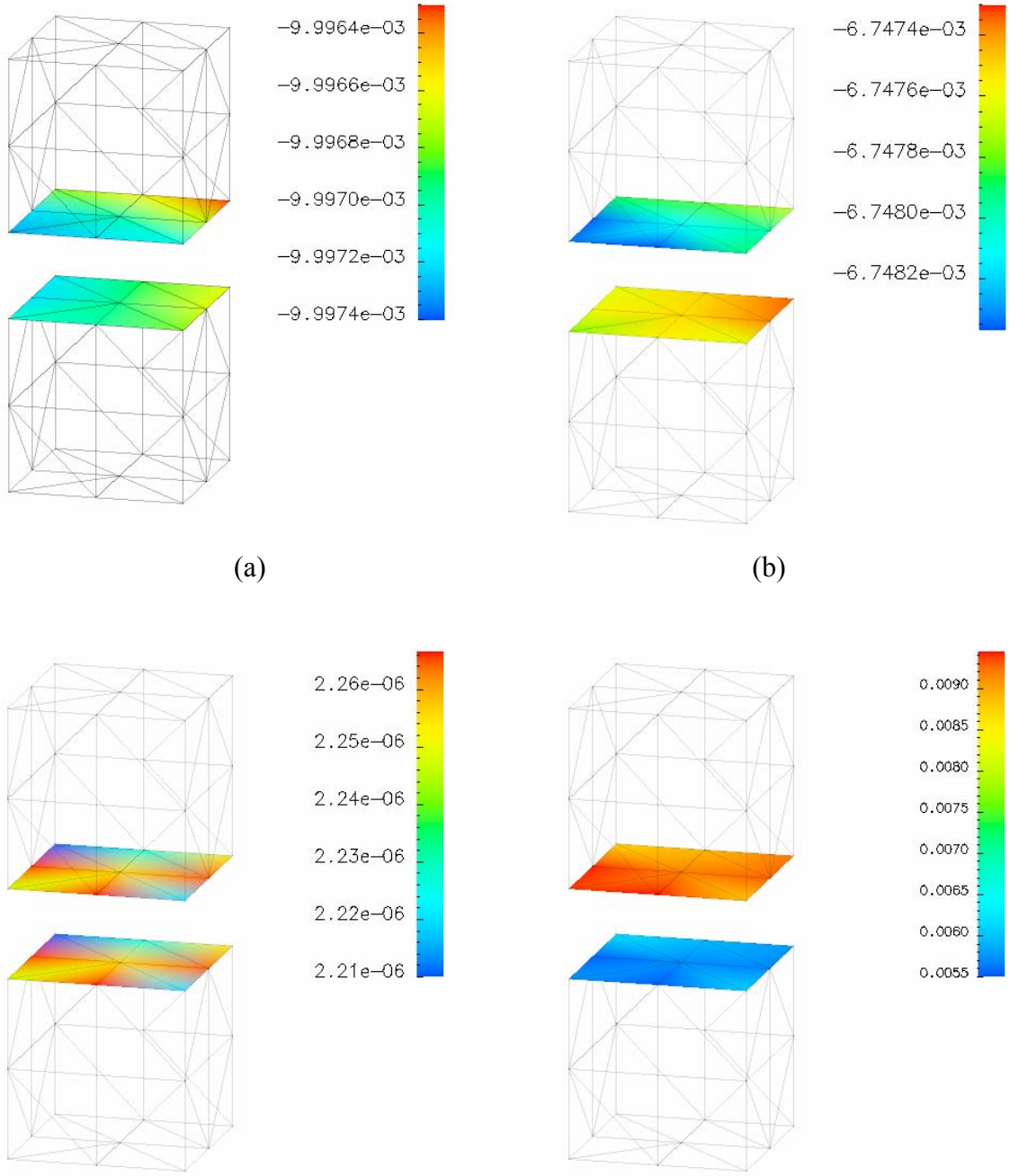

Figure 4. 7 (a) u_z, (b) σ_{zz}^E, (c) p and (d) $-\kappa p_{,z} n_z$ on the contact surfaces using continuous interpolations for Lagrange multipliers with MESH C (units are mm for displacement, MPa for normal stress and pressure, mm/sec for relative fluid velocity).

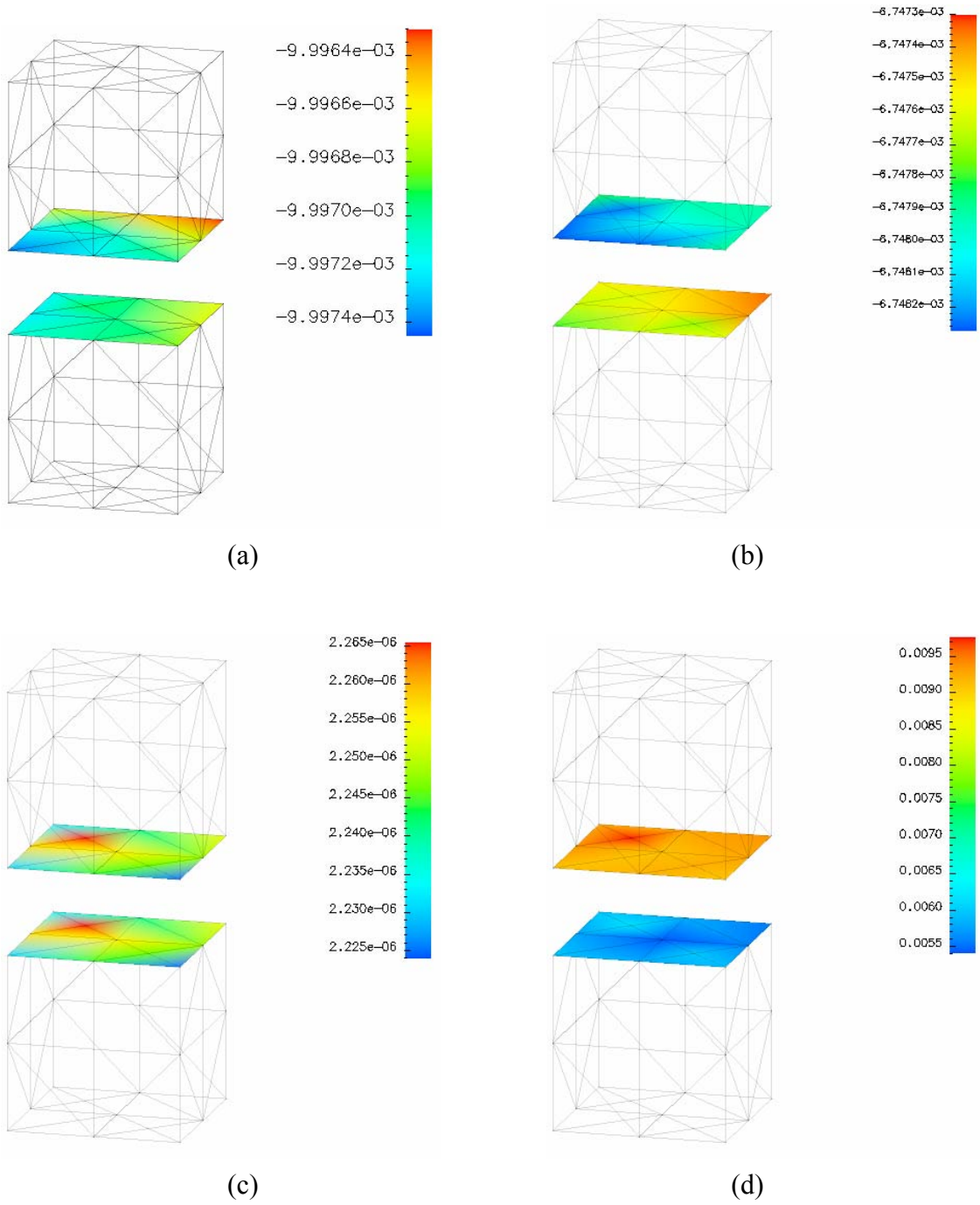

Figure 4. 8 (a) u_z, (b) σ_{zz}^{E}, (c) p and (d) $-\kappa p_{,z} n_z$ on the contact surfaces using continuous interpolations for Lagrange multipliers with MESH D (units are mm for displacement, MPa for normal stress and pressure, mm/sec for relative fluid velocity).

4.3.2 Discontinuous Interpolating Functions

A set of discontinuous interpolating functions have also been used for the Lagrange multipliers; linear for λ^s and constant for λ^f. This choice satisfies condition (i) for all test meshes, but the conditions (ii) and (iii) need to be more closely examined. Figure 4.9 shows the parameters for the singularity check (condition (iii)) using these discontinuous interpolations. MESH A, B and C satisfy condition (iii), but there are more multiplier DOF than equations for MESH D, and thus condition (iii) is not satisfied.

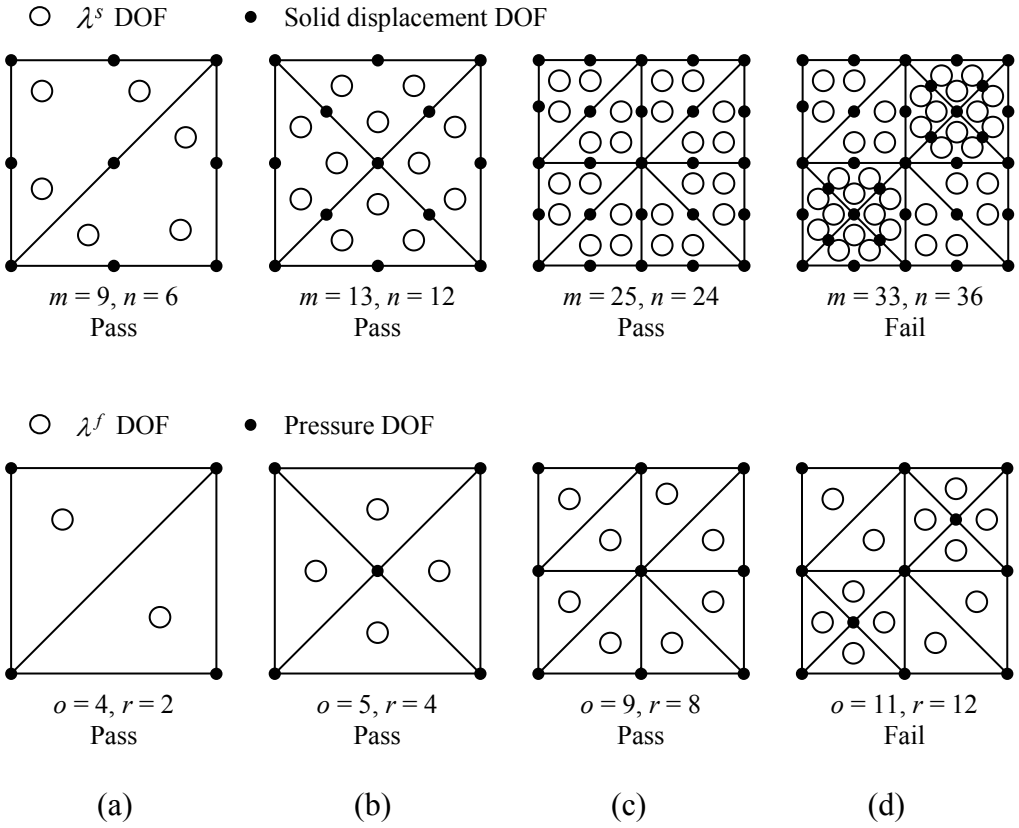

Figure 4. 9 Singularity check for the discontinuous interpolations for λ^f and λ^s (a solid circle represents a DOF of a primary variable, and a hollow circle represents a DOF of Lagrange multiplier variables) (a) MESH A, (b) MESH B, (c) MESH C and (d) MESH D.

	Condition (i) Enough Approximating Power		**Condition (ii) Enough Constraining Equations**		**Condition (iii) Non-singularity**	
	$\frac{\lambda^s}{\sigma_{ij}^E n_i n_j} \geq 1$	$\frac{\lambda^f}{\kappa p_{,i} n_i} \geq 1$	$\frac{N_{d_eqn}}{N_{d_con}} \geq 1$	$\frac{N_{p_eqn}}{N_{p_con}} \geq 1$	$\frac{m}{n} \geq 1$	$\frac{o}{r} \geq 1$
	$\frac{\lambda^s}{\sigma_{ij}^E n_i n_j} \geq 1$	$\frac{\lambda^f}{\kappa p_{,i} n_i} \geq 1$	$\frac{s^s \text{ or } \lambda^s}{u_z} \geq 1$	$\frac{s^f \text{ or } \lambda^f}{p} \geq 1$	$\frac{u_z}{\lambda^s} \geq 1$	$\frac{p}{\lambda^f} \geq 1$
MESH A	$\frac{6}{6}$	$\frac{2}{2}$	$\frac{6}{9}$ *	$\frac{2}{4}$ *	$\frac{9}{6}$	$\frac{4}{2}$
MESH B	$\frac{12}{12}$	$\frac{4}{4}$	$\frac{12}{13}$ *	$\frac{4}{5}$ *	$\frac{13}{12}$	$\frac{5}{4}$
MESH C	$\frac{24}{24}$	$\frac{8}{8}$	$\frac{24}{25}$ *	$\frac{8}{9}$ *	$\frac{25}{24}$	$\frac{9}{8}$
MESH D	$\frac{36}{36}$	$\frac{12}{12}$	$\frac{36}{33}$	$\frac{12}{11}$	$\frac{33}{36}$ *	$\frac{11}{12}$ *

*Table 4. 4 Conditions (i), (ii) and (iii) for discontinuous interpolations for Lagrange multipliers (asterisk * indicates violation of the condition).*

Table 4.4 summarizes conditions (i), (ii) and (iii) for discontinuous interpolations, and Figs 4.10 – 4.13 shows the results of the biphasic contact patch test for each of the meshes. Due to the competing nature of conditions (ii) and (iii), there are fewer constraining equations than variables for condition (ii) with MESH A, B and C. This could cause weak satisfaction of the continuity conditions related to the primary variables (position and pressure). It is clearly seen that pressure continuity in Figs 4.10 – 4.12 is weakly satisfied with discontinuity functions, when compared with pressure continuity in Figs 4.5 – 4.7 for the continuous functions. As the mesh is further refined, MESH D violates condition (iii), causing singularity for the Lagrange multipliers. However, the

constant normal traction is precisely transmitted and all four continuity conditions are closely enforced, as shown in Fig. 4.13.

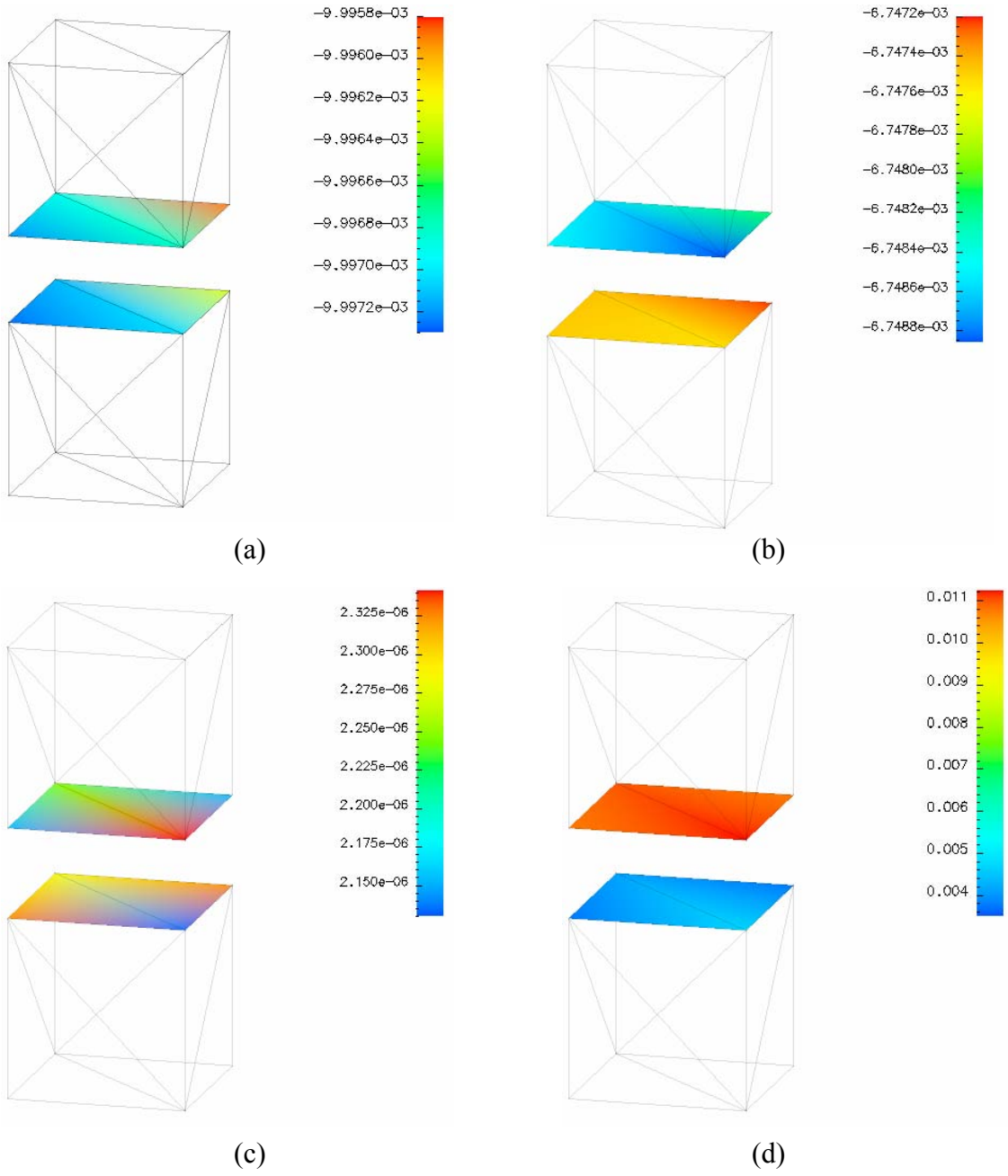

Figure 4. 10 (a) u_z, (b) σ_{zz}^E, (c) p and (d) $-\kappa p_{,z} n_z$ on the contact surfaces using discontinuous interpolations for Lagrange multipliers with MESH A (units are mm for displacement, MPa for normal stress and pressure, mm/sec for relative fluid velocity).

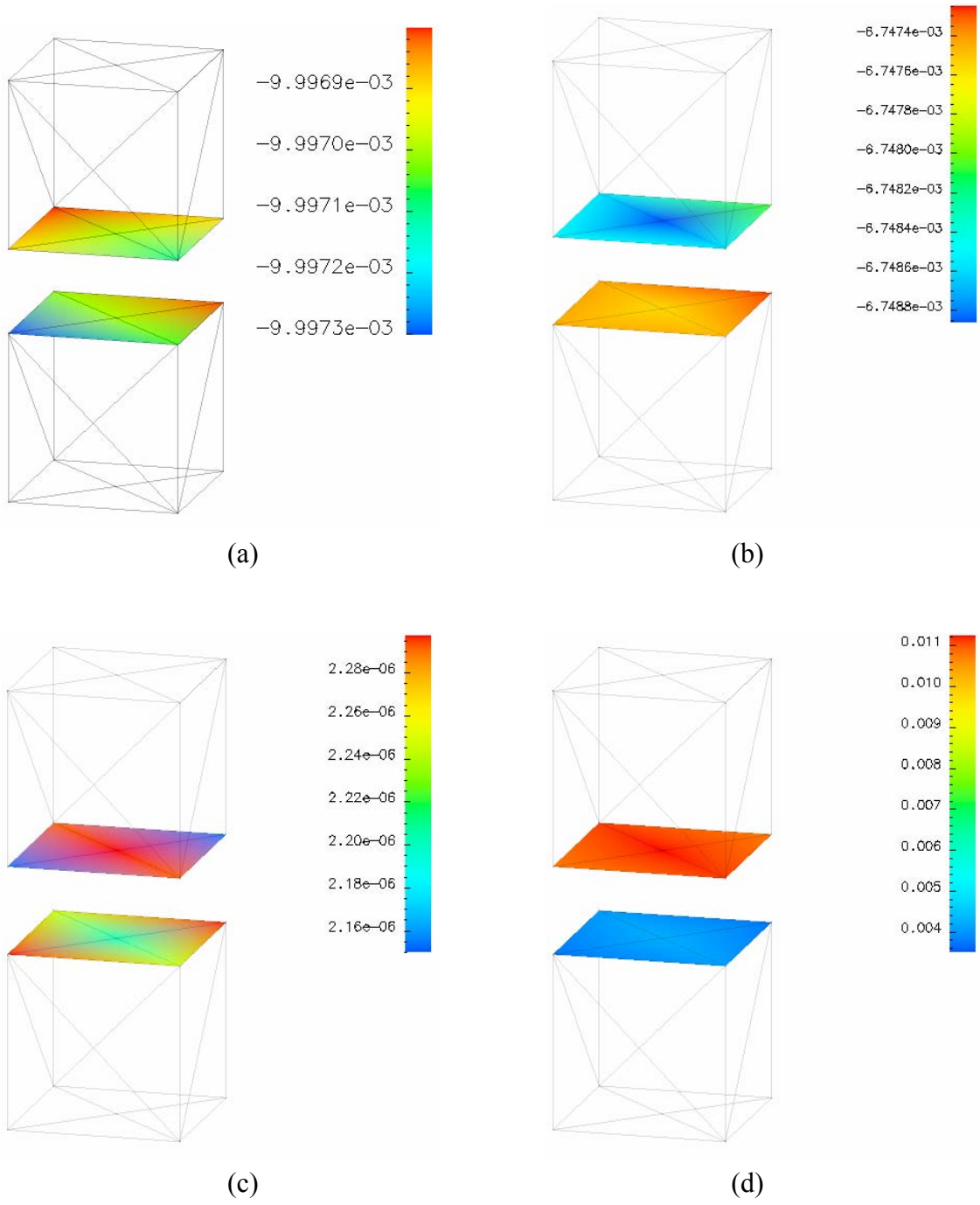

Figure 4. 11 (a) u_z, (b) σ_{zz}^E, (c) p and (d) $-\kappa p_{,z} n_z$ on the contact surfaces using discontinuous interpolations for Lagrange multipliers with MESH B (units are mm for displacement, MPa for normal stress and pressure, mm/sec for relative fluid velocity).

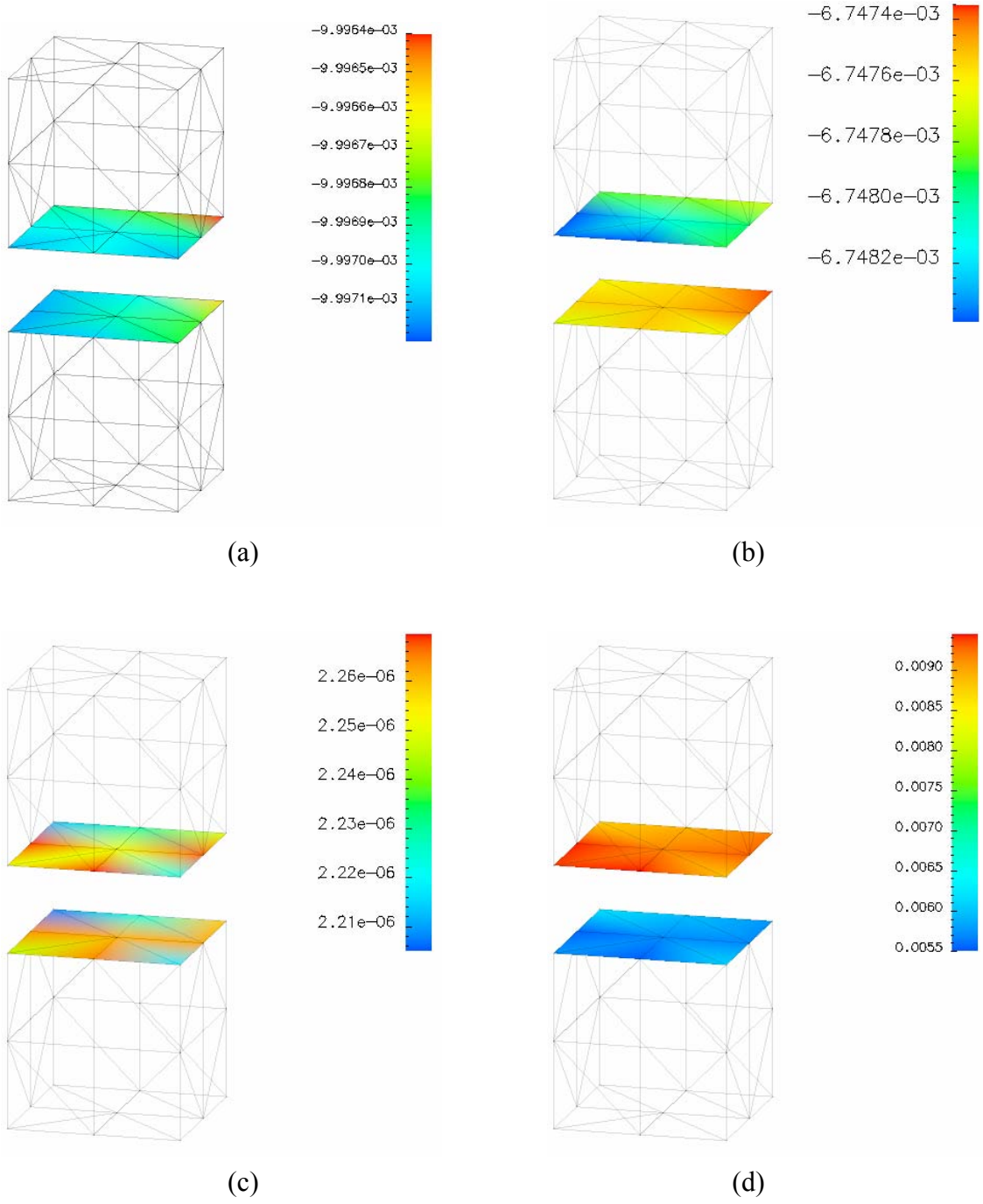

Figure 4. 12 (a) u_z, (b) σ_{zz}^E, (c) p and (d) $-\kappa p_{,z} n_z$ on the contact surfaces using discontinuous interpolations for Lagrange multipliers with MESH C (units are mm for displacement, MPa for normal stress and pressure, mm/sec for relative fluid velocity).

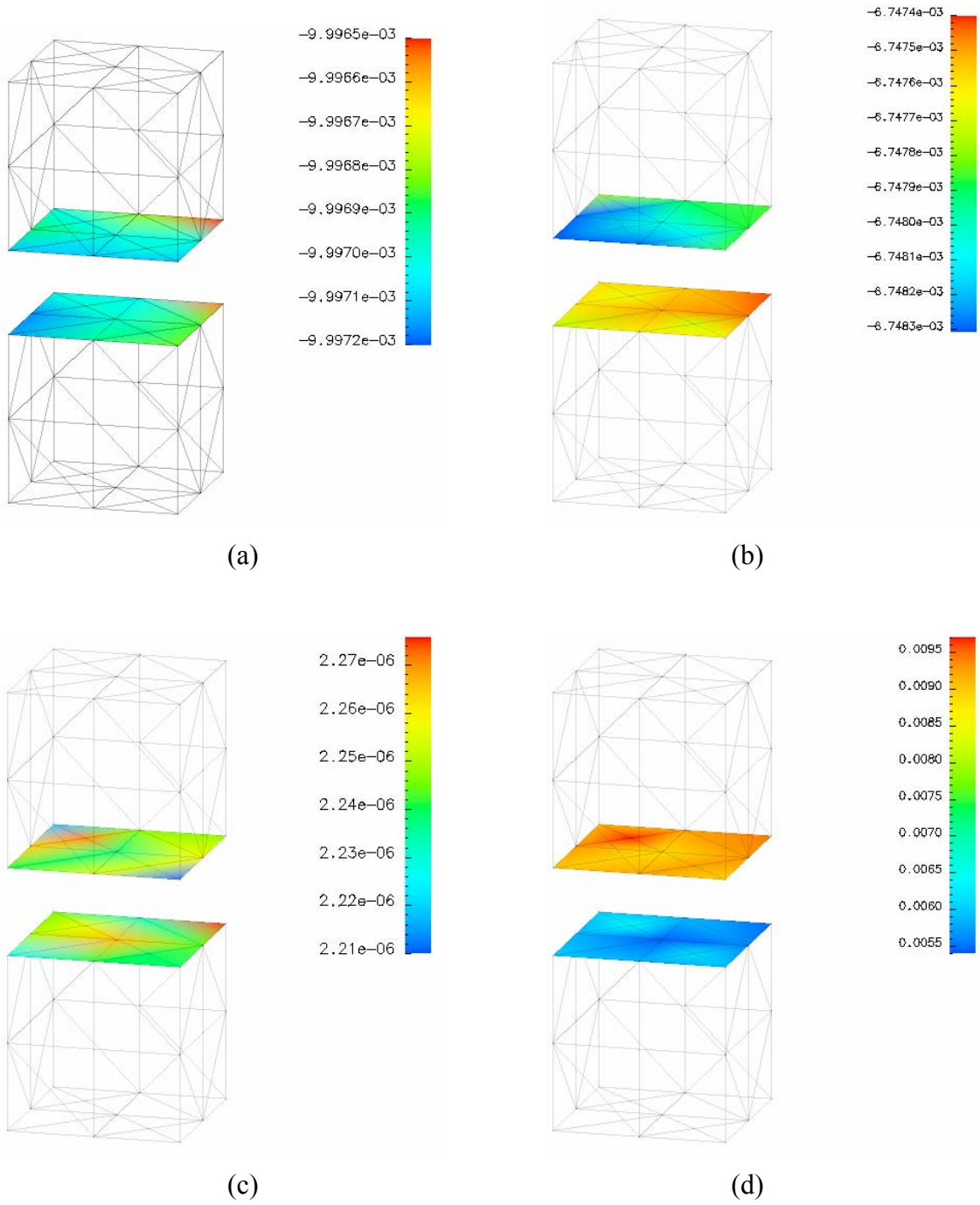

Figure 4. 13 (a) u_z, (b) σ_{zz}^E, (c) p and (d) $-\kappa p_{,z} n_z$ on the contact surfaces using discontinuous interpolations for Lagrange multipliers with MESH D (units are mm for displacement, MPa for normal stress and pressure, mm/sec for relative fluid velocity).

4.4 Biphasic Patch Test for the Alternative Kinematic Variable Based Formulation

For the 'kinematic variable based' formulation, the biphasic contact patch test ratios are summarized in Tables 4.5 and 4.6 for continuous and discontinuous interpolations, respectively. Since the definition of λ^s relates to normal solid traction, and thus remains unchanged, changes are found only in the right columns of each condition, which is related to pressure (introduced via λ^f) or relative fluid velocity (introduced directly). $N_{v^f_con}$ and $N_{v^f_eqn}$ are the number of the relative normal fluid velocity constraint variables and the number of corresponding constraining equations, respectively, on the contact surface. Also, o is the number of DOF in the pressure gradient and r is the number of DOF in λ^f. By comparing the ratios between the two formulations, it is concluded that the alternative kinematic variable based formulation, while a valid option, does not have any notable advantage over the primary variable based formulation. The primary variable based formulation is therefore used for all subsequent tests.

	Condition (i) Enough Approximating Power		**Condition (ii) Enough Constraining Equations**		**Condition (iii) Non-singularity**	
	$\frac{\lambda^s}{\sigma_{ij}^E n_i n_j} \geq 1$	$\frac{\lambda^f}{p} \geq 1$	$\frac{N_{d_eqn}}{N_{d_con}} \geq 1$	$\frac{N_{v^f_eqn}}{N_{v^f_con}} \geq 1$	$\frac{m}{n} \geq 1$	$\frac{o}{r} \geq 1$
	$\frac{\lambda^s}{\sigma_{ij}^E n_i n_j} \geq 1$	$\frac{\lambda^f}{p} \geq 1$	$\frac{s^s \text{ or } \lambda^s}{u_z} \geq 1$	$\frac{\lambda^f}{\kappa p_{,i} n_i} \geq 1$	$\frac{u_z}{\lambda^s} \geq 1$	$\frac{\kappa p_{,i} n_i}{\lambda^f} \geq 1$
MES H A	$\frac{9}{6}$	$\frac{4}{4}$	$\frac{9}{9}$	$\frac{4}{2}$	$\frac{9}{9}$	$\frac{2}{4}$ *
MES H B	$\frac{13}{12}$	$\frac{5}{5}$	$\frac{13}{13}$	$\frac{5}{4}$	$\frac{13}{13}$	$\frac{4}{5}$ *
MES H C	$\frac{25}{24}$	$\frac{9}{9}$	$\frac{25}{25}$	$\frac{9}{8}$	$\frac{25}{25}$	$\frac{8}{9}$ *
MES H D	$\frac{33}{36}$ *	$\frac{11}{11}$	$\frac{33}{33}$	$\frac{11}{12}$ *	$\frac{33}{33}$	$\frac{12}{11}$

*Table 4. 5 Conditions (i), (ii) and (iii) for continuous interpolations for Lagrange multipliers with the 'kinematic variable based' formulation (asterisk * indicates violation of the condition).*

	Condition (i) Enough Approximating Power		**Condition (ii) Enough Constraining Equations**		**Condition (iii) Non-singularity**	
	$\frac{\lambda^s}{\sigma_{ij}^E n_i n_j} \geq 1$	$\frac{\lambda^f}{p} \geq 1$	$\frac{N_{d_eqn}}{N_{d_con}} \geq 1$	$\frac{N_{v^f_eqn}}{N_{v^f_con}} \geq 1$	$\frac{m}{n} \geq 1$	$\frac{o}{p} \geq 1$
	$\frac{\lambda^s}{\sigma_{ij}^E n_i n_j} \geq 1$	$\frac{\lambda^f}{p} \geq 1$	$\frac{s^s \text{ or } \lambda^s}{u_z} \geq 1$	$\frac{\lambda^f}{\kappa p_{,i} n_i} \geq 1$	$\frac{u_z}{\lambda^s} \geq 1$	$\frac{\kappa p_{,i} n_i}{\lambda^f} \geq 1$
MESH A	$\frac{6}{6}$	$\frac{2}{4}$ *	$\frac{6}{9}$ *	$\frac{2}{2}$	$\frac{9}{6}$	$\frac{2}{2}$
MESH B	$\frac{12}{12}$	$\frac{4}{5}$ *	$\frac{12}{13}$ *	$\frac{4}{4}$	$\frac{13}{12}$	$\frac{4}{4}$
MESH C	$\frac{24}{24}$	$\frac{8}{9}$ *	$\frac{24}{25}$ *	$\frac{8}{8}$	$\frac{25}{24}$	$\frac{8}{8}$
MESH D	$\frac{36}{36}$	$\frac{12}{11}$	$\frac{36}{33}$	$\frac{12}{12}$	$\frac{33}{36}$ *	$\frac{12}{12}$

*Table 4. 6 Conditions (i), (ii) and (iii) for discontinuous interpolations for Lagrange multipliers with the 'kinematic variable based' formulation (asterisk * indicates violation of the condition).*

4.5 Contact Element Matrix Calculations for Non-matching Meshes

The results for node-to-node aligned meshes showed the capability of the formulation to reproduce constant traction, and the accuracy with which the contact continuity conditions were satisfied. In this section, the same biphasic contact patch test is performed for the meshes that are not node-to-node aligned between the two contacting surfaces.

El-Abbasi and Bathe [22] reported that patch test performance is dominated by the accuracy of evaluation of the contact integrals, while stability is related to the contact stress interpolations. To appreciate the impact of the exact evaluation of contact integrals for a non-matching mesh, a simple 2D contact example is examined. Figure 4.14 illustrates a 2D contact problem with a non-matching mesh: in (a) body II is chosen as a contactor, in (b) body I is the contactor. Recall that the contact surface is discretized to match the mesh on the contactor surface.

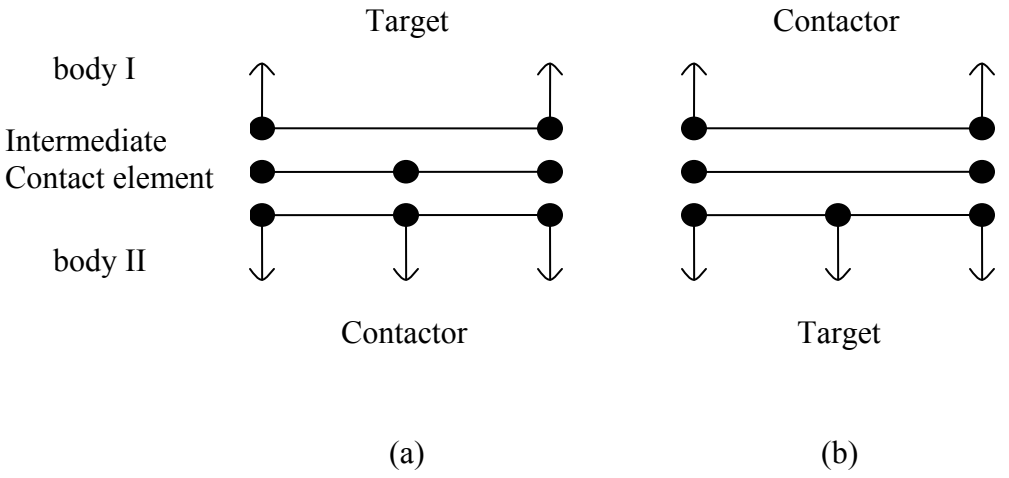

Figure 4. 14 A simple 2D contact example with non-matching mesh: (a) body II as a contactor, (b) body I as a contactor.

The element contact matrices in the current (primary variable based) formulation are repeated as Eqs. (4.13) and (4.14),

$$\boldsymbol{q}_e^{s\gamma} = \int_{\Gamma_{C_e}} \mathbf{N}^{\gamma T} \boldsymbol{n}^{\gamma} \mathbf{M}^{s} \mathrm{d}\Gamma \,, \quad \gamma = A, B \,, \tag{4.13}$$

$$\boldsymbol{q}_e^{f\gamma} = \int_{\Gamma_{C_e}} \mathbf{N}_p^{\gamma T} \mathbf{M}^{f} \mathrm{d}\Gamma \,, \quad \gamma = A, B \,. \tag{4.14}$$

Superscripts A and B indicate the contactor and a target, respectively. For the node-to-node aligned meshes, the contact integral boundary, Γ_{C_e}, is the same for both contactor and target sides, but it needs to be distinguished as $\Gamma_{C_e}^A$ for the contactor side and $\Gamma_{C_e}^B$ for the target side contact boundary with non-matching meshes. For the current formulation, Γ_{C_e} is always identical to $\Gamma_{C_e}^A$. The element interpolating functions, $\mathbf{N}^{\gamma}$, $\mathbf{N}_p^{\gamma}$, $\mathbf{M}^{s}$ and $\mathbf{M}^{f}$ are used for interpolating solid displacement/velocity, pressure, Lagrange multipliers, and the corresponding weighting functions, respectively. In the *v-p* formulation, $\mathbf{N}^{\gamma}$ is a continuous quadratic function and $\mathbf{N}_p^{\gamma}$ is a continuous linear function. And, $\mathbf{M}^{s}$ and $\mathbf{M}^{f}$ can be chosen as either continuous quadratic and continuous linear functions, respectively, or discontinuous linear and discontinuous constant functions, respectively.

With body II as the contactor (Fig 4.14 (a)), the functions $\mathbf{N}^{A}$ and $\mathbf{N}_p^{A}$ are defined on $\Gamma_{C_e}^A$ and the functions $\mathbf{M}^{s}$ and $\mathbf{M}^{f}$ are defined on Γ_{C_e}. Since the contact integral boundary Γ_{C_e} is identical to $\Gamma_{C_e}^A$, the element contact matrices, $\boldsymbol{q}_e^{sA}$ and $\boldsymbol{q}_e^{fA}$, will be exactly evaluated. For the calculation of $\boldsymbol{q}_e^{sB}$ and $\boldsymbol{q}_e^{fB}$, $\mathbf{M}^{s}$ and $\mathbf{M}^{f}$ are defined on Γ_{C_e},

but $\mathbf{N}^B$ and $\mathbf{N}_p^B$ are defined on $\Gamma_{C_e}^B$. Although the interpolating functions, $\mathbf{M}^s$ and $\mathbf{N}^B$ are defined on different boundaries, the product of the two functions remains well defined as a fourth order function (a third order function with discontinuous linear λ^s) on $\Gamma_{C_e}^B$. Since the contact integrals are numerically evaluated point-wise, $\boldsymbol{q}_e^{sB}$ can be exactly calculated. Note that the 7 Gauss quadrature point rule with 4th order precision is used in the current 3D analysis. For $\boldsymbol{q}_e^{fB}$, similarly, a product of $\mathbf{M}^f$ and $\mathbf{N}_p^B$ is defined as a second order function (a first order with discontinuous constant λ^f) on $\Gamma_{C_e}^B$, and can be exactly integrated numerically.

With body I as the contactor (Fig 4.14 (b)), the contact integrals for the contactor side, $\boldsymbol{q}_e^{sA}$ and $\boldsymbol{q}_e^{fA}$, are exactly calculated on $\Gamma_{C_e}^A$. However, the evaluation of the target side integral is not straightforward. The product of $\mathbf{M}^s$ and $\mathbf{N}^B$ becomes a combination of a fourth order function on a half of integral domain Γ_{C_e} and another fourth order function on the other half. Similarly, the product of $\mathbf{M}^f$ and $\mathbf{N}_p^B$ will be a combination of "two" second order functions over the integral domain. Therefore, the contact integrals for the target side, $\boldsymbol{q}_e^{sB}$ and $\boldsymbol{q}_e^{fB}$, will not be exactly evaluated with the classical numerical integration rules when the coarse mesh is chosen as a contactor.

The above statement can be verified through a simple test using the current 3D biphasic contact code. The geometry, boundary conditions and material properties are identical to those used in the biphasic contact patch test shown in Fig. 4.1 (b). Figure 4.15 shows non-matching meshes on the two contacting surfaces. In case (a), the contact surface on body II is refined from the mesh on body I. There are two elements on body I

and four elements on body II. In case (b), the contact surfaces are more randomly discretized. There are 32 elements on body I and 30 elements on body II. For each mesh, four tests have been analyzed, changing the choice of contactor and target surfaces, and changing the choice of Lagrange multiplier interpolations (continuous versus discontinuous). Table 4.7 summarizes the test cases.

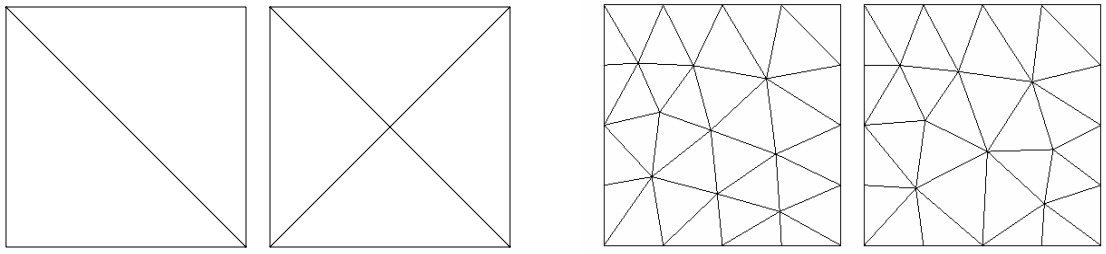

Figure 4. 15 Non-matching meshes between two contacting surfaces: (a) 2 elements on body I and 4 elements on body II, (b) 32 elements on body I and 30 elements on body II.

	Mesh	Contactor	Interpolations for λ^s and λ^f
Case 1	Figure 4.15 (a)	body II	Continuous
Case 2		body II	Discontinuous
Case 3		body I	Continuous
Case 4		body I	Discontinuous
Case 5	Figure 4.15 (b)	body II	Continuous
Case 6		body II	Discontinuous
Case 7		body I	Continuous
Case 8		body I	Discontinuous

Table 4. 7 Test cases of the biphasic contact patch tests for non-matching meshes.

For Cases 1 and 2, it is expected that all element contact matrices, $\boldsymbol{q}_e^{sA}$, $\boldsymbol{q}_e^{sB}$, $\boldsymbol{q}_e^{fA}$ and $\boldsymbol{q}_e^{fB}$, are exactly evaluated, since the contactor side mesh is a exact refinement of target side mesh. Figure 4.16 (a) and (b) show that the constant strain, $\varepsilon_{zz} = 0.01$, has been accurately transmitted between the contacting surfaces (there are noticeable differences in color, but the magnitude of the difference is insignificant). No significant difference is observed in the use of continuous versus discontinuous Lagrange multipliers.

However, with the coarse mesh as a contactor, Cases 3 and 4, the target side integrals for $\boldsymbol{q}_e^{sB}$ and $\boldsymbol{q}_e^{fB}$ will not be accurately evaluated. This causes significant variations of normal strain on the target surface, although the distribution is fairly uniform on the contactor surface (see Figs 4.16 (c) and (d)). Both continuous and discontinuous multipliers yield similar results, and the error is beyond an acceptable range.

Figure 4.17 shows the normal strain distributions for Cases 5 through 8 (the refined pair of contact surface meshes). A more uniform strain distribution is observed with the choice of the more refined surface as a contactor (Cases 7, 8 compared with Cases 5, 6) and with discontinuous Lagrange multipliers (Cases 6, 8 compared with Cases 5, 7). When the coarse mesh is chosen as a contactor in Cases 5 and 6, the results show large variation, particularly on the target surface.

Enforcement of the four continuity conditions is examined for Cases 5 through 8. Case 8 results in the closest enforcement among the cases and is shown in Figure 4.18. A slightly large displacement u_z is found on body I due to the initial gap of 0.0001 mm (Fig.

4.18 (a)). However, the uniformity in continuity condition observed with the matching mesh is not obtained for the non-matching meshes. In Fig. 4.18 (b), the applied compressive traction of 0.00675 MPa is reproduced in most of the contact area with a maximum error of 4.3 %. Pressure is kept continuous along the contact surfaces, and the non-uniformity over the contact area is negligible (Fig. 4.18 (c)). The discontinuity of relative fluid velocity in Fig. 4.18 (d) can be explained by the same reasons presented for the node-to-node cases. In fact, compared with the matching mesh results, this discrepancy is reduced as more elements are used through the thickness (compare Figs. 4.5 - 4.8 with 4.10 – 4.13 (d)). Overall, the continuity conditions are enforced within an acceptable error range most consistently with the choice of the finer mesh as the contactor, and with the discontinuous functions.

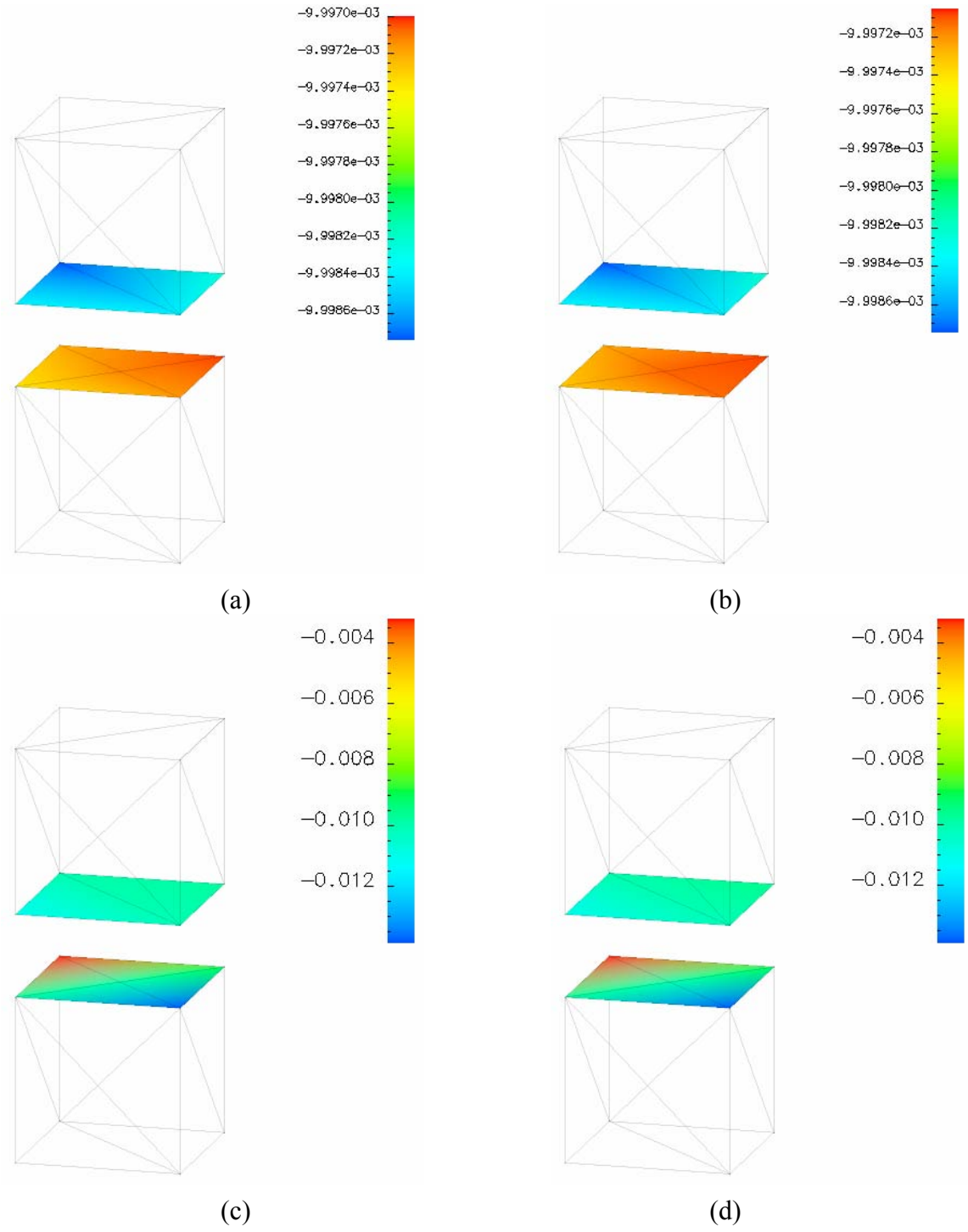

Figure 4. 16 Distributions of strain, ε_{zz}, on the contacting surfaces for (a) Case 1, (b) Case 2, (c) Case 3 and (d) Case 4.

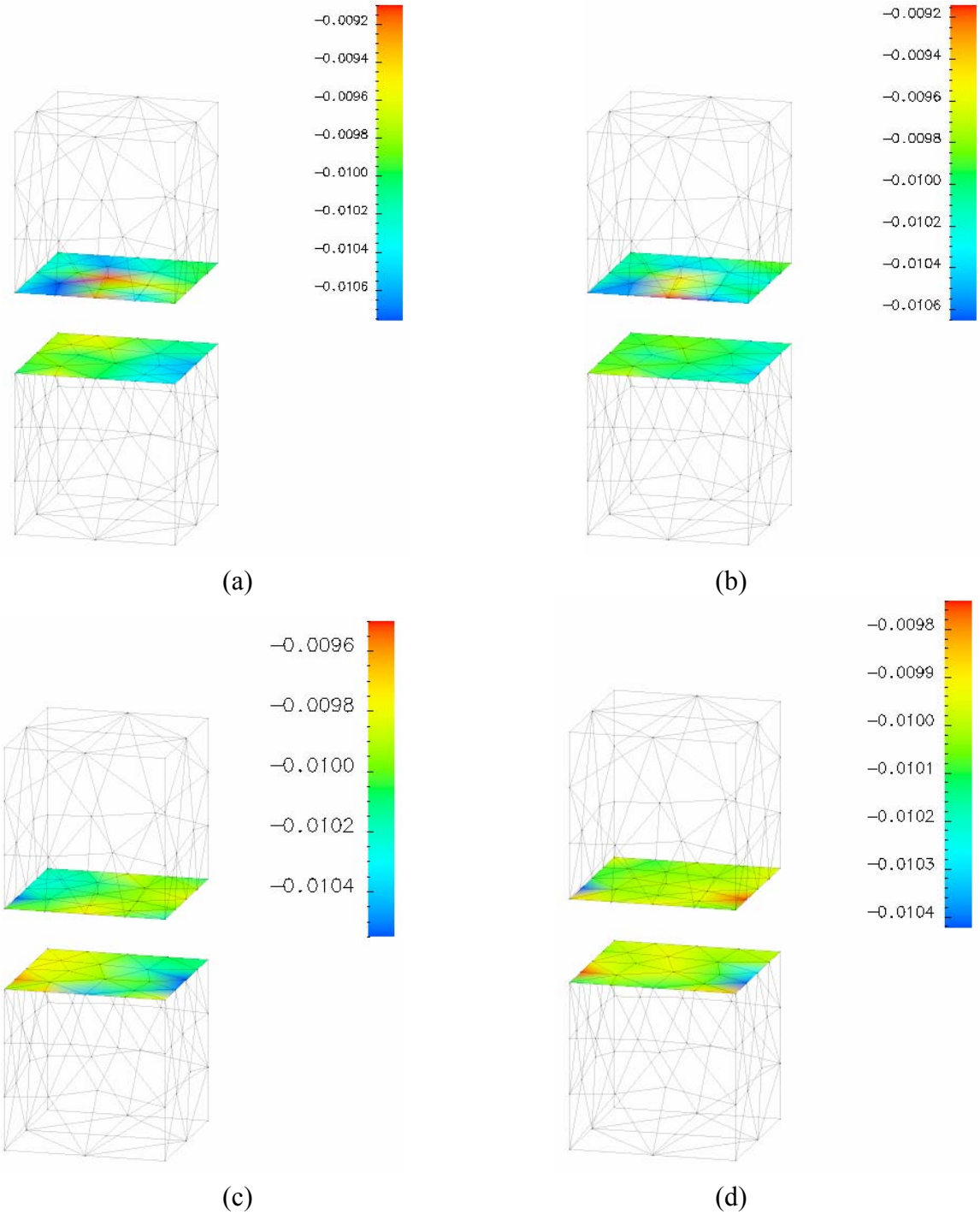

Figure 4. 17 Distributions of strain, ε_{zz}, on the contacting surfaces for (a) Case 5, (b) Case 6, (c) Case 7 and (d) Case 8.

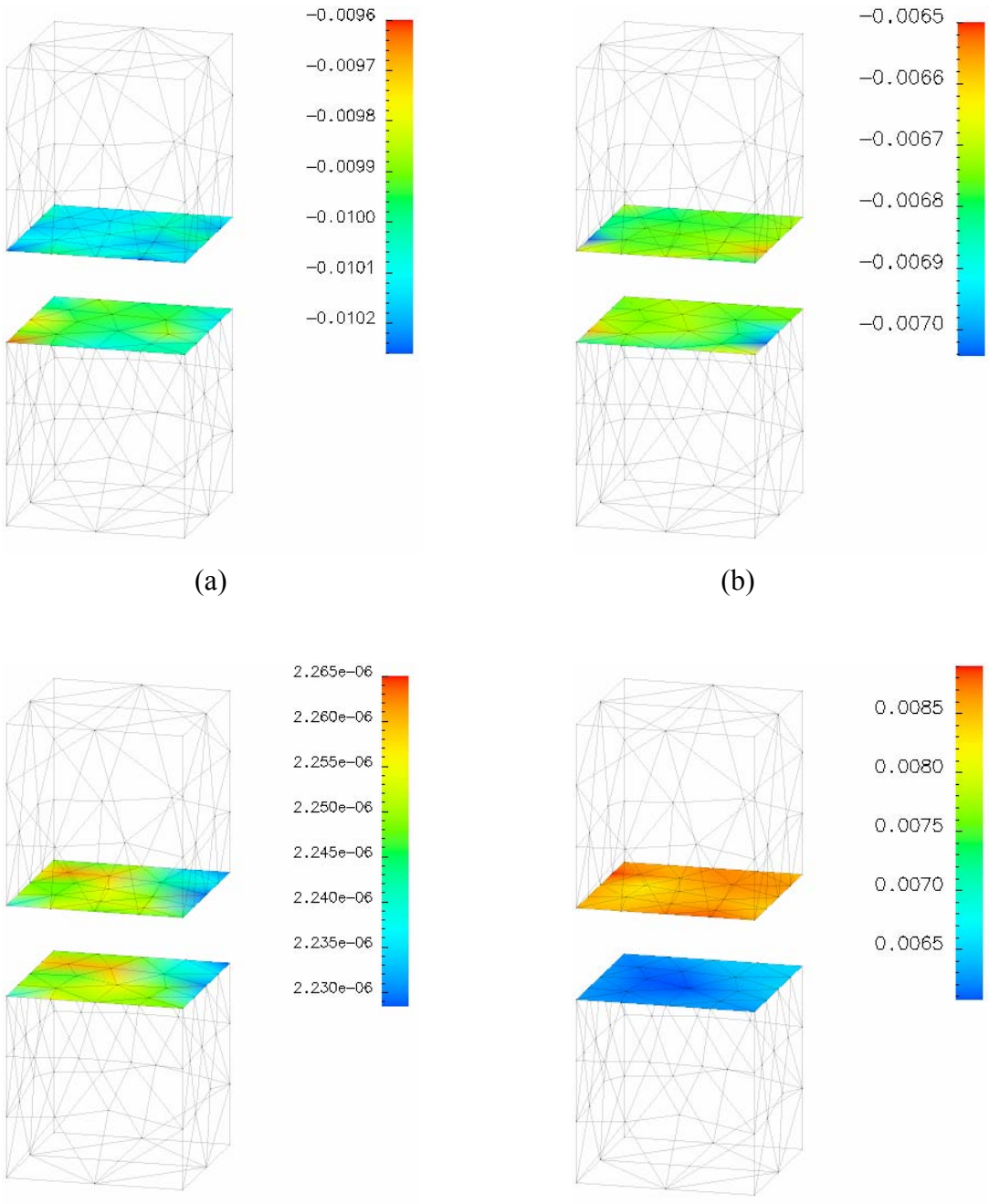

Figure 4. 18 (a) u_z, (b) σ_{zz}^E, (c) p and (d) $-\kappa p_{,z} n_z$ on the contact surfaces for Case 8 (units are mm for displacement, MPa for normal stress and pressure, mm/sec for relative fluid velocity).

From these tests, it can be concluded that when the meshes are not node-to-node aligned (the usual situation in contact problems): (a) the target side integrals for $\boldsymbol{q}_e^{sB}$ and $\boldsymbol{q}_e^{fB}$ are not accurately evaluated; (b) this inaccurate calculation is the source of error for the biphasic contact patch test; (c) if practical, the finer mesh should be chosen as the contactor side;. and (d) the contact continuity conditions are closely satisfied with the choice of the finer mesh as the contactor, and with the discontinuous functions.

To improve the accuracy of the numerical integrals for contact matrices, El-Abbasi and Bathe [22] suggested "the composite integration rule" for their 2D elastic contact problems. This technique defines unbiased intermediate contact elements essentially using the intersection of the contactor and target meshes, and then uses Gaussian or Newton-Cotes rules to numerically integrate the contact matrices. However, the method is not readily available for 3D contact problems due to geometric complexity. Care must be taken to eliminate ill-shaped contact elements, such as slivers, that can result when nodes from one side are near nodes on the other side, but do not align to within a tolerance. Also, the approach could cause stability problems in our formulation, since the method generates too many unknowns for the Lagrange multipliers for highly non-matching 3D contact meshes. In future research, algorithms need to be developed to address this issue and ensure the convergence of the biphasic finite element contact formulation.

Chapter 5: Evaluation of Iterative Solution Methods for Linear Biphasic Problems

5.1 Introduction

Historically, our laboratory has used direct methods for the solution of both linear and nonlinear biphasic problems. Recognizing the computational demands on both storage and CPU time would accompany 3D biphasic contact analysis. It was apparent that more efficient solution methods would be needed. Thus, a study was undertaken (before initiating the development of 3D contact) to evaluate iterative methods for 3D linear biphasic problems. Our rationale was to identify best methods first for biphasic problems, from which a subset could be selected for use in 3D biphasic contact problems.

The need to solve large sparse linear systems arises in most scientific applications as the size of problems increase for 3D analysis on complex geometries. Until recently, direct solution schemes based on Gaussian elimination methods were popular because of their robustness. However, both computing costs and memory requirements for direct solvers easily grow beyond the hardware capability and become prohibitive for large problems. As an alternative, iterative solution techniques emerged in the sixties and have been continuously improved to take advantage of the sparseness of the system on high performance computers.

5.2 Iterative Methods

Iterative techniques use successive approximations to obtain more accurate solutions to a linear system. Stationary methods such as the Jacobi, Gauss-Seidel, Successive Overrelaxation (SOR), and the Symmetric Successive Overrelaxation (SSOR) methods are easier to understand and implement but usually are not feasible for large ill-conditioned systems in realistic application [7, 86, 91]. Preconditioned *Krylov* subspace methods are more viable choices for those cases. The algorithmic details and comparisons of modern iterative methods are available in the literature [7, 28, 70, 71]. A brief discussion is presented on the viability of some of selective methods for our problem.

5.2.1 *Krylov* Subspace Methods

The Conjugate Gradient (CG) method is one of the oldest and most effective non-stationary methods for symmetric, positive definite systems. In this method the successive approximations $\boldsymbol{x}^k \in \mathrm{R}^n$ of the exact solution $\boldsymbol{x}$ can be found with a given initial approximation $\boldsymbol{x}^o$ using,

$$\boldsymbol{x}^{k+1} = \boldsymbol{x}^k + \alpha_k \boldsymbol{d}^k, \quad k = 0, 1, \ldots, \tag{5.1}$$

where the search directions, $\boldsymbol{d}^k$, are conjugate, i.e., $\boldsymbol{d}^i \cdot \boldsymbol{A}\boldsymbol{d}^j = 0$ for $i \neq j$, and the step length α_k is chosen to be optimal with the form,

$$\alpha_k = \frac{\left(\boldsymbol{r}^k, \boldsymbol{r}^k\right)}{\left(\boldsymbol{A}\boldsymbol{d}^k, \boldsymbol{r}^k\right)}, \tag{5.2}$$

where, $\boldsymbol{r}^k = \boldsymbol{b} - \boldsymbol{A}\boldsymbol{x}^k$. The CG method constructs an orthogonal basis on the Krylov subspace to eliminate components of the error in the direction of eigenvectors associated with extreme eigenvalues [7]. Convergence rate depends on the spectral condition number, defined as a ratio of the maximum eigenvalue to the minimum eigenvalue. Accordingly, a faster convergence can be obtained by reducing the condition number with preconditioners. However, since CG is not applicable to non-symmetric or indefinite systems, and other CG modifications such as CG on Normal Equations (CGNE or CGNR) suffer from slow convergence [7], they were not tested in this study.

Saad *et al*. [69] proposed the Generalized Minimal Residual Method (GMRES) as a direct generalization of the CG method for nonsymmetric indefinite systems. GMRES minimizes the L_2 norm of the residual at the k-th iteration, $\left\|\boldsymbol{b} - \boldsymbol{A}\boldsymbol{x}^k\right\|_2$, using a sequence of orthogonal vectors. Since the full set of previously calculated orthogonal bases need to be retained in this method, the memory requirement grows linearly with k. For this reason, a restarted version is used in which previous bases are discarded after a restart number, m, of iterations, and subsequent bases are used as the initial data for the next m iterations. In this study, GMRES with a restart number of 30 was tested using modified Gram-Schmidt orthogonalization, in which orthogonality is gradually lost but the computational cost drops significantly.

The Biconjugate Gradient (BCG) algorithm was developed from a different approach in GMRES, replacing the orthogonal sequence of residuals by two mutually orthogonal sequences. The method implicitly solves not only the original system $\boldsymbol{A}\boldsymbol{x} = \boldsymbol{b}$ but also a dual linear system $\boldsymbol{A}^T\boldsymbol{x}^* = \boldsymbol{b}^*$ and constructs two sequences of residuals based on the two linear systems. In practice, however, the BCG experiences unpredictable

convergence behavior and even divergence. Remedies for these divergence situations are found in the literature [7, 65]. Sonneveld [73] derived the Conjugate Gradient Squared (CGS) method in order to avoid the use of $\boldsymbol{A}^T$ in BCG and achieve faster convergence. It is often observed that the convergence rate of CGS is twice as fast as for BCG at roughly the same cost [7, 71]. The Biconjugate Gradient Stabilized (BiCGSTAB) method is obtained by a modification of the residual vectors in CGS using "stabilizing" polynomials and shows the best convergence rate in its class.

Freund *et al* [23] introduced the Quasi-Minimal Residual (QMR) method where a basis for Krylov subspace is constructed using a biorthogonal process. The method uses a look-ahead strategy and its convergence rate is smoother than for BCG. Freund [24] also developed a transpose free variant of CGS, Transpose-Free Quasi-Minimal Residual (TFQMR) that yields the desirable convergence behavior of CGS at a lower computational cost.

In spite of a number of surveys on recent Krylov methods [7, 17, 70, 71], no single method is known to solve all classes of linear systems, and little practical information on their performance is available. Therefore, numerical experimentation is needed to provide insight into their capability for our biphasic problems. Since our system is symmetric and indefinite, choice of test methods was narrowed to GMRES, BiCGSTAB, and TFQMR methods.

5.2.2 Incomplete LU Factorization Preconditioners

A properly chosen preconditioner, $\boldsymbol{M}$, transforms the original linear system into one in which the same solution can be easily obtained with a favorable condition number:

$$\boldsymbol{M}^{-1}\boldsymbol{A}\boldsymbol{x} = \boldsymbol{M}^{-1}\boldsymbol{b}\,. \tag{5.3}$$

Based on the multiplicative position of the preconditioner, $\boldsymbol{M}$ is called the left, right, or split preconditioner which transforms into $\boldsymbol{M}^{-1}\boldsymbol{A}$, $\boldsymbol{A}\boldsymbol{M}^{-1}$, or $\boldsymbol{L}^{-1}\boldsymbol{A}\boldsymbol{U}^{-1}$, respectively. Many widely used preconditioners are based on incomplete LU (ILU) factorization. During a complete factorization, zero entries in the original matrix will typically be replaced by nonzero entries, called fill-in, in the factored matrix. ILU preconditioners are categorized into two classes based on the strategy used for allowing fill-in. One strategy to allow fill-in is based on the structure of nonzero entries of the original coefficient matrix and the other is based on the relative scale of numerical values of the entries. The former, called ILU(k), was tested in this study. Details are available in texts and references [4, 5, 7, 13, 17, 70], and an extensive experimental study on ILU preconditioners for indefinite matrices is found in Chow *et al.* [15].

5.2.3 Equation Reordering Methods

In an ILU-preconditioned Krylov subspace method, equation reordering may have a significant impact both on memory requirement and on computing time. The structure of the nonzero entries after reordering determines the amount of fill-in, the required number of floating-point operations, and the quality of the preconditioner during iterative solution. Reordering techniques based on standard graph theory can be found in [20, 67]; experimental studies and surveys on the impact of reordering have been performed by Botta *et al*. [13] and Benzi *et al* [10]. For our linear system, one-way dissection, nested dissection, reverse Cuthill-McKee, and quotient minimum degree orderings were compared with preconditioned Krylov subspace methods.

All of the iterative, preconditioning and reordering methods needed for our study are available in a software, the Portable, Extensible Toolkit for Scientific Computation (PETSc) [6]. PETSc has been used with our biphasic analysis, both implemented within the *Trellis* object oriented finite element analysis framework [8] of the Scientific Computation Research Center (SCOREC) at Rensselaer Polytechnic Institute, to perform all of the analyses.

5.3 Example Problems and Numerical Results

An experimental study has been conducted by solving the linear systems arising from our biphasic *v-p* formulation using preconditioned Krylov subspace methods, ILU(k) preconditioning, and matrix reordering. A physiological problem representing the humeral head tissue layer in the shoulder was used to compare methods (see Fig. 5.1). Tissue geometry was provided by the Orthopedic Research Laboratory at Columbia University using stereophotogrammetry (SPG) on cadaver shoulder joints. The boundary conditions for this example consist of a uniformly distributed compressive traction in the negative z direction, $\bar{\boldsymbol{t}}^{Tot} = -70$ kPa, applied to the top surface of the thin layer of cartilage. This load is approximately normal to surface at the center. The lower surface of the tissue is supported by a rigid impermeable surface (simulating bone) so there is no motion of either phase. To implement this condition for the *v-p* formulation, the solid phase degrees of freedom are constrained to zero on this surface, and the pressure degrees of freedom are unspecified. The fluid flow constraint is a natural boundary condition and is therefore satisfied approximately. The tissue has a solid phase Young's modulus and Poisson's ratio, $E^s = 0.675$ MPa and $\nu^s = 0.125$, respectively, permeability, $\kappa =$

5.0×10^{-15} m^4/N/sec, and solid content, ϕ^s = 0.2. In order to study the capability of the iterative methods with respect to the size of the system, four increasingly refined meshes were tested. Table 5.1 describes the four global coefficient matrices that arise from these meshes using the previously described ten-node tetrahedral mixed *v-p* element. All comparison discussed here are based on results for a single time step (the first step) of the time dependent problem, since the coefficient matrix remains the same for later steps.

It is important to note that the test problem (Fig. 5.1) has physiologically realistic geometry and sufficiently realistic loading. Some combinations of iterative solver and preconditioning methods performed well in preliminary tests using canonical problems, such as a cylinder or block, of similar dimension in each global coordinate direction, but were unsuccessful in physiological problems. The converse was not found to be true. Therefore, realistic geometry is an important factor in assessing the methods. The direction and distribution of loading, within reasonable limits, are not factors that influence the characteristics of the methods.

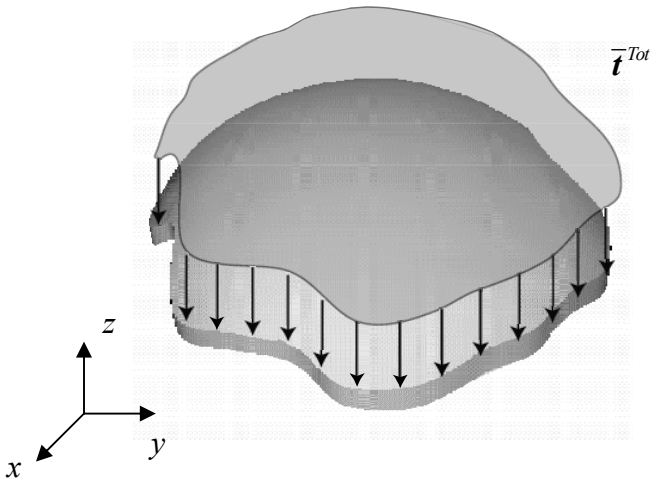

Figure 5. 1 A schematic of the test problem representing the humeral head cartilage layer in the human shoulder.

Matrix	Number of elements	Number of Equations	Nonzero Entries
MESH1	231	1,083	56,569
MESH2	2,641	11,159	607,937
MESH3	16,548	69,437	4,867,425
MESH4	53,438	221,187	17,649,257

Table 5. 1 Description of coefficient matrices from increasingly refined meshes for the biphasic finite element formulation.

The following Krylov subspace methods were tested: GMRES with a restart number of 30 using modified Gram-Schmidt orthogonalization, TFQMR, and BiCGSTAB. These methods became the natural choice for our global, linear, unstructured, and symmetric indefinite matrix system, since other CG-like methods are only applicable for symmetric positive definite matrices, or they show poor convergence characteristics. Level-based incomplete LU factorization preconditioners, ILU(k), were used as the left preconditioner. Since matrix reordering is expected to have an important impact on preconditioned Krylov subspace methods, the effect of different reordering methods was studied in terms of convergence behavior and memory requirements. One-way dissection (OWD), nested dissection (ND), reverse Cuthill-McKee (RCM), and quotient minimum degree (QMD) orderings were compared.

A zero vector was used as the initial guess for each iterative solution. Iterations ceased and the approximate solution was obtained, when the absolute size of the L_2 norm of a preconditioned residual, $\left\| (\boldsymbol{LU})^{-1} \left(\boldsymbol{b} - \boldsymbol{A}\boldsymbol{x}^k \right) \right\|_2$ became less than 10^{-6} (where, $\boldsymbol{L}$ and $\boldsymbol{U}$ are the lower and upper incomplete factors, respectively, and it is noted that the norm for

the initial guess is of order O(1)). Otherwise, iteration was terminated after 500 iterations due to slow convergence, or divergence, in which case the method was considered to fail converge.

5.3.1 Without Fill-in

The first numerical experiment used the ILU factorization preconditioner, allowing no fill-in, ILU(0). Table 5.2 shows the number of iterations required for convergence for combinations of reordering and iterative methods. Both BiCGSTAB and TFQMR required fewer iterations to converge than GMRES, although the convergence was significantly affected by the choice of reordering method. One-way dissection (OWD) required the fewest iterations with all three iterative methods, and the reverse Cuthill-McKee (RCM) gave the worst performance. Note that none of the iterative methods converged with RCM for cases MESH3 and MESH4 (the most refined meshes).

Krylov method	BiCGSTAB + ILU(0)				TFQMR + ILU(0)				GMRES + ILU(0)			
Ordering	OWD	ND	RCM	QMD	OWD	ND	RCM	QMD	OWD	ND	RCM	QMD
MESH1	6	7	11	7	6	8	12	7	11	13	16	13
MESH2	13	37	334	25	14	38	361	27	22	42	*	43
MESH3	24	37	*	94	24	37	*	79	39	56	*	113
MESH4	44	141	*	194	45	128	*	187	69	138	*	209

*Table 5. 2 Required number of iterations to solve the test matrices using incomplete LU preconditioning with no fill-in ILU(0). A * indicates that the convergence criteria was not satisfied within 500 iterations.*

Figure 5.2 shows the residual of the L_2 norm for the three Krylov methods with one-way dissection for case MESH4. The convergence behavior of GMRES was smoother but slower than BiCGSTAB and TFQMR. Figure 5.3 shows the effect of matrix reordering scheme on the convergence behavior of BiCGSTAB, and that OWD yields the most rapid convergence. The superiority of OWD was also observed with TFQMR and GMRES, but the results are not shown here. Consequently, it can be concluded that BiCGSTAB with OWD is the best combination for our linear system when an ILU(0) preconditioner is used.

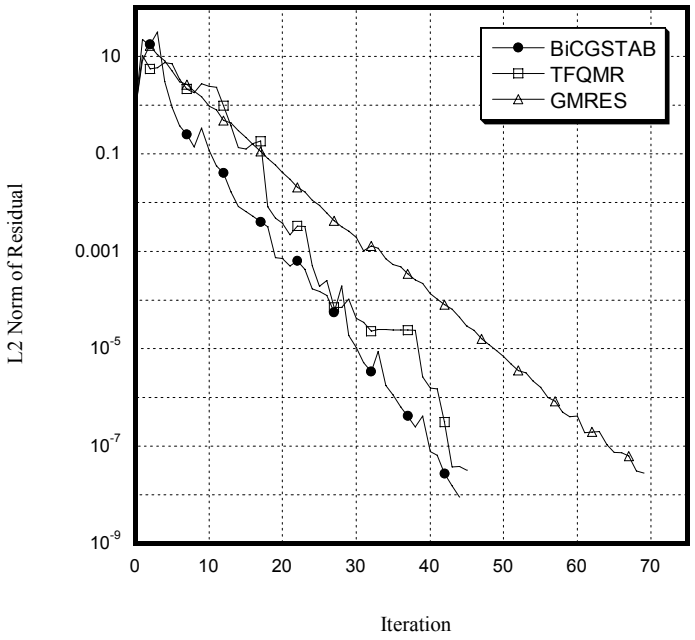

Figure 5. 2 The L_2 *norm of the residual for each Krylov subspace method using one-way dissection reordering for case MESH4.*

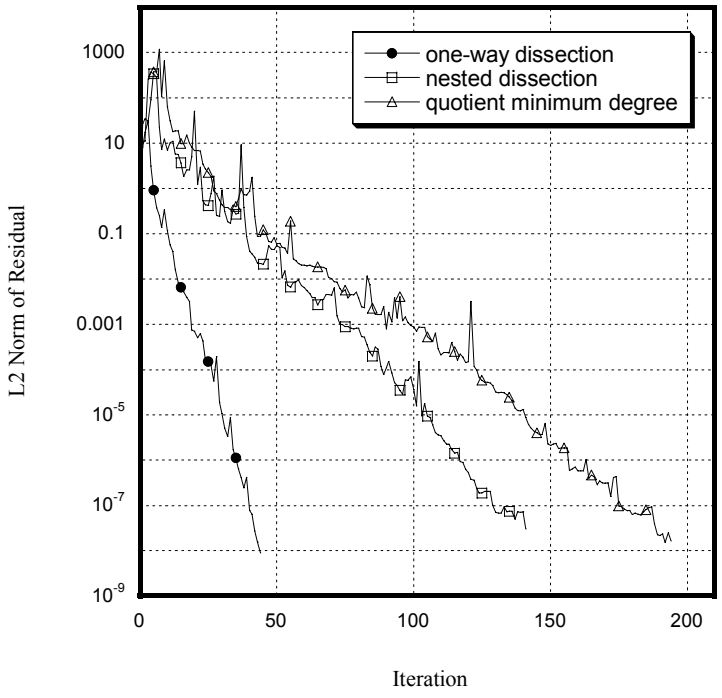

Figure 5. 3 Decrease in the L_2 *norm of the residual for the matrix reordering methods using BiCGSTAB Krylov method for case MESH4.*

The number of floating point operations (flops) is a useful comparative measure of the speed of iterative methods, since the number of flops per iteration and the number of iterations varies with each method. Table 5.3 lists the number of flops required for convergence for combinations of matrix reordering and iterative method, all using ILU(0) preconditioning (the values shown were monitored using profiling functions in PETSc). Similar to the pattern observed for number of iterations, BiCGSTAB with OWD requires the fewest flops, and reverse Cuthill-McKee requires the most among the four reordering methods, regardless of the Krylov method used. However, it is interesting to note that GMRES requires fewer flops than TFQMR for some cases (for example, with OWD, ND, and QMD for MESH3 and MESH4). This is because the Lanczos biorthogonalization process in BiCGSTAB and TFQMR requires twice as many matrix-vector multiplications as GMRES at each iteration. The advantage of GMRES was not as obvious for a small problem (MESH1). BiCGSTAB requires the fewest total flops due to its higher convergence rate. In terms of total flops, TFQMR is not much better, and is sometimes worse, than GMRES.

Krylov method	BiCGSTAB + ILU(0)				TFQMR + ILU(0)				GMRES + ILU(0)			
Ordering	OWD	ND	RCM	QMD	OWD	ND	RCM	QMD	OWD	ND	RCM	QMD
MESH1 ($\times 10^6$)	5.36	6.19	8.39	6.09	6.08	7.61	10.3	6.92	6.09	7.19	8.38	7.09
MESH2 ($\times 10^8$)	1.02	2.56	21.3	1.79	1.25	3.11	27.6	2.26	1.19	2.20	*	2.24
MESH3 ($\times 10^9$)	1.40	2.09	*	4.92	1.64	2.46	*	4.96	1.60	2.27	*	4.36
MESH4 ($\times 10^{10}$)	0.88	2.65	*	3.61	1.06	2.88	*	4.16	0.98	1.90	*	2.83

*Table 5. 3 Number of flops (the exponent for each mesh case is shown in parentheses) to solve the linear systems using an ILU(0) preconditioner. A * indicates that the convergence criteria was not satisfied within 500 iterations.*

Although the required number of iterations or flops may illustrate the convergence behavior or computing demands, it should be noted that the cost of each flop in Table 5.3 is not the same. For example, the cost of a flop depends significantly on the time to load the data from memory into the register, so the time per flop, called *flop rate*, in vector operations is different than in a sparse matrix-vector product. In fact, flop rates depend in a very complicated manner on factors such as the data layout, cache size, cache policy, and number of registers. For these reasons, simply comparing the number of iterations or number of flops produces only a rough estimate. Consequently, it is instructive to examine wall-clock time on a specific computer architecture as a measure of the actual computing performance. In order to perform a meaningful comparison on clock time, a single machine has been dedicated to the current study whose specifications are as follows; a Sun Ultra-2 workstation with two 200MHz UltraSPARC-I (only one of

the CPUs has been used for serial computing) and RAM of 2GB. Each CPU has 1MB of L2 cache and the system clock is 100MHz.

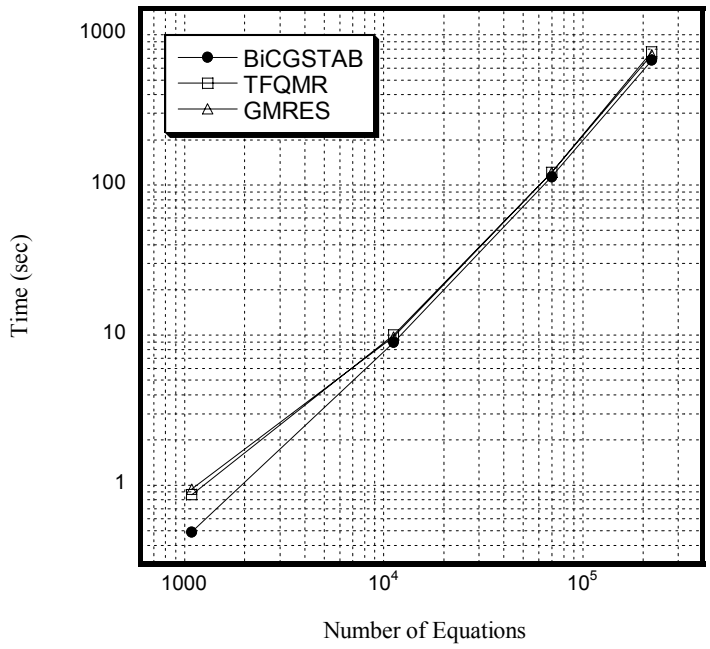

Figure 5. 4 Elapsed wall-clock time to solve the linear systems using alternate Krylov subspace methods with one-way dissection reordering.

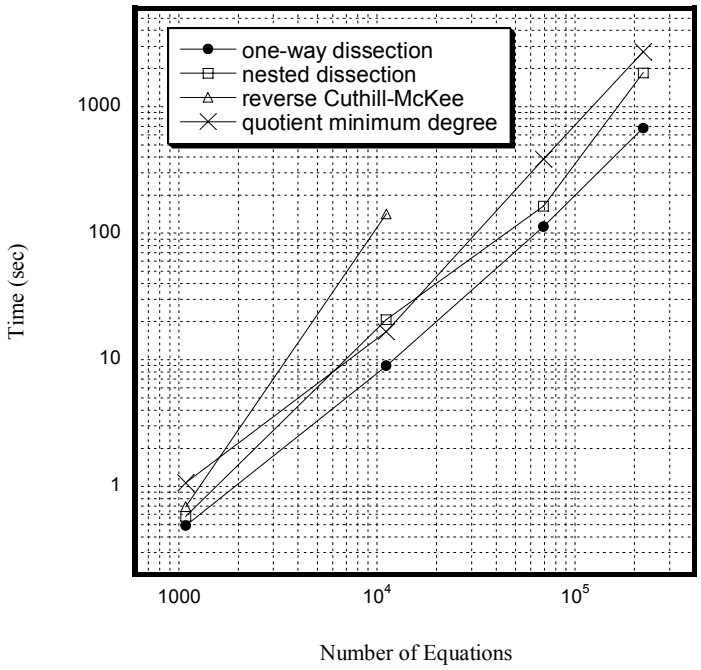

Figure 5. 5 Elapsed wall-clock time to solve the linear systems using BiCGSTAB with alternate matrix reorderings.

The results for elapsed wall-clock time versus number of equations are shown in Figs. 5.4 and 5.5. The measure includes the cost of successive iterative approximation on the Krylov subspace, as well as setting up and applying the preconditioner. BiCGSTAB was slightly faster than the other two solvers, but no significant difference was observed among the three methods when they were used with one-way dissection ordering. A significant effect of reordering on computing time can be seen in Figure 5.5; OWD was always the fastest, followed by ND, QMD, and RCM.

5.3.2 With Fill-in

The ILU(0) preconditioner was successful in solving our linear systems, and has the advantage of low memory requirements due to no fill-in (memory requirements for

ILU(k) preconditioners are compared later). A trade-off, however, is that the accuracy of ILU(0) might be insufficient to yield an efficient rate of convergence. Table 5.4 shows that the required number of iterations to reach convergence decreases substantially using a level one fill-in preconditioner, ILU(1), for all three iterative methods. Both BiCGSTAB and TFQMR outperform GMRES. The difference in convergence rate is more significant between reordering schemes than across Krylov methods. Again, one-way dissection showed the fastest convergence and reverse Cuthill-McKee the slowest, although its lack of convergence with ILU(0) was resolved for the large problems (MESH3 and MESH4). Further improvement of convergence rate can be achieved by allowing more fill-in. Figure 5.6 shows convergence rates for case MESH4 using BiCGSTAB and OWD with increasing level of fill-in.

Krylov method	BiCGSTAB + ILU(1)				TFQMR + ILU(1)				GMRES + ILU(1)			
Ordering	OWD	ND	RCM	QMD	OWD	ND	RCM	QMD	OWD	ND	RCM	QMD
MESH1	4	4	4	4	4	4	4	4	6	7	7	6
MESH2	7	8	7	8	8	7	7	8	11	13	12	14
MESH3	12	13	23	15	11	15	21	16	20	24	29	25
MESH4	20	24	61	23	20	23	59	25	32	40	54	40

Table 5. 4 Required number of iterations to solve the linear systems using alternate Krylov methods and ILU(1) preconditioning.

Table 5.5 shows that the decreased number of iterations with ILU(1) resulted in fewer flops than with ILU(0). However, unlike the iteration number comparison, none of the three iterative methods clearly outperformed the others in the flop measurement. Since the matrix-vector product with ILU(1) includes more nonzero entries, the

biorthogonalization process becomes more complicated. In other words, BiCGSTAB and TFQMR converge faster than GMRES, but each iteration with ILU(1) in BiCGSTAB and TFQMR requires significantly more flops than an iteration in GMRES. The effects of reordering methods with ILU(1) are the same as with ILU(0). Results for the elapsed clock time with ILU(1) showed trends similar to those with ILU(0) (Figs. 5.4 and 5.5), and are therefore not shown here.

Krylov method	BiCGSTAB + ILU(1)				TFQMR + ILU(1)				GMRES + ILU(1)			
Ordering	OWD	ND	RCM	QMD	OWD	ND	RCM	QMD	OWD	ND	RCM	QMD
MESH1 ($\times 10^6$)	6.57	10.0	7.18	7.66	6.92	10.5	7.53	8.77	6.34	10.2	7.39	8.12
MESH2 ($\times 10^8$)	0.96	1.54	1.07	1.37	1.13	1.54	1.15	1.47	0.96	1.55	1.12	1.44
MESH3 ($\times 10^9$)	1.33	2.19	2.30	1.95	1.36	2.49	2.36	2.19	1.38	2.35	2.04	2.03
MESH4 ($\times 10^{10}$)	0.78	1.32	1.91	1.07	8.50	1.38	2.07	1.21	0.81	1.36	1.25	1.14

Table 5. 5 Number of flops (the exponent for each mesh case is shown in parentheses) to solve the linear systems using alternate Krylov methods and ILU(1) preconditioning.

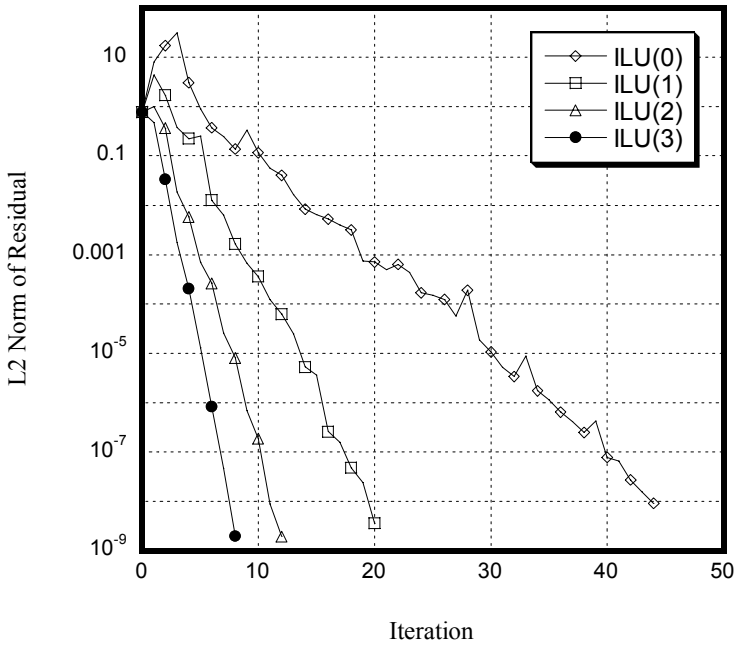

Figure 5. 6 Improvement of convergence rate using higher level of fill-in using BiCGSTAB and one-way dissection reordering for case MESH4.

In addition to convergence rate and number of flops, memory requirements also need to be considered when choosing an optimal level of fill-in. Since the structure of nonzero entries of a coefficient matrix varies with reordering method, different amounts of fill-in are expected after each level of incomplete LU factorization for a given reordering method. Table 5.6 shows the fill ratio, defined as the ratio of the number of nonzero entries in the incomplete LU factorization to the number of nonzero entries in the original coefficient matrix. The numbers of iterations required for convergence is given in parentheses. A higher fill-in ratio results in a more accurate preconditioner and fewer iterations to convergence. This is true for all four reordering methods. Note that the instability of incomplete factorization (unstable forward or backward substitution with the incomplete factors) mentioned in [10, 15] has not been observed in this study. Again,

in terms of memory requirements, one-way dissection was the most cost-effective among the four methods, and nested dissection was the most expensive.

	OWD	ND	RCM	QMD
ILU(0)	1.00 (44)	1.00 (141)	1.00 (*)	1.00 (194)
ILU(1)	1.91 (20)	2.58 (24)	2.06 (61)	2.25 (23)
ILU(2)	3.21 (12)	4.72 (13)	3.56 (13)	3.91 (14)
ILU(3)	4.96 (8)	6.87 (9)	5.50 (8)	5.79 (9)

Table 5. 6 Fill ratio of ILU(k) and required number of iteration using BiCGSTAB for MESH4 matrix.

In PETSc, the compressed (or Yale) sparse row (CSR) format is used [6]. The more accurate ILU(k) preconditioners produce more fill-in and thus larger memory requirements. Figure 5.7 shows the fill ratio and memory requirement for increasing ILU(k) level using BiCGSTAB and one-way dissection reordering. The choice of an optimum level of fill-in for the ILU(k) preconditioner is also influenced by the computation time for both preconditioning and iterative solution. As shown in Figure 5.8, again using BiCGSTAB and one-way dissection reordering, the time for preconditioning increases significantly with the level of fill-in, but the time for iterative solution decreases from ILU(0) through ILU(2), after which it increases. Note that the fill ratio jumps dramatically from ILU(2) to ILU(3) (see Table 5.6) and also that the solution time for ILU(3) increases due to the large increase in nonzero entries. ILU(0) and ILU(1) require about the same total computing time, thus ILU(0) is preferred because of lower memory requirements. However, ILU(1) or ILU(2) could be the better choice when the same linear system needs to be solved repetitively with different right hand side vectors, such

as for linear time dependent problems, since preconditioning can be performed once and used for all time steps.

As will be mentioned in the next chapter in conjunction with the solution of larger 3D contact problems, this study on linear biphasic systems has provided significant guidance in the choice of iterative solver and strategy in the 3D biphasic contact problem. In addition, it has been used to select iterative methods used by others in our laboratory for 3D nonlinear biphasic analysis [85].

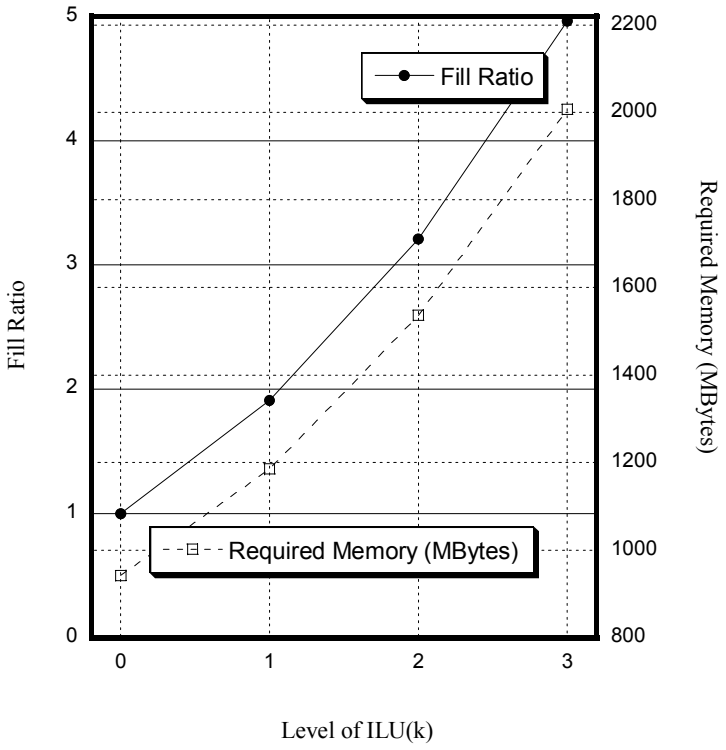

Figure 5. 7 Fill ratio and memory requirement versus level of ILU(k) fill-in using BiCGSTAB and one-way dissection reordering for case MESH4.

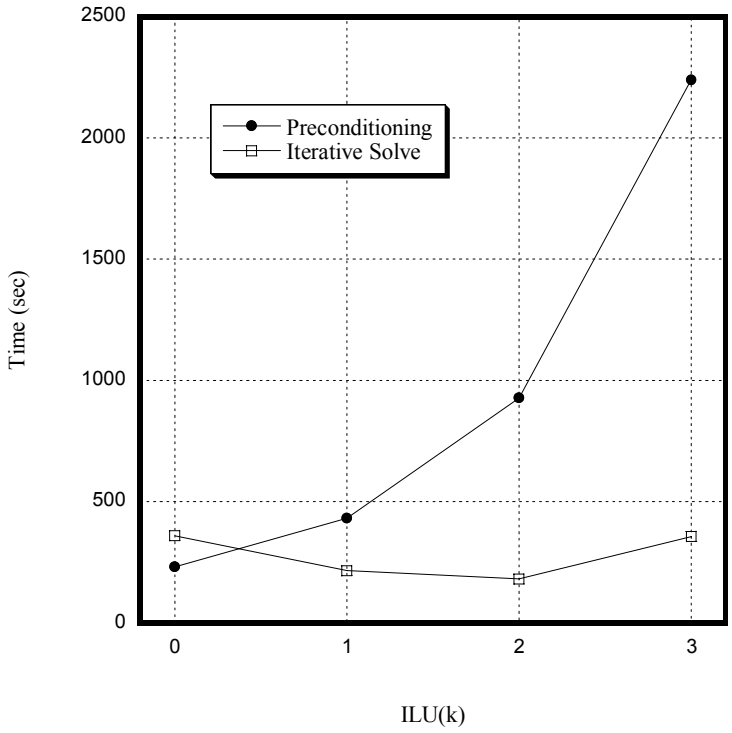

Figure 5. 8 Elapsed wall-clock time for preconditioning and iterative solution using BiCGSTAB and one-way dissection, versus level of fill in, for case MESH4.

Chapter 6: Three-Dimensional Biphasic Contact Problems

6.1 Introduction

Before the proposed formulation (the primary variable based formulation) is applied to physiological problems, both theoretical and numerical implementations should be verified through canonical examples. First, simple mechanical tests of hydrated soft tissue are used for which analytical solution exists. In particular, for the confined and perfectly lubricated unconfined compression test, tissue-to-tissue contact problems can be defined which should yield the same results as the analytical solution for a single tissue. The contact solution results should obey the time-dependent behavior of soft tissues, while satisfying the contact continuity conditions, Eqs. (2.54) to (2.57) along the contact area. Second, the elastic Hertz contact problem is solved using a pseudo biphasic analysis in order to verify that the Kuhn-Tucker conditions are satisfies, and ensure the capability of the contact algorithm to predict the correct contact surface for an evolving contact problem. Next, biphasic indentation tests are performed to further verify the formulation, and demonstrate both the enforcement of continuity conditions and the prediction of a correct contact surface. After the above validations, the gleno-humeral joint (GHJ) contact of the human shoulders is analyzed as a demonstration for a clinically significant problem.

The experimental study on the *Krylov* iterative solvers in Chapter 5 provides guidance in the choice of a suitable solution scheme for biphasic contact problems. As

the Lagrange multipliers are introduced in the contact formulation, the global linear system becomes symmetric, semi-indefinite, including zero entities on the diagonal. Accordingly, the performances observed in the previous Chapter are not expected to be exactly the same. The sparse ILU factorization with matrix reordering provided in PETSc [6] often failed with a zero pivot for biphasic contact analyses. It was also observed that the BiCGSTAB method converges very slowly or even diverges for the evolving contact situations. The ILU(1) preconditioned TFQMR with reverse Cuthill reordering method showed good convergence performance for most of the 3D contact examples, and was therefore used for all analyses in this chapter.

6.2 Confined Compression Test

It is widely accepted that the transient viscoelastic response of the tissue results from the interaction between the solid and fluid phases. There are two fundamental tests that describe the rheological characteristics of soft tissues: the creep and stress relaxation tests. In a creep test, a constant load is applied, and the deformation of the tissue is observed as a result of fluid exudation. In stress relaxation, the applied displacement is controlled, and the stress required to maintain this displacement is measured over time. These two tests are used to verify the current contact methodology. Contact results will be compared with the analytical solutions [58] for single tissue cases. Also, enforcement of the continuity conditions across the contact surface will be examined.

Figure 6.1 (a) illustrates a schematic of the confined compression (CC) test modeled as a contact problem. In a lubricated solid chamber, two tissue samples are positioned vertically with an initial gap of 0.0001 mm. Each tissue sample has a

dimension of $1\times1\times1$ mm^3 (w = 1 mm and h/2 = 1 mm). Either traction or displacement is applied on top of the tissue for CC creep or CC stress relaxation test as shown in Figs. 6.1 (b) and (c) to simulate a rigid, free-draining platen. Fluid can therefore freely exude through the top surface. The response to these boundary conditions is one-dimensional, with variation in the z-direction only. For both creep and stress relaxation tests, 10 % of total strain is expected at equilibrium. The material properties are chosen for both tissues to simulate normal human cartilage [58]: Young's modulus E = 0.675 MPa, Poisson's ratio ν = 0.125, permeability $\kappa = 7.6\times10^{-3}$ mm^4/N/sec and solid content ϕ^s = 0.17.

The problem domain is discretized with finite elements in two ways (see Fig. 6.2): (a) A total of 420 tetrahedral elements with 24 triangular contact elements that are node-to-node aligned. (b) A total of 363 tetrahedral elements with non-matching contact elements (32 triangular elements on bottom surface of the top tissue sample and 30 elements on top of the bottom tissue).

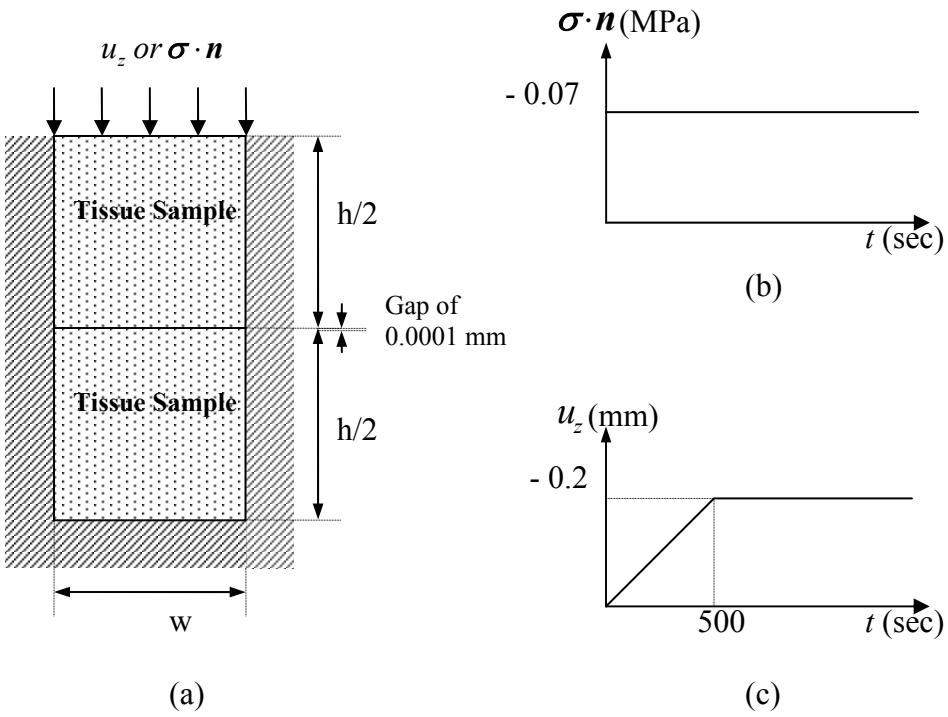

Figure 6. 1 (a) A schematic of the uni-axial confined compression test, (b) traction boundary condition for a creep test, (c) displacement boundary condition for a stress relaxation test.

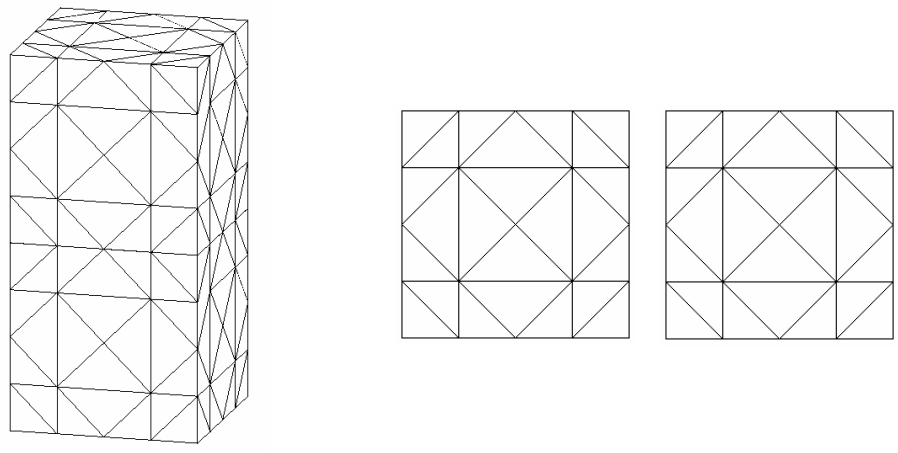

(a)

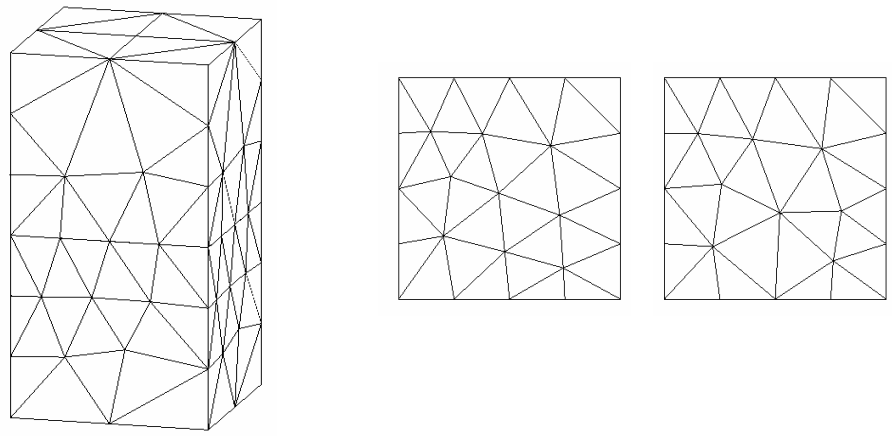

(b)

Figure 6. 2 Finite element meshes of (a) 420 tetrahedral elements with 24 matching contactor elements, (b) 363 tetrahedral elements with 32 (left) and 30 (right) contact elements.

For a time dependent contact analysis, Donzelli [18] suggests a fully implicit method to precisely track the current velocity. When the finite difference parameter $\omega = 1$ the current velocity is calculated only from the displacement values, independent of the velocity history. Although this choice reduces the time accuracy to first order,

compared to second order accuracy of a Crank-Nicolson scheme ($\omega = 0.5$), the solution does not oscillate regardless of the size of time step [38]. In the analyses which follow, time integration parameters are chosen as: $\omega = 1.0$, initial time t_0 = 5 sec., final time, t_f = 1000 sec., size of time step Δt = 5 sec.

6.2.1 CC Creep

Figure 6.3 (a) shows tissue deformation at the top of tissue ($z = 2.0$ mm) normalized by the equilibrium displacement ($\bar{u}_z = 0.2$ mm). For both matching and non-matching mesh, results show good agreement with analytical solution [58]. Displacement variations through the depth are shown in Fig. 6.3 (b) at t = 50, 500 and 1000 sec. At early time (t = 50 sec.), most of the deformation is in the upper part of the tissue. Later on (t = 1000 sec.), deformation is uniformly distributed throughout the entire tissue.

Other results of interest for the confined compression creep test are the pressure changes in time. Pressure variation through the thickness is presented in Figure 6.4 at t = 50, 500 and 1000 sec. Pressure is normalized by the aggregate modulus, $H_A = 0.7$ MPa. Note that the applied traction is mostly supported by the fluid phase at earlier time (t = 50 sec.), and is transmitted to the solid phase as the fluid exude at t = 1000 sec. For displacement and pressure, the contact finite element results show good agreement with analytical solutions [35, 58].

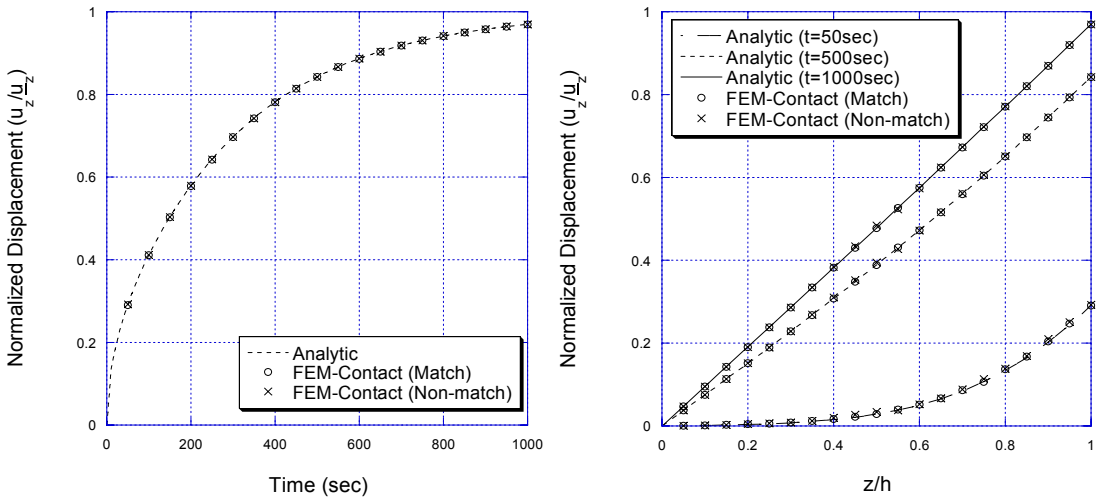

(a) (b)

Figure 6. 3 (a) Normalized displacement in the confined compression creep test at the top of tissue in time (b) normalized displacement through the depth at t = 50, 500 and 1000 sec.

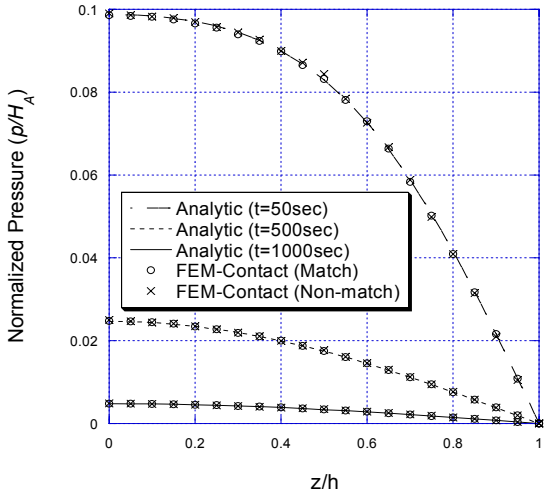

Figure 6. 4 Normalized pressure through the depth in the confined compression creep test at t = 50, 500 and 1000 sec.

Of equal interest is the enforcement of continuity conditions on the contact surface, Eqs. (2.54) to (2.57). For both meshes, the top surface of the bottom tissue is chosen as the contactor. Figure 6.5 (a) compares the solid displacements u_z^s from contactor and target across the contact surface, from (0,0) to (1,1), over time. Although there are slight variations in the displacement continuity from the non-matching mesh, they occur in the third or fourth significant digit and are not problematic. Pressure continuity across the contact surface is closely satisfied over the time in Fig. 6.5 (b).

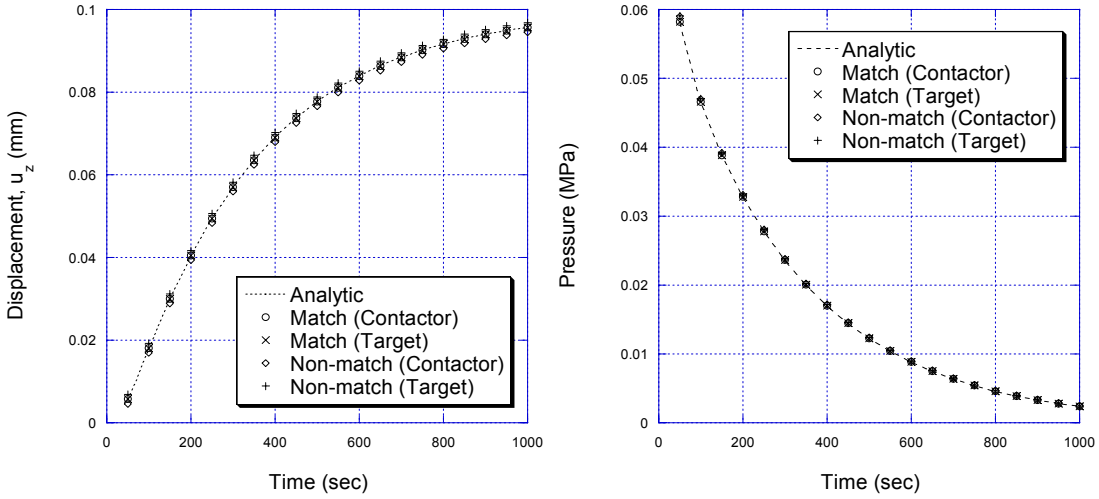

(a) (b)

Figure 6. 5 Continuity conditions of (a) solid displacement u_z^s, (b) pressure from the matching and non-matching contact elements in the confined compression creep test.

A noticeable discrepancy is observed for the continuity enforcement of the derived variables of the *v-p* formulation. Figure 6.6 (a) to (d) show the solid stress and

the relative fluid velocity for the matching and non-matching meshes, respectively. The discrepancy can be explained for two reasons. First, the creep is not fully developed at early times and therefore the gradients of displacement and pressure are more severe. Consequently, there are differences in normal stress and relative fluid velocity across the contact boundary at 500 sec. At 1000 sec., the continuity of solid stress is more closely satisfied, as the creep progresses close to the equilibrium.

The gradients further contribute to perceived discrepancy in continuity of derived quantities because of the methods used to post-process results in our software. For the visualizing purposes, the software Data Explorer [40] is used throughout this study. It is a powerful and useful tool, but has certain limitations. For some nodal quantities (primary variables) solid displacement, it cannot represent the true finite element interpolations. Instead, nodal values at element vertices are linearly interpolated (whereas displacement is a quadratic interpolation for the 3D biphasic element used here). Also, to represent the element quantities such as stress, strain and the pressure gradient, the quantities are evaluated at the centroid of the tetrahedron. These quantities are then averaged at vertices using centroidal data from adjacent elements, and then interpolated by Data Explorer throughout the problem domain using the linear interpolations just mentioned. Therefore, if there are high gradients of nodal quantities the element quantities may not be exactly evaluated. As expected, when the finite elements are made sufficiently small, the current Data Explorer data does not show any appreciable error. The discrepancy at the earlier time will therefore be minimized with mesh refinement in z-direction.

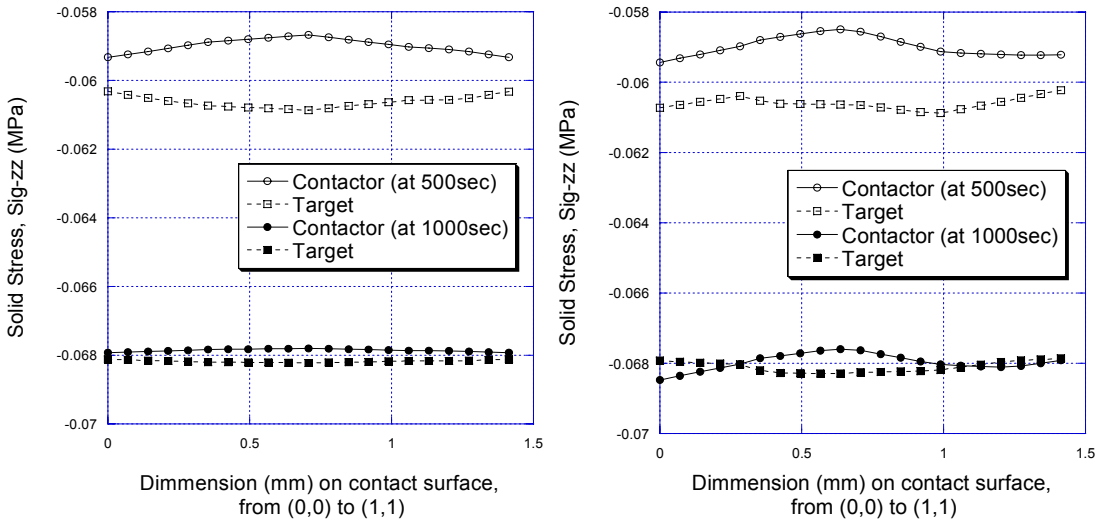

(a) (b)

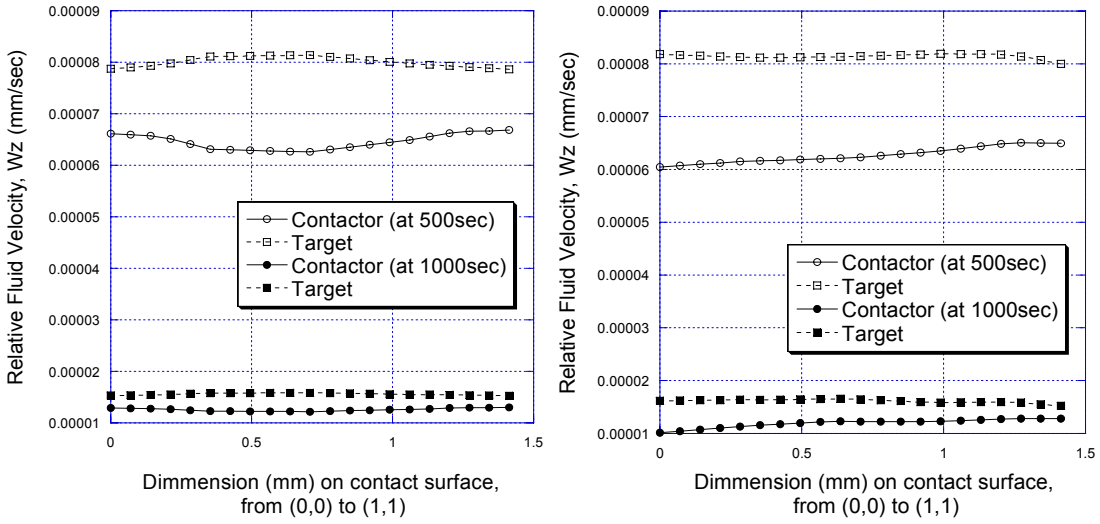

(c) (d)

Figure 6. 6 Continuity conditions of solid stress σ_{zz}^{s} (a) for matching mesh, (b) for non-matching mesh, and of relative fluid velocity $W_z = -\kappa p_{,z}$ (c) for matching mesh, (d) for non-matching mesh in the confined compression creep test.

6.2.2 CC Stress Relaxation

Figure 6.7 compares pressure distributions (a) through the depth and (b) in time for both the matching and non-matching meshes. Again, the finite element results show good agreement with the analytical solution. Pressure is zero at the top of tissue (z = 2.0) as the fluid phase freely exudes, and increases through the depth (Fig 6.7 (a)). As more displacement is applied up to $t = 500$ sec., pressure increases. And then, as soon as the applied displacement is held constant, pressure starts to decrease with fluid efflux (Fig 6.7 (b)) and stress in the tissue is redistributed. Meanwhile, the continuity conditions (although not shown here) are noted to be accurately enforced throughout the entire time.

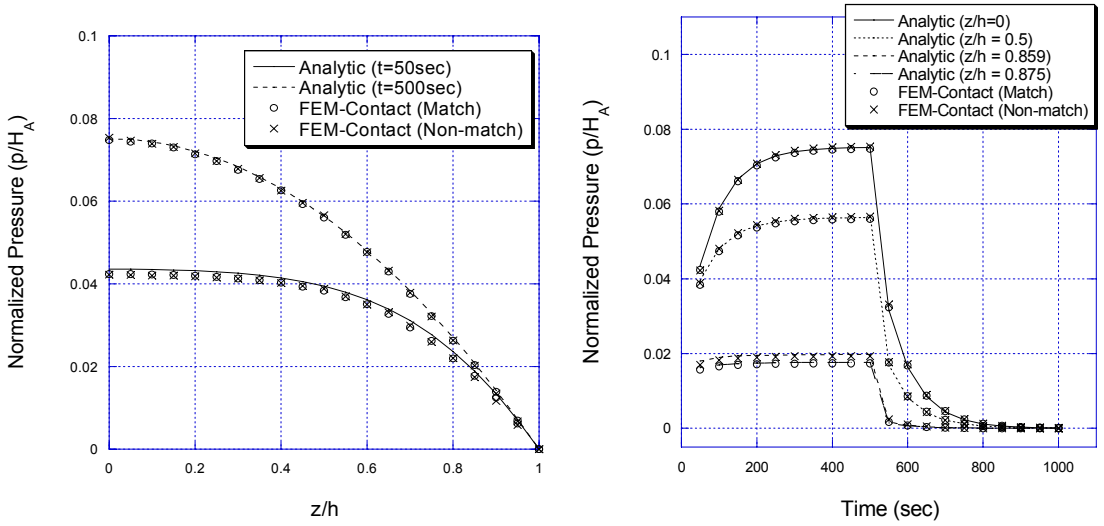

(a) (b)

Figure 6. 7 (a) Normalized pressure in the confined compression stress relaxation test through the depth at t = 50 and 500 sec., (b) normalized pressure in time at z/h = 0, 0.5, 0.875.

6.3 Unconfined Compression Test

The unconfined compression test is often performed experimentally to determine the intrinsic material properties of biological tissues such as cartilage. In this test, a thin cylindrical disk of tissue is compressed between two rigid impermeable platens, while fluid can freely exude through the side of the tissue. The upper platen is given a prescribed displacement and the lower platen is fixed. Figure 6.8 shows a schematic of the unconfined compression stress relaxation test. Both platens are assumed to be perfectly lubricated, i.e., frictionless between the tissue and platens. Under this assumption, the applied displacement yields a quasi-one dimensional expansion in the radial direction, which is independent of z location. The analytical solution for this problem has been developed by Armstrong *et al.* [2].

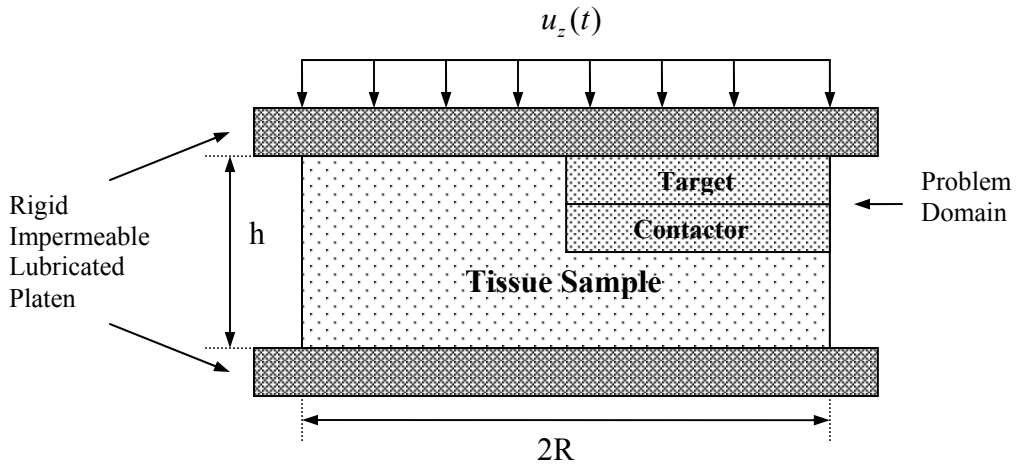

Figure 6. 8 A schematic of the perfectly lubricated unconfined compression stress relaxation test of a cylindrical disk of hydrated soft tissue.

The tissue sample has h = 2 mm and R = 3 mm. The applied displacement increases linearly from $u_z = 0$ at $t = 0$ to $u_z = -0.05$ mm at $t = 500$ sec., and then the platen is held. Material parameters are identical to those used in the confined compression examples. Due to symmetry with respect to the mid-height and the central axis, only the upper right quadrant of the tissue is considered in the finite element analysis.

Two analyses are used in this validation example. An analysis of the complete quadrant shown in Figure 6.8 is performed with 1994 tetrahedral elements (see Fig. 6.9 (a)). For the contact analysis, the quadrant is divided into two parts of equal height. Fig. 6.9 (b) shows the finite element mesh for a contact analysis where the initial gap of 0.0001 mm between tissues is exaggerated for visualization purposes. The mesh consists of 1639 tetrahedral elements and 138 triangular contact elements. Notice that the two contact surface are discretized with the same number of elements, but they are not exactly node-to-node aligned. The lower tissue is chosen to be the contactor and the upper tissue the target. The contact analysis results are expected to reproduce the solution from the single tissue analysis, while satisfying the contact continuity conditions.

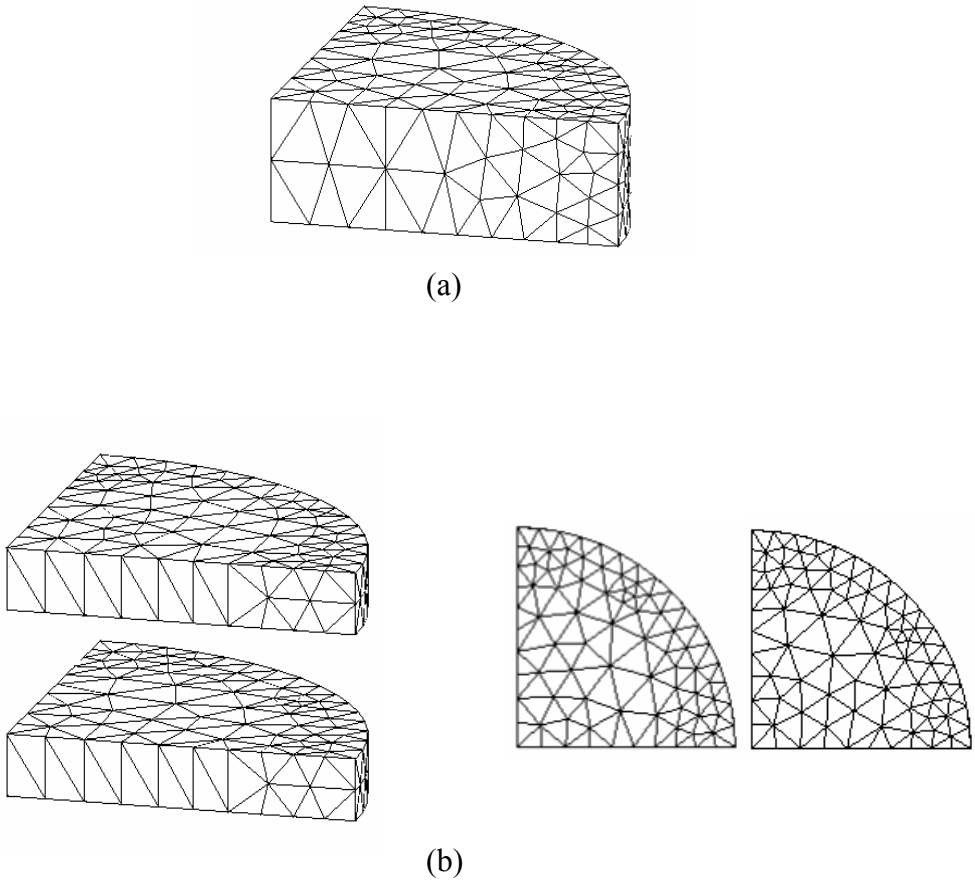

Figure 6. 9 Finite element meshes for (a) single tissue test with 1994 tetrahedral elements and for (b) contact test with 1639 tetrahedral and 138 contactor elements

Unlike the confined compression test, there is fluid efflux on the outer radial surface of the tissue. This can be modeled with the free draining boundary condition, i.e., pressure is set to be zero. For the elements on the contact boundary of either the upper or lower tissue that have a face on the contact surface, nodes of which touch this outer radial surface, as many as two of the three pressure degrees of freedom (DOF) of that face will be set to zero. This will change the constraint ratio counts that were done in conjunction with the contact patch test in Chapter 4 as follows. There are the same number of

Lagrange multiplier λ^f DOF and pressure DOF for the non-singularity condition with the continuous linear interpolating function (see condition (iii) in Table 4.2). However, there is now a significant imbalance between the numbers of these two variables for the elements adjacent to the outer radial boundary. Three λ^f DOF versus one pressure DOF can cause a local singularity along that boundary, which can preclude convergence of the iterative solver. Therefore, for this example, the discontinuous functions for λ^s and λ^f described in Chapter 4 are used, and the results show that the continuity conditions are accurately satisfied.

To demonstrate the overall accuracy of the contact formulation, the radial solid velocity as a function of time is plotted at the mid-height of the outer tissue surface (at the bottom of the outer surface in problem domain) in Figure 6.10. The results from the contact analysis show good agreement with those from the single tissue analysis. This suggests that the applied displacement on the upper tissue is precisely transmitted to the lower tissue through the contact surface.

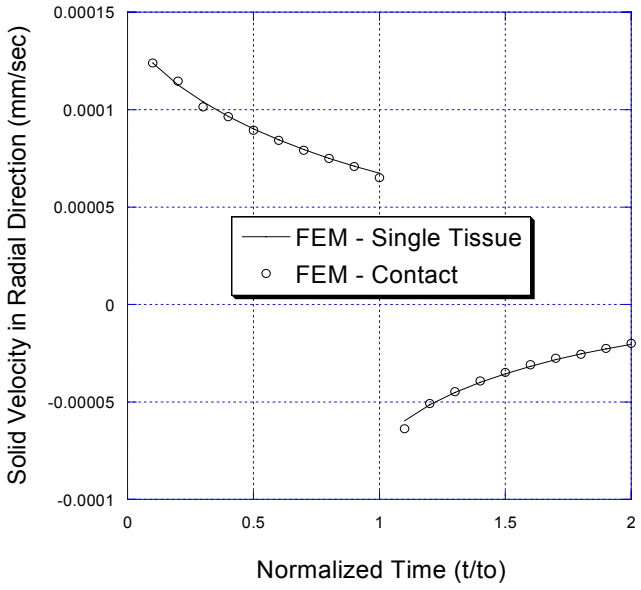

Figure 6. 10 Solid velocity in radial direction at the mid-height of the outer surface for the unconfined compression stress relaxation test. (time is normalized by t_o = 500 sec.)

Figure 6.11 shows the continuity of solid velocity in the axial direction along the contact surface at 250 sec. The solid line displays the solutions from the single tissue analysis and the symbols are from the contact analysis. Although some noticeable discrepancies exist, the continuity is considered adequately enforced with a maximum error of 0.57 %. Figure 6.12 compares (a) pressure and solid stresses and (b) the relative fluid velocity along the contact surface at 250 sec. The results demonstrate again that the current contact formulation is capable of producing the required continuity conditions, in this case for distributions which vary over the contact surface. Pressure is maximum at the center of the tissue and gradually decreases to zero at the outer surface. Axial solid stress is compressive and nearly constant, and shear stress is zero in agreement with frictionless contact assumption. The relative fluid velocity in the axial direction is zero

across the contact surface except near the outer surface where some discrepancy occurs. However, the values are negligibly small compared to other variables of interests.

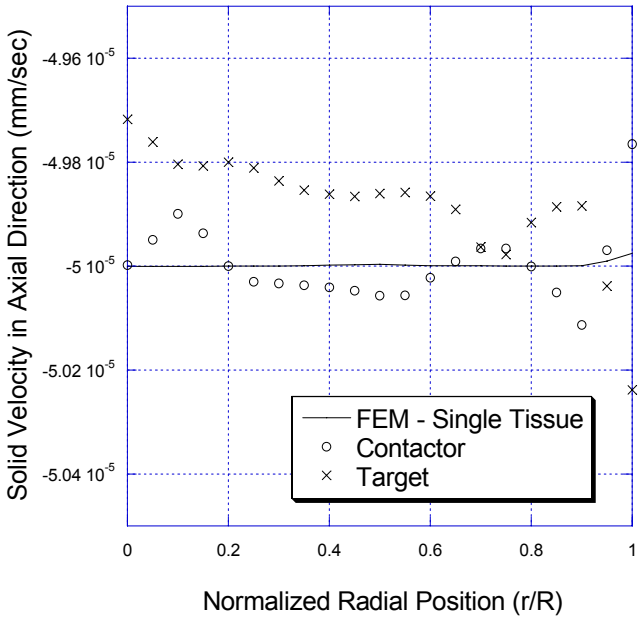

Figure 6. 11 Solid velocity in axial direction across the contact surface at 250 sec. for the unconfined compression stress relaxation test.

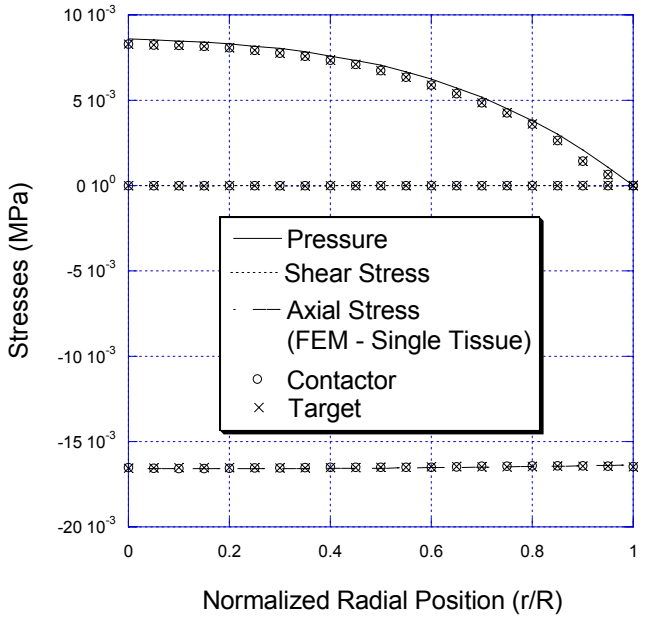

(a)

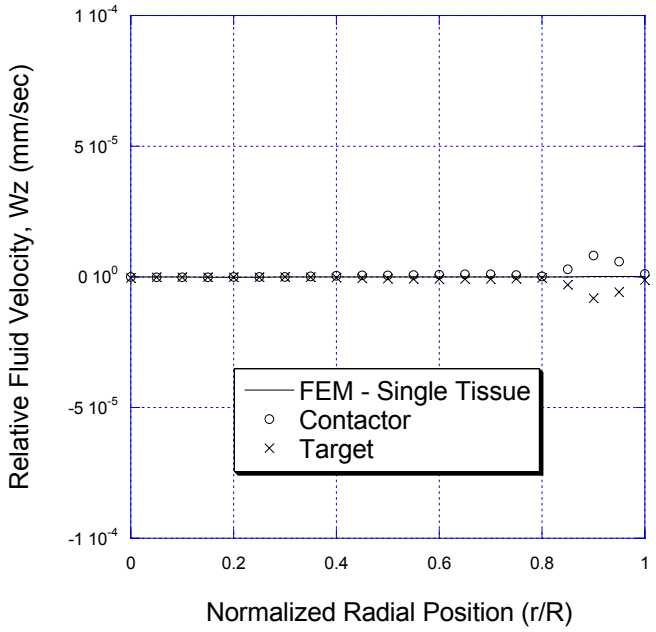

(b)

Figure 6. 12 (a) Fluid pressure and solid stresses, (b) relative fluid velocity across the contact surface at 250 sec. for the unconfined compression stress relaxation test.

6.4 Hertz Contact

The solution by Hertz [33] is one of the few available analytic solutions for problems where contact area and contact pressure are simultaneously changing with the applied load. However, the static Hertz contact solution can not be comparable directly with the current time-dependent biphasic contact solutions that involve interstitial fluid flow. However, the deforming elastic medium of the static Hertz contact problem can be approximated using the biphasic analysis by using a large value for the solid volume fraction, ϕ^s, and high permeability, κ, to minimize the time-dependent effects of fluid motion.

Figure 6.13 (a) illustrates the Hertz problem where the elastic cylindrical foundation is indented by a rigid spherical indenter. The foundation has w = 5 mm and h = 2 mm and the indenter has a radius r = 10 mm. A uniform displacement u_z = - 0.01 mm is applied on the top of the indenter and the bottom surface of the foundation is fixed. For free fluid exudation outside of contact surface, zero pressure boundary condition is applied to the inactive contact elements according to contact search results.

Figure 6.13 (b) shows the finite element mesh composed of 20112 tetrahedral elements for both the indenter and foundation. The foundation surface is chosen as the contactor and discretized with 804 triangular contact elements. The cylindrical foundation has material properties as: Young's modulus E^A = 1.0 MPa, Poisson's ratio ν^A = 0.125, constant permeability, $\kappa^A = 4.0\times10^{-12}$ m^4/N/sec and solid content, ϕ^{sA} = 0.95. The properties for the indenter are chosen to approximate the rigid indenter by making the modulus 1000 times that of the foundation: E^B = 1000 MPa, ν^B = 0.125, κ^B

= 4.0×10^{-12} m^4/N/sec and ϕ^{sB} = 0.95. The capability of the proposed element is validated to calculate the correct contact surface for an evolving contact problem while satisfying Kuhn-Tucker conditions.

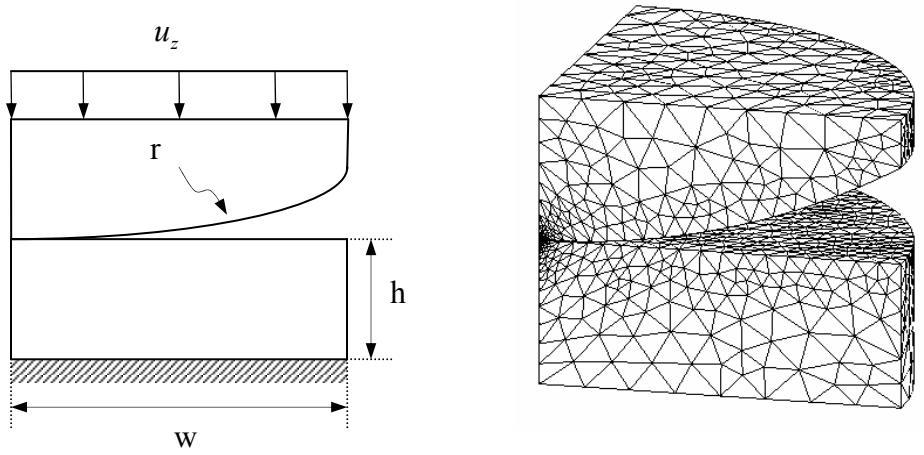

(a) (b)

Figure 6. 13 (a) A schematic of Hertz contact problem (b) finite element mesh

Figure 6.14 shows (a) the distribution of displacement and (b) the deformed surface geometry after 5 contact iterations. The elastic foundation deforms geometrically smooth along with rigid body motion of the indenter. The computed contact area agrees with the Hertz solution of 0.316 mm. Distributions of strain and stress are given in Fig. 6.15 (a) and (b), respectively.

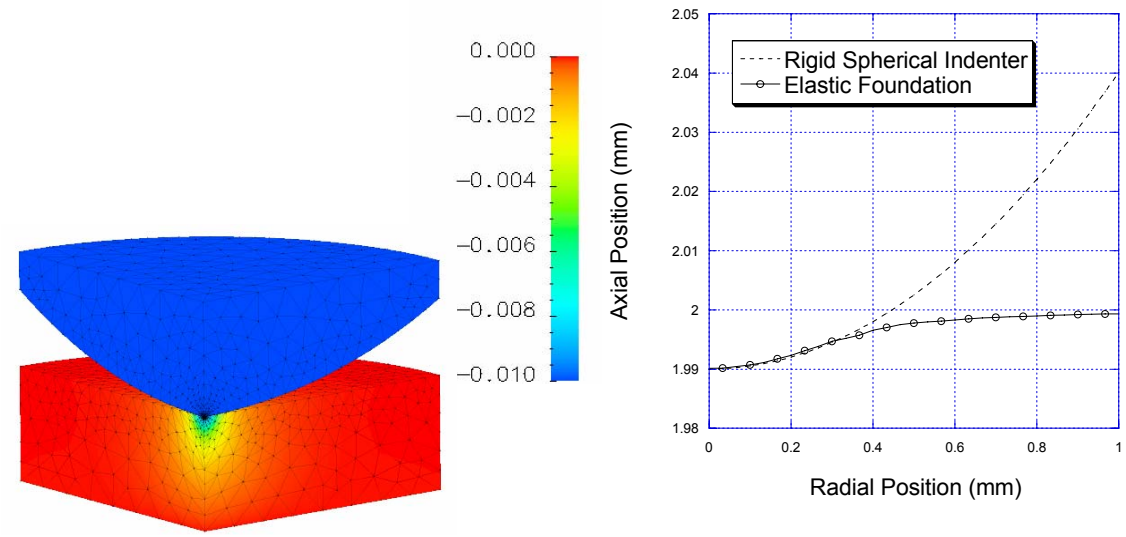

(a) (b)

Figure 6. 14 (a) Distribution of displacement, (b) Deformed surface geometry for 0.01 mm displacement of the spherical indenter.

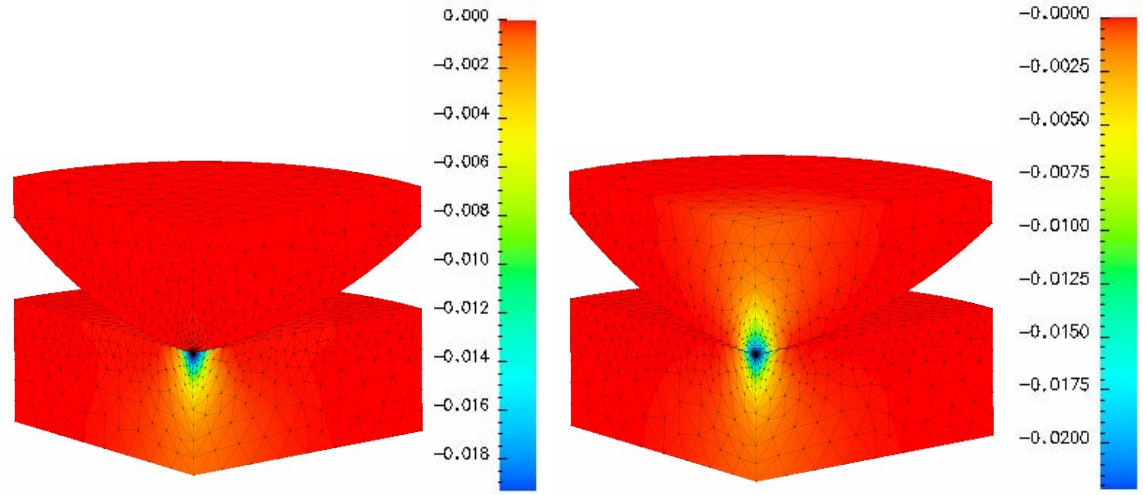

(a) (b)

Figure 6. 15 (a) Distribution of strain, (b) Distribution of stress (in MPa) for 0.01 mm displacement of the spherical indenter.

6.5 Biphasic Indentation Test

In the previous sections, the capability of the biphasic contact methodology has been shown to enforce the contact continuity conditions, and to predict the correct contact area. The methodology is now further tested using two biphasic indentation tests: one with a flat-ended cylindrical and the other with a cylindrical-ended indenter.

6.5.1 Analysis using a Flat-Ended Cylindrical Indenter

Indentation experiments on a hydrated soft tissue are widely used to determine the intrinsic material properties, such as permeability, κ, and the elastic coefficients, E and ν, of the solid phase for linear biphasic tissues. The popularity of the test was initially due to the relative ease of performance and the availability of an analytical solution for elastic contact [33]. A mathematical solution of the biphasic indentation test has been developed by Mak *et al.* [54] using double Laplace and Hankel transform techniques. A finite element solution has been presented by Spilker *et al.* [79] where they compared the permeable and frictional effects of the indenter.

Figure 6.16 (a) illustrates a schematic of the indentation test with a flat-ended cylindrical indenter. A quadrant of the problem domain is modeled and discretized with total of 14,647 tetrahedral elements (for both the indenter and cartilage) with 294 triangular contact elements (on the cartilage surface) shown in Fig. 6.16 (b). The indenter is positioned normal to the cartilage surface and subjected to a ramp displacement. The indenter of a radius R_{ind} = 0.75 is assumed to be rigid, porous, and frictionless. The cartilage of a thickness h = 0.75 mm and a radius R_o = 3.0 mm is bonded to an impervious, rigid subchondral bone. The indenter and the cartilage are

placed with an initial gap of 0.0001 mm. The bone is not explicitly modeled, instead a fixed boundary condition is applied to the bottom surface of the cartilage. Displacement boundary condition is applied on the top of indenter, increasing linearly from $u_z = 0$ at $t = 0$ to $u_z = -0.075$ mm at $t = 500$ sec., and then the indenter is held. Zero pressure boundary condition is applied on the top of the indenter and on the cartilage surface outside of contact surface. Following Spilker's model, the material properties for the cartilage are: Young's modulus E^A = 0.5417 MPa, Poisson's ratio ν^A = 0.0833, constant permeability, $\kappa^A = 4.0\times10^{-15}$ m^4/N/sec and solid content, $\phi^{sA} = 0.2$. Properties for the rigid indenter are: E^B = 541.7 MPa, ν^B = 0.125, $\kappa^B = 4.0\times10^{-12}$ m^4/N/sec and ϕ^{sB} = 0.95.

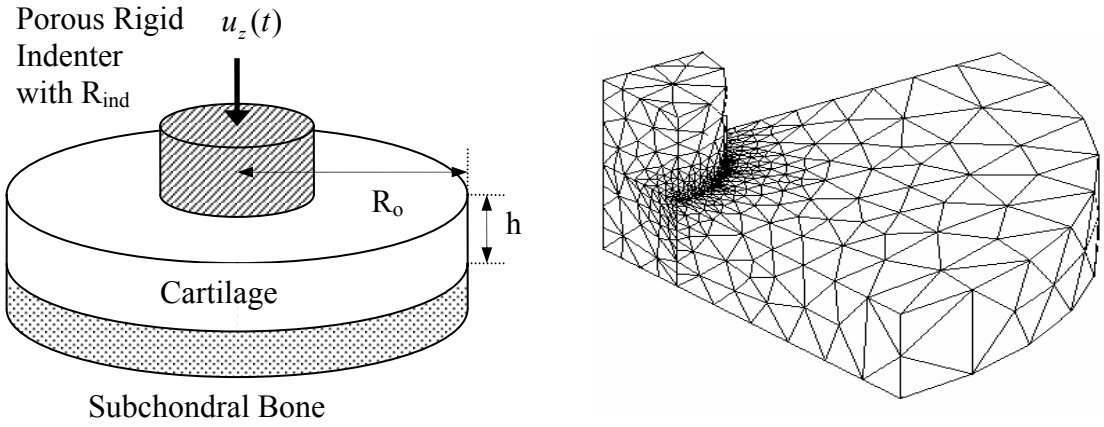

Figure 6. 16 (a) A schematic of the biphasic indentation test with a flat-ended cylindrical indenter, (b) The finite element mesh with 14647 tetrahedral elements and 294 contact elements.

First, results on traction-like quantities are compared with Spilker *et al*. [79]. For the axial strain and stress (in Fig. 6.17 (a) and (b)), contact solutions show a fair agreement with Spilker et al. versus the radial position. However, noticeable difference is found near the edge of indenter where severe gradients of strain and stress occur. If the mesh is further refined around the edge, higher gradients will be properly represented along the circumference of this singular point. Unlike axial stress, the radial distribution of pressure (in Fig. 6.18) varies smoothly and increases with depth, and the solutions are in good agreement.

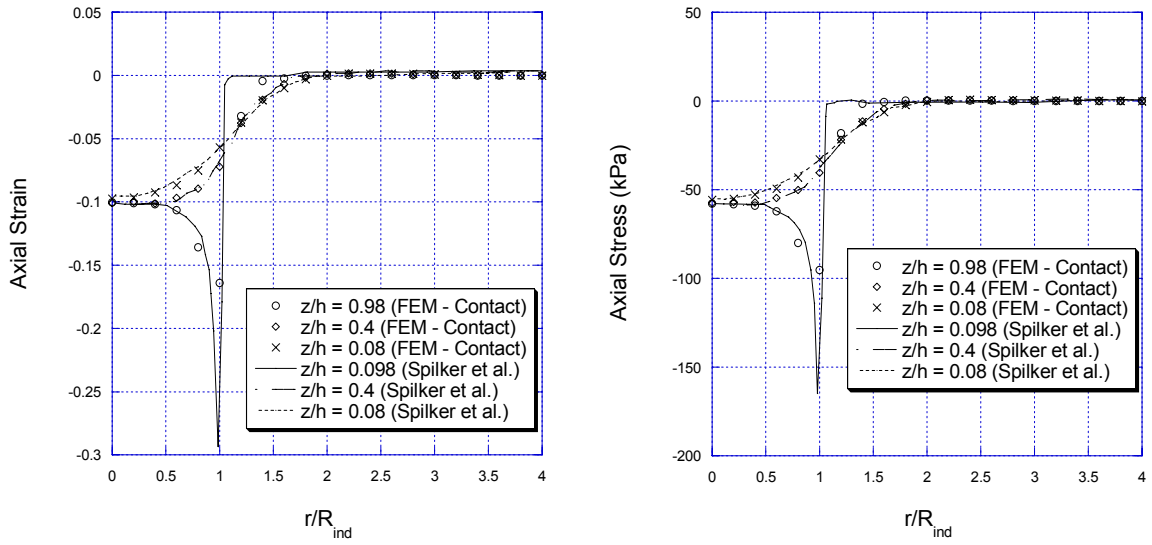

(a) (b)

Figure 6. 17 (a) Axial strain and (b) axial stress along the radial position at several depths at 500 sec. in the biphasic indentation test with a flat-ended cylindrical indenter.

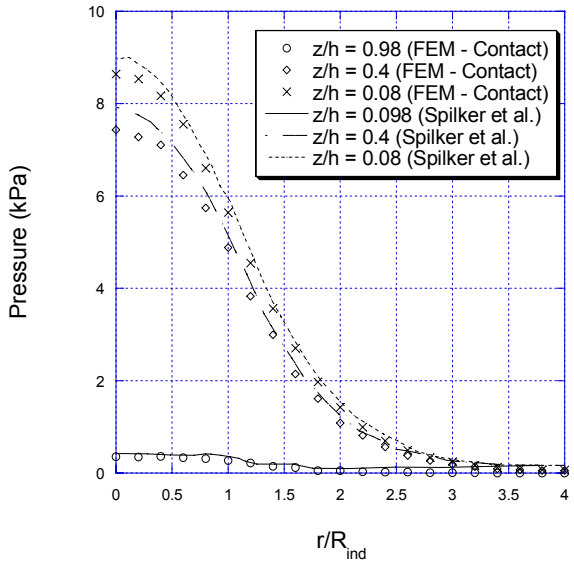

Figure 6. 18 Pressure along the radial position at several depths at 500 sec. in the biphasic indentation test with a flat-ended cylindrical indenter.

Next, the enforcement of contact continuity conditions is examined. In Figs. 6.19 – 22, the distributions of displacement, pressure, normal solid stress and relative fluid velocity at 250 sec. are displayed on the left. The continuity of the quantities across the contact surface is compared in the figures on the right. The cartilage surface is chosen as the contactor and the indenter as target. For the primary variables, the continuity conditions are accurately satisfied. On the contact surface, the cartilage deforms along with the flat-ended indenter in Fig. 6.19 (b). Pressure values from each contacting surface are also continuous in Fig. 6.20 (b), although the values are insignificantly small. For the derived quantities such as normal stress and relative fluid velocity, however, a much greater discrepancy is observed near the singular point. This is explained in the next paragraphs.

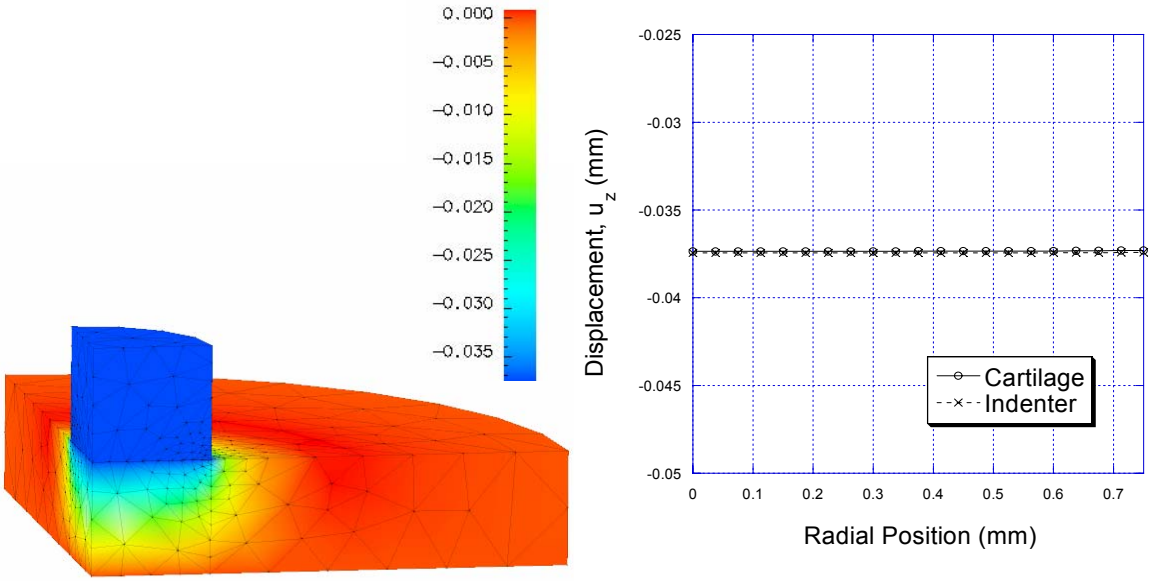

(a) (b)

Figure 6. 19 (a) Displacement distribution in mm and (b) comparison of displacement on contact surfaces at 250 sec. in the biphasic indentation test with a flat-ended cylindrical indenter.

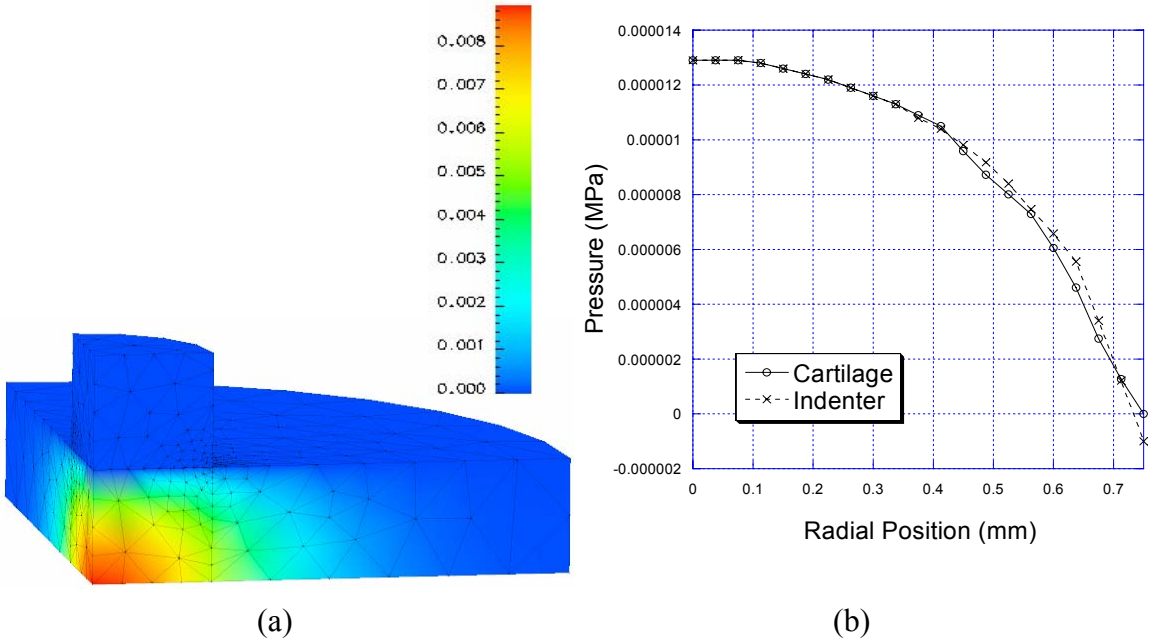

(a) (b)

Figure 6. 20 Pressure distribution in MPa and (b) comparison of pressure on contact surfaces at 250 sec. in the biphasic indentation test with a flat-ended cylindrical indenter.

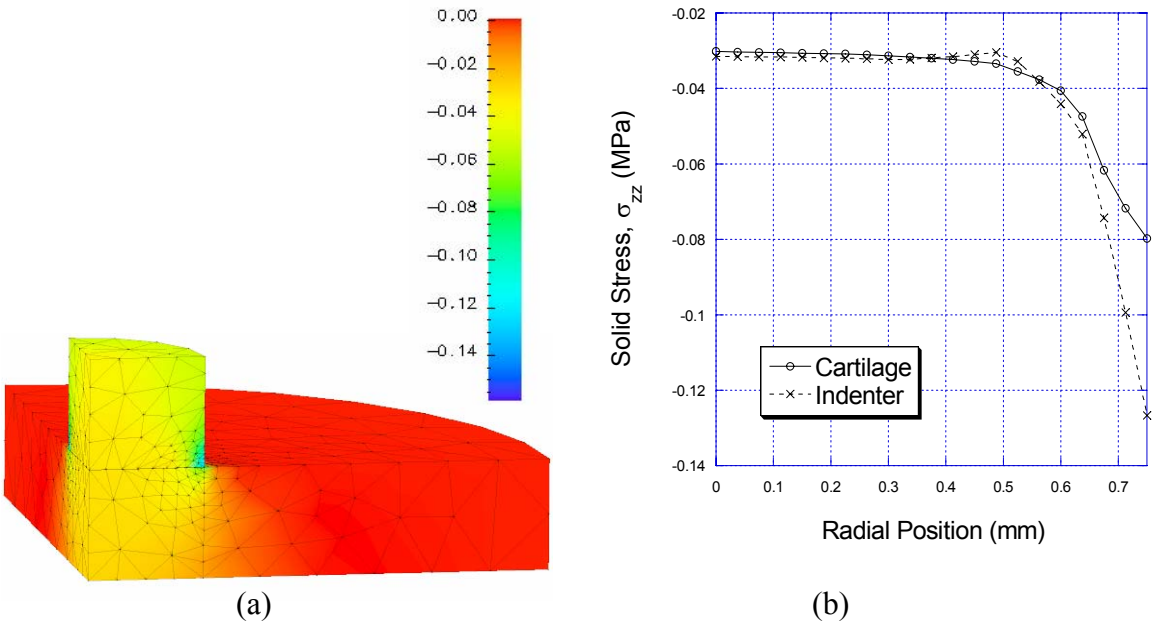

Figure 6. 21 Solid stress σ_{zz}^{s} distribution in MPa and (b) comparison of solid stress on contact surfaces at 250 sec. in the biphasic indentation test with a flat-ended cylindrical indenter.

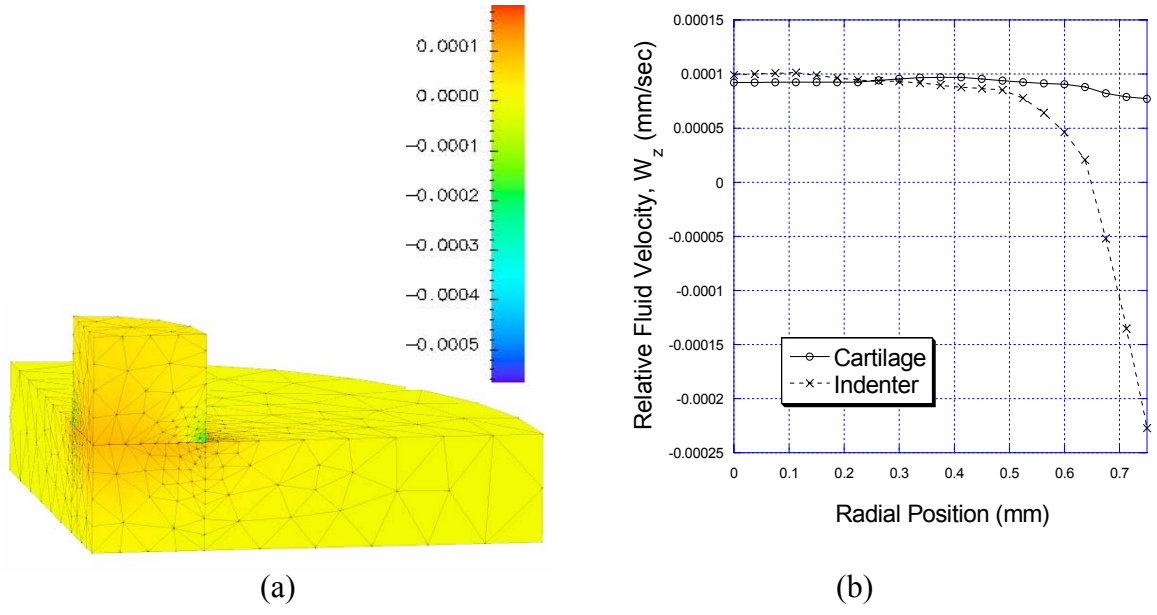

Figure 6. 22 Relative fluid velocity $W_z = -\kappa p_{,z}$ distribution in mm/sec and (b) comparison of relative fluid velocity on contact surfaces at 250 sec. in the biphasic indentation test with a flat-ended cylindrical indenter.

Normal stress and relative fluid velocity are the quantities derived from the gradients of displacement and pressure, respectively. Figure 6.23 (a) shows the displacement, u_z, versus depth at the center and at the edge of contact at 250 sec. from the bottom of the tissue to the top of the indenter. There is an expected displacement gradient discontinuity at the depth of 0.75 mm where the tissue and indenter meet and contact occurs. While the indenter seems to move as a rigid body, a high gradient exists in the cartilage. In Fig. 6.23 (b), the displacements in the indenter are magnified, which reveals a small deformation within the "quasi-rigid" indenter. To satisfy the normal stress continuity in the numerical analysis, the formulation enforces continuity of the product of the displacement gradient (strain) times elastic modulus. For the indenter, the product of a small gradient multiplied by a modulus that is a thousand times bigger than the modulus of the tissue is required to have the same value as the corresponding product for the tissue. Considering the severe discontinuity in Fig. 6.23 (a), the continuity condition should be viewed as reasonably satisfied over most of the contact surface (see Fig. 6.21 (b)). The discrepancy toward the singular point can be reduced with mesh refinement.

The discrepancy of relative fluid velocity continuity near the singular point can be similarly explained. Figure 6.24 shows pressure distribution through the depth at 250 sec. (a) for both the cartilage and the indenter and (b) only for the indenter. Again, considering the large change of pressure gradient at the contact surface, the continuity condition is reasonably satisfied for most of the contact surface (see Fig. 6.22 (b)). But the discrepancy toward the edge of the indenter is more severe than the stress continuity. This is caused by the fact that the prescribed zero pressure on the permeable boundary of

the tissue outside of contact also enforces zero pressure on the outer radial edge of the indenter. Eliminating the zero pressure on the outer edge where the indenter meets the tissue will improve the continuity, as will mesh refinement.

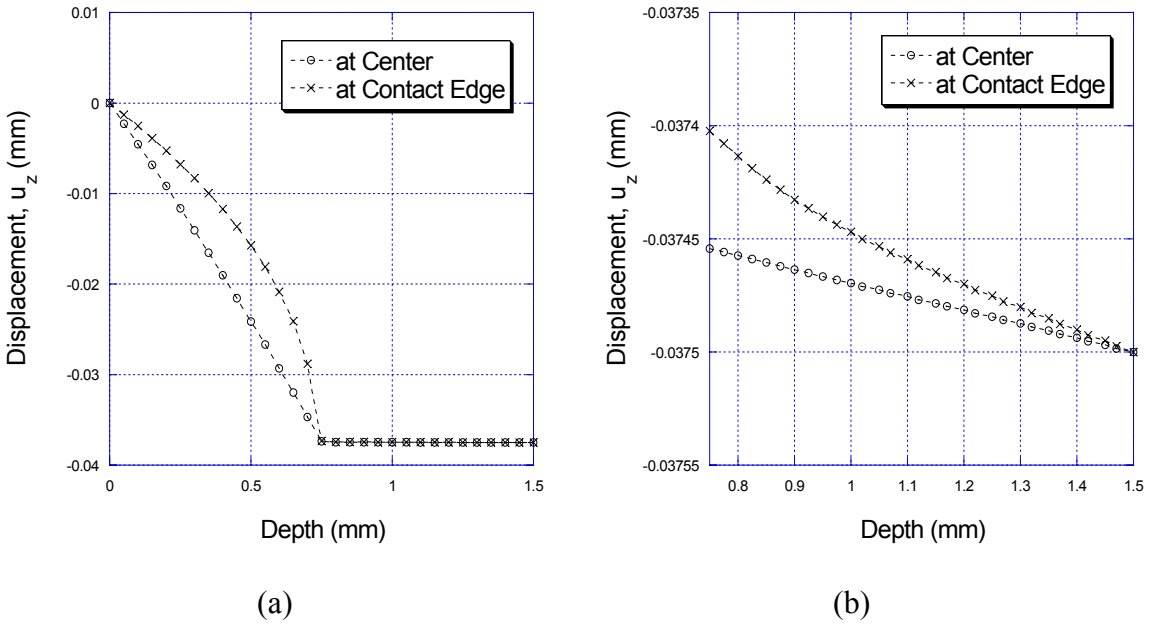

(a) (b)

Figure 6. 23 Displacement through the depth (a) for both the cartilage and the indenter, (b) only for the indenter.

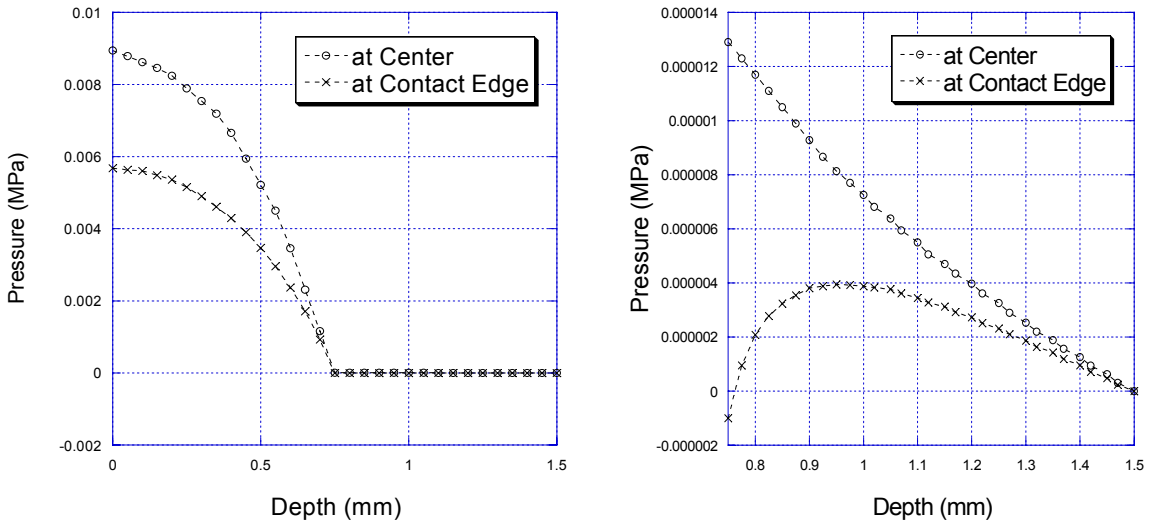

(a) (b)

Figure 6. 24 Pressure through the depth (a) for both the cartilage and the indenter, (b) only for the indenter.

6.5.2 Analysis using with a Cylindrical Ended Indenter

Unlike a flat-ended indentation test, cylindrical-ended indentation involves evolving contact surface. Analytical solutions for this class of biphasic indentation have been developed by Ateshian *et al*. [3], Kelkar and Ateshian [43, 44]. The problem is illustrated in Figure 6.25. The indenter radius is R = 100 mm and the cartilage has the dimensions: w = 20 mm, d = 1 mm and h = 1 mm. The problem domain is discretized with total of 17,871 tetrahedral elements for both the indenter and cartilage, and with 1,008 triangular contact elements on the cartilage surface. Again, there is an initial gap of 0.0001 mm between the indenter and the cartilage, and a fixed boundary condition is applied to the bottom of the tissue instead of explicit modeling of the subchondral bone. The applied vertical displacement increases linearly from $u_z = 0$ at $t = 0$ to $u_z = -0.04$

mm at $t = 100$ sec., and then held. Based on contact search results, pressure is set to zero outside of contact surface. The material properties for the cartilage are E^A = 0.5 MPa, ν^A = 0.0, κ^A = 2.0×10^{-15} m^4/N/sec and ϕ^{sA} = 0.5. The properties for the rigid impermeable indenter are: E^B = 500 MPa, ν^B = 0.125, κ^B = 2.0×10^{-18} m^4/N/sec and $\phi^{sB} = 0.99$.

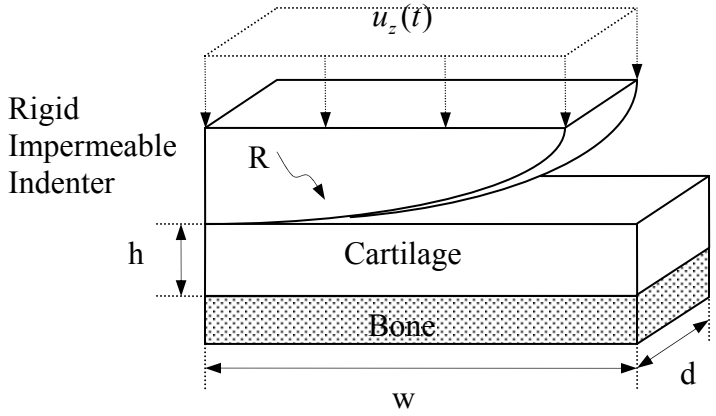

Figure 6. 25 A schematic of the biphasic indentation test with a cylindrical ended indenter.

Figure 6.26 shows (a) displacement on the deformed configuration and (b) the deformed surface, both at 100 sec. The cartilage layer deforms consistent with the rigid motion of the indenter without any inter-penetration. Near the edge of contact surface, large tensile deformation is observed. Figure 6.27 shows the pressure distribution at 100 sec., which is observed to be fairly uniform through the depth. The continuity condition for pressure is satisfied along the contact surface. Pressure falls rapidly to zero outside of contact region.

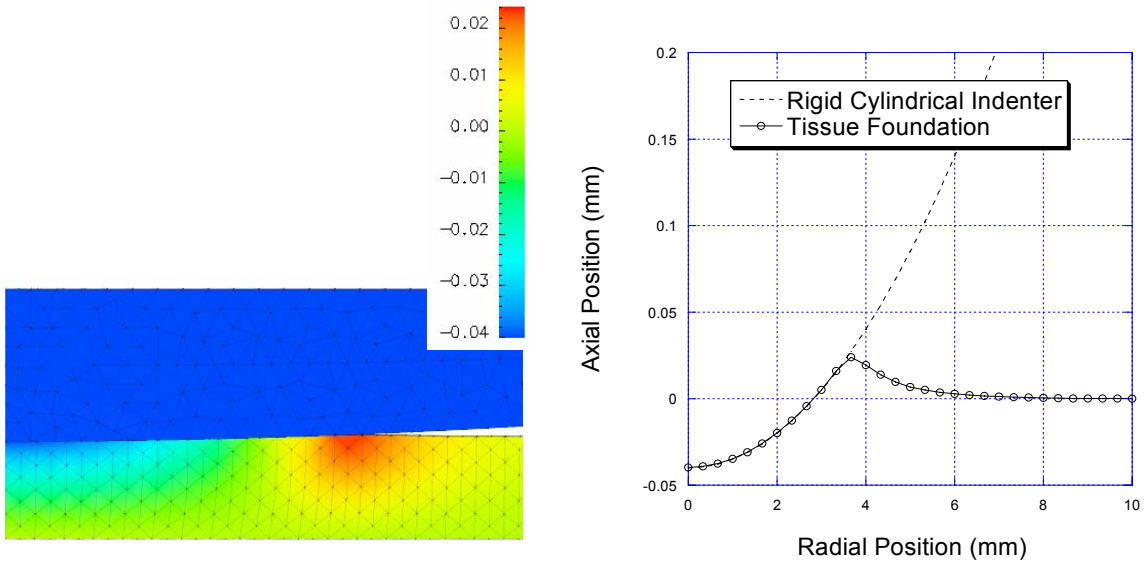

(a) (b)

Figure 6. 26 (a) Displacement (in mm) on the deformed configuration and (b) deformed surface at 100 sec. in the biphasic indentation test with a cylindrical ended indenter.

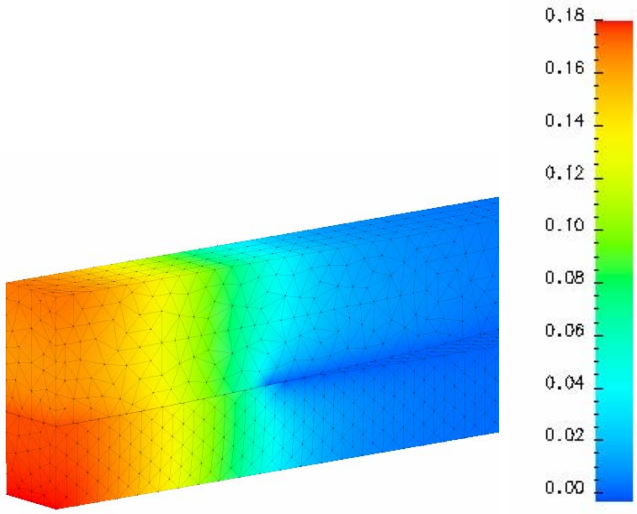

Figure 6. 27 Pressure distribution (in MPa) on the deformed configuration for the biphasic indentation at 100 sec. in the biphasic indentation test with a cylindrical ended indenter.

The normal traction along the contact surface at 100 sec. is depicted in Figure 6.28. It should be noted that the fluid traction is nearly twice the solid traction. This means that the fluid phase takes two times the load on the contact surface than the solid phase even at times as late as 100 sec. As the fluid flow diminishes with time, the load is increasingly supported by the solid phase. Figure 6.29 shows (a) maximum and (b) minimum principal stresses for the solid phase at 100 sec. The cartilage experiences a high compressive stress at the center of the contact surface. However, it is interesting to notice that the peak values of both maximum and minimum stresses are found at the cartilage-bone interface beneath the contact zone.

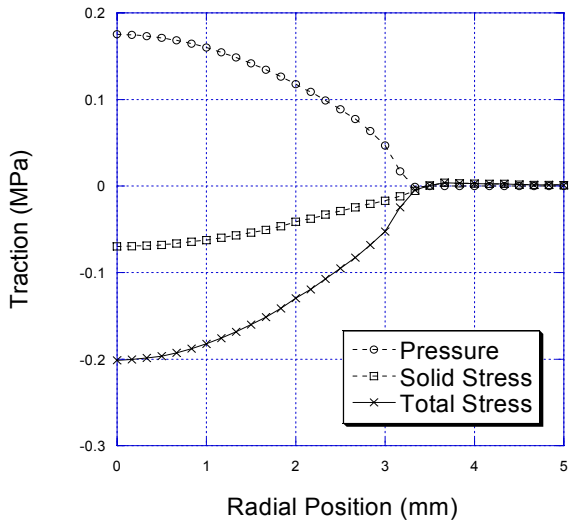

Figure 6. 28 Normal traction distributions (in MPa) at 100 sec. in the biphasic indentation test with a cylindrical ended indenter.

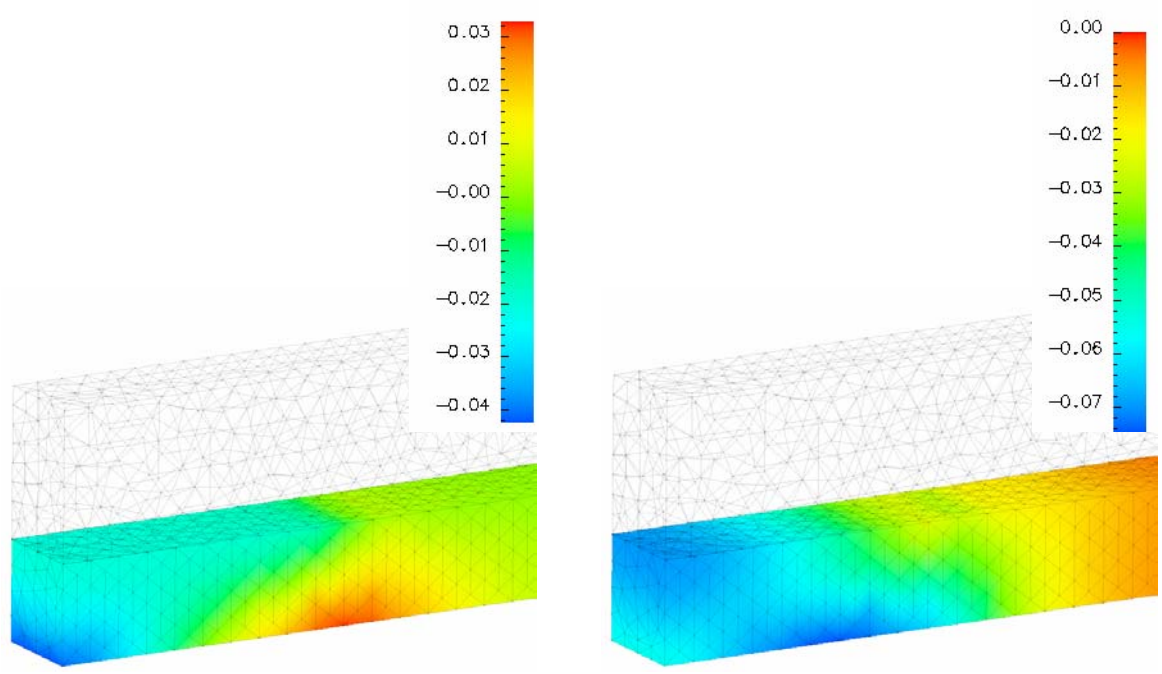

(a) (b)

Figure 6. 29 (a) Maximum and (b) minimum principal stresses in MPa at 100 sec. in the biphasic indentation test with a cylindrical ended indenter.

Results for this problem cannot be directly compared with a mathematical solution due to the evolving contact boundary, but the results do show the same trends observed by Donzelli [18] in a 2D biphasic analysis of a similar problem. Since the biphasic analysis itself has been widely validated on single tissue problems, and the contact continuity conditions are accurately represented, it is concluded that the formulation and implementation produce accurate contact solutions.

6.6 Gleno-Humeral Joint (GHJ) Contact

In previous sections, a series of canonical problems have been used to validate the formulation. Now, it is applied to a physiologically relevant problem, the gleno-humeral joint (GHJ) contact of the human shoulder. Since small changes in joint congruence can cause a crucial impact on the joint mechanics, a precise geometric model is necessary. The anatomy of the joint is shown in Figure 6.30 and quadrants of the glenoid and humeral head cartilage layers are modeled based on the average values of stereophotogrammetric (SPG) data obtained by Soslowsky [74]. The model geometry is discretized with 18,264 biphasic elements for both the glenoid and humerus cartilages, and 700 contact elements aligned with the glenoid surface, which is taken to be the contactor. The geometric and material properties are given in Table 6.1. The subchondral bone is not explicitly modeled. A compressive axial displacement is applied to the humerus-bone interface whose value increases linearly up to 0.2 mm in 10 sec., while the glenoid-bone interface is held fixed. On the contacting faces, zero pressure should be obtained outside of the contact area for free fluid exudation, while the required continuity conditions are satisfied on the contact area.

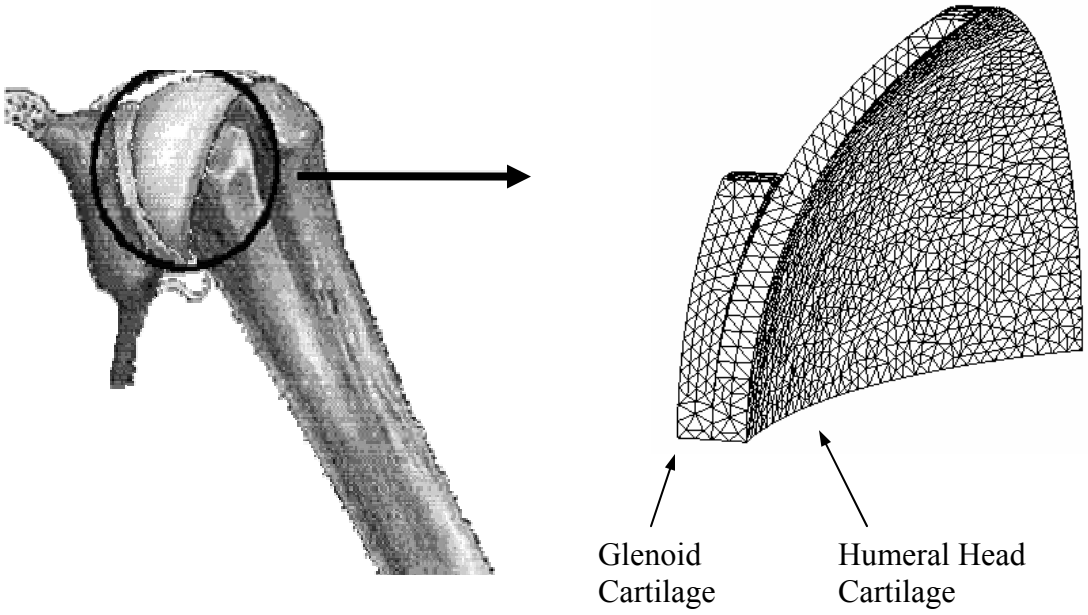

Figure 6. 30 Model geometry and a finite element mesh for glenoid and humeral head cartilages.

	Glenoid	Humeral Head
Contact-Side Radius (mm)	26	23.5
Bone-Side Radius (mm)	34.5	23.5
Thickness at Center (mm)	1.5	1.5
Contact-Side Surface Area (mm^2)	430.13	1427.97
Young's Modulus (MPa)	0.559	0.5565
Poisson's ratio	0.02	0.05
Permeability (m^4/Ns)	1.16×10^{-15}	1.70×10^{-15}
Solid Volume Fraction, ϕ^s	0.2	0.2

Table 6. 1 Geometric and material properties for GHJ.

As soon as the load is applied, the two curved cartilage layers come in contact and the contact surface is developed. Figure 6.31 compares the undeformed mesh with the displacements at 5 and 10 sec. on the deformed geometry. Since there is an initial gap between contacting surfaces, displacement is not continuous. But, the current position is continuous, as required, and no inter-penetration occurs along the contact surface.

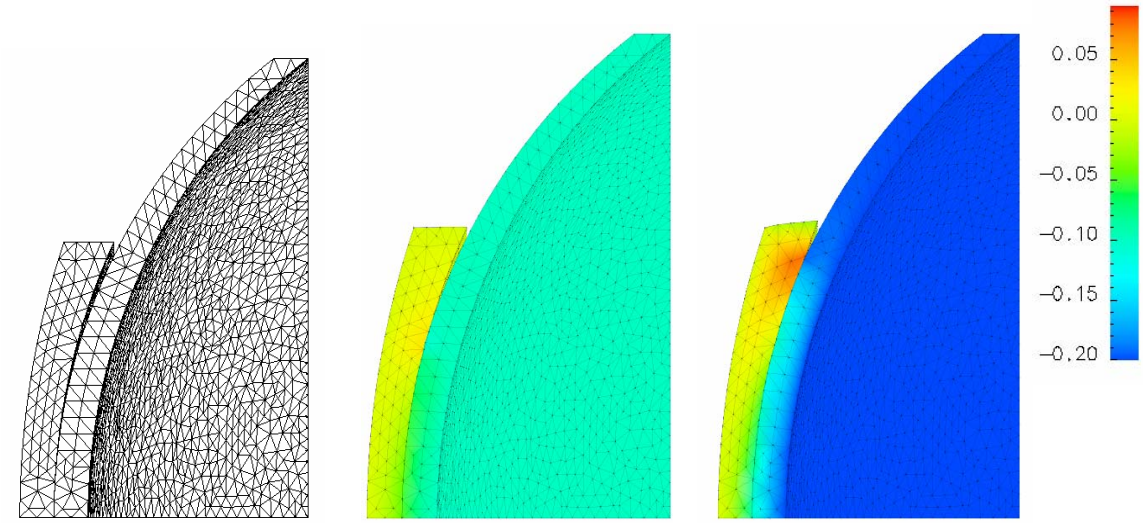

Figure 6. 31 Displacement (in mm) on the deformed geometry in the GHJ at 5 and 10 sec. of 0.2 mm compressive displacement.

Pressure distribution is shown on the deformed configuration at 10 sec. in Figure 6.32. Maximum pressure is found at the center, and decreases towards the edge of contact. Pressure is continuous across the contact area, and zero outside of contact area where the fluid can freely exude. T pressure distributions on the tissue-bone interface for each tissue are also shown to be similar (they are not expected to be the same).

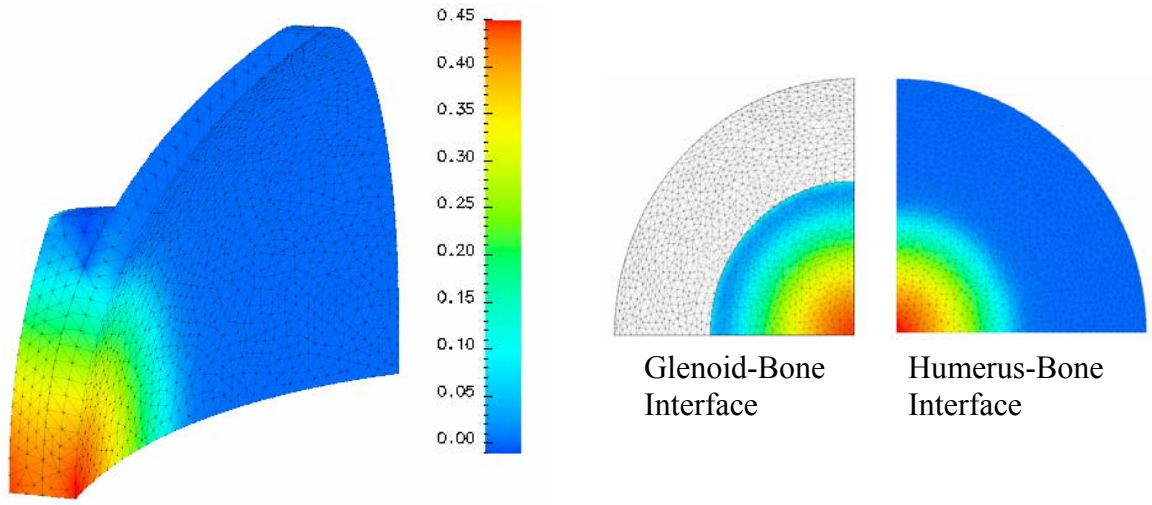

Figure 6. 32 Pressure distribution (in MPa) in the GHJ on the deformed geometry at 10 sec. of 0.2 mm compressive displacement.

Figs 6.33 and 6.34 show the maximum and minimum principal elastic stresses for the solid phase at 10 sec., respectively. Stresses on the cartilage - bone interface for each tissue are compared on right hand side. Since the fluid phase supports a large portion of the load on the contact surface, the solid phase experiences relatively low stresses. Peak values of both principal stresses are found at the cartilage-bone interface, away from the center. These peak values have the shape of a circular band which is smaller than contact radius. The magnitude and shape of both principal stresses are distributed in a similar pattern. The glenoid cartilage experiences peak stresses over a wider area than the humerus cartilage, especially the maximum stress. This observation agrees with an independent axisymmetric contact solution by Donzelli [18].

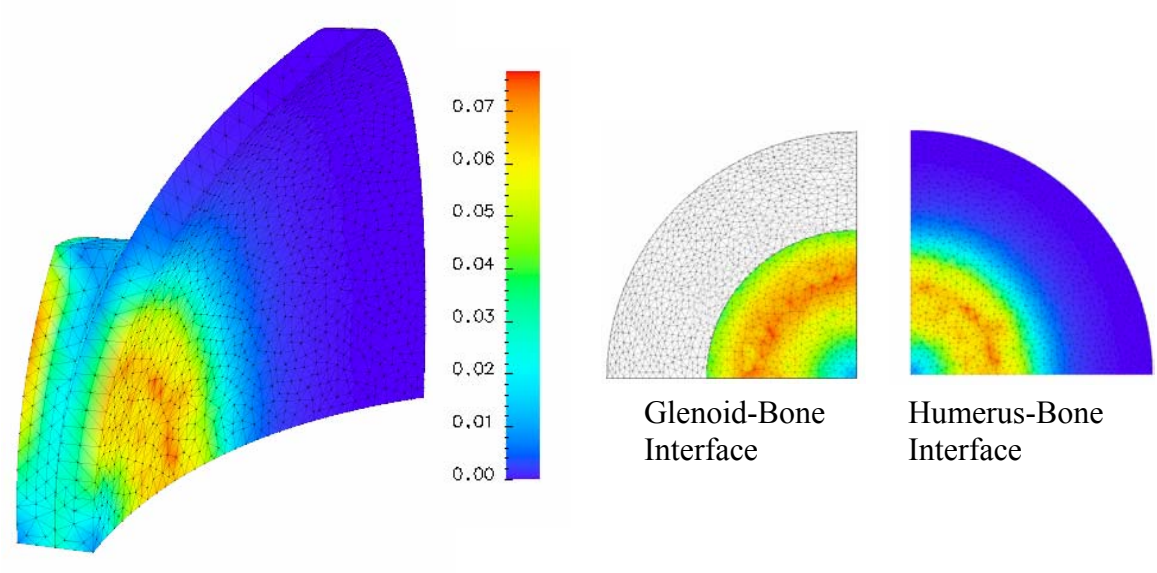

Figure 6. 33 Maximum principal elastic stress in MPa in the GHJ at 10 sec. of 0.2 mm compressive displacement.

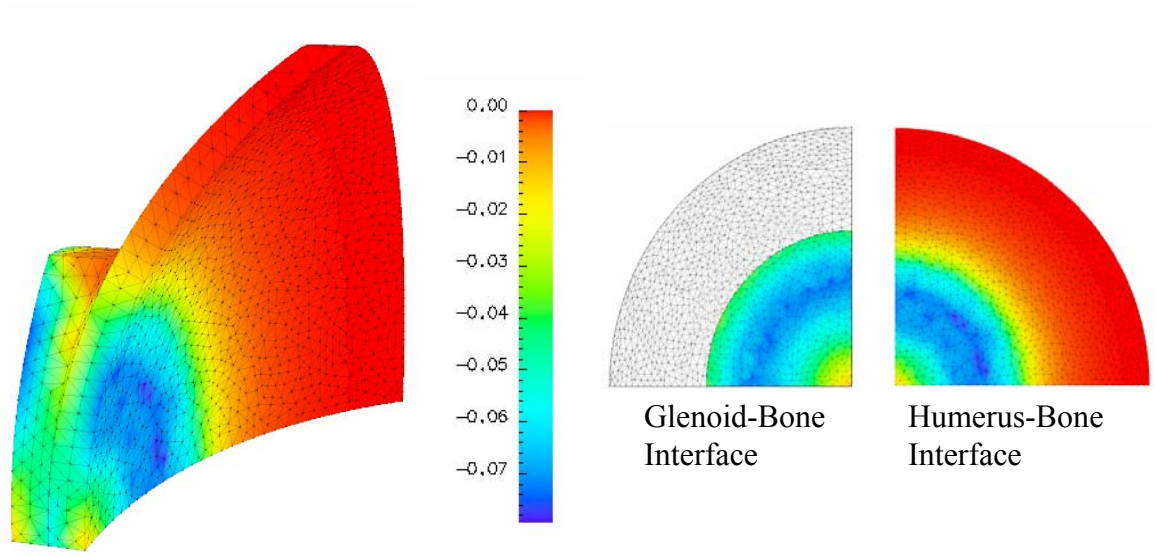

Figure 6. 34 Minimum principal elastic stress in MPa in the GHJ at 10 sec. of 0.2 mm compressive displacement.

Chapter 7: Summary, Concluding Remarks and Future Study

7.1 Summary and Concluding Remarks

A fully three-dimensional finite element formulation has been developed for biphasic contact analysis. For each contacting hydrated soft tissue, the biphasic continuum model [58] has been adopted to describe the tissue as a mixture of solid and fluid phases. The four contact continuity conditions [36] for biphasic tissues have been applied to the assumed contact surface; they insure that both the kinematic and kinetic variables are continuous between the two contacting surfaces. An iterative contact algorithm is independently employed to eliminate physically unacceptable solutions; inter-penetration and tensile contact tractions. The governing equations and boundary conditions are simplified under assumptions that include small deformation, strain-independent permeability, strain-independent phase fraction and frictionless contact.

The Galerkin weighted residual statement is derived based on the velocity-pressure (*v*-*p*) formulation [1], while the contact continuity conditions are enforced using a Lagrange multiplier method. The Lagrange multiplier method is used to enforce two of the four contact continuity conditions, while the other two conditions are introduced directly into the weighted residual statement. Alternate formulations have been examined, differing in the choice of continuity conditions to enforce with Lagrange multipliers. In one they enforce the normal solid traction and relative fluid flow continuity conditions on the contact surface, and in the other the multipliers enforce normal solid traction and pressure continuity conditions. The resulting first order system of equations is

discretized in time using the generalized finite difference scheme. A fully implicit method is used to properly enforce the solid velocity continuity over the evolving contact surface. Symmetry of the global system ensures that the Lagrange multiplier method is equivalent to a variational approach. The problem domain is discretized into the finite elements using a Taylor-Hood element. Ten node tetrahedral elements are used to interpolate a quadratic solid displacement and velocity, and a continuous linear pressure interpolation is defined in terms of pressure degrees of freedom at the four vertex nodes. The formulation has been implemented using an object-oriented language, C++, within a finite element framework, *Trellis* [8].

A biphasic contact patch test has been devised to examine the 3D biphasic contact formulation as a finite element completeness check. The exact transmission of constant normal traction is monitored using continuous and discontinuous interpolations for the Lagrange multipliers. At the same time, enforcement of the four contact continuity conditions is evaluated. When the contact meshes are node-to-node aligned, both continuous and discontinuous functions perform well for the test. The singularity from a fine mesh with discontinuous functions does not significantly deteriorate patch test results. For non-matching meshes, the test results are improved by choosing the finer mesh as the contactor, and with discontinuous functions for Lagrange multipliers.

In an independent study, iterative solvers were extensively tested to efficiently solve the symmetric indefinite systems resulting from the *v-p* formulation where contact boundary conditions are not included. A number of combinations of the preconditioned Krylov subspace methods and matrix reordering techniques are compared. Performance is evaluated based on their convergence rate, number of floating point operations (flops),

computing time, and memory requirements. Overall, the ILU(0) preconditioned BiCGSTAB with one-way dissection reordering performs the best for non-contact problems. As the Lagrange multipliers are introduced to enforce contact constraints, the global linear system becomes symmetric semi-indefinite including zero entities on diagonals. Consequently, the Krylov methods give a totally different performance. The ILU(1) preconditioned TFQMR with reverse Cuthill reordering method shows good convergence performance, while the BiCGSTAB method often diverges for biphasic contact problems.

A series of increasingly complex canonical problems have been used to validate the formulation. For the classical uni-axial compression tests, a single tissue is divided into two pieces and the contact conditions are applied to the known contact boundary. The finite element contact formulation was capable of reproducing the time-dependent analytical solutions of the confined/unconfined compression tests. The contact continuity conditions were precisely enforced at each time step. The contact iterative algorithm has been tested to predict the correct contact area for the evolving contact problem. The contact area and maximum contact pressure showed a good agreement with the Hertz solution. Through the biphasic indentation tests, the contact code showed both capabilities; (i) to find the correct contact surface and (ii) to enforce the continuity conditions on it.

Taken collectively, the results from these tests suggest that the current formulation can be used to solve physiologically realistic problems. As an example, the gleno-humeral joint (GHJ) contact of the human shoulder has been solved using an idealized geometry. The results agreed qualitatively with the those from a 2D mixed-

penalty biphasic contact formulation by Donzelli [18] and with those from a penetration method by Ün [84, 85]. The maximum tensile and compressive stresses occur at the cartilage-bone interface, away from the center of the contact surface.

7.2 Suggestions for Future Study

The ultimate goal of the current study is to characterize the mechanical response of human diarthrodial joint systems throughout numerical simulations. The first fully three-dimensional biphasic finite element contact formulation was successful, but there are certain limitations. Suggestions also arise to improve the formulation both theoretically and numerically. Some of the following suggestions can be readily implemented within the current finite element framework. Others will require a long term investment of time and effort.

Among theoretical aspects, geometric and material nonlinearity should be the first consideration. Sliding contact and large displacements in diathrodial joints cannot be precisely described within the limitation of geometric linearity. Also, consideration of material nonlinearity brings nonlinear constitutive relations; strain-dependent permeability, hyperelasticity of the solid phase, etc. It is possible that the frictional effect on cartilage contact surface may change the overall deformational behavior, but the contribution of friction in most cases should be negligible. If friction is introduced, a modified contact patch test has to be considered to establish the finite element completeness and convergence. As more ingredients are included, the contact treatment methods should also be re-evaluated. For instance, the augmented Lagrange or penalty

method might be more attractive than the Lagrange multiplier method when the global system needs to be updated for nonlinear analysis.

As the computational expense drastically increases for 3D nonlinear analysis, a careful effort is required to reduce the computing time with the limited hardware resources. In the present contact analysis, a large amount of time is being spent in searching contact pairs among the potential contact elements. This process is theoretically straightforward, but numerically costly especially for the refined contact surfaces needed to account for locally high gradients of field variables. Also, the later biphasic contact implementation should include error estimation techniques, as well as *h*, *p* and *h*-*p* adaptivity mesh refinement. Finally, parallel implementation on multiple-processors will become a major part of future research for practical analyses of physiological problems.

References

1. Almeida, E.S., Finite Element Formulations for Biological Soft Hydrated Tissues under Finite Deformation, in Mechanical Engng, Aeronautical Engng and Mechanics. 1995, Rensselaer Polytechnic Institute: Troy, NY.

2. Armstrong, C.G., Lai, W.M., and Mow, V.C., "An Analysis of the Unconfined Compression of Articular Cartilage.," Journal of Biomechanical Engineering, 1984. 106: p. 165-173.

3. Ateshian, G.A., Lai, W.M., Zhu, W.B., and Mow, V.C., "An Asymptotic Solution for the Contact of Two Biphasic Cartilage Layers," Journal of Biomechanics, 1994. 27(11): p. 1347-1360.

4. Axelsson, O., "A Survey of Preconditioned Iterative Methods for Linear Systems of Algebraic Equations," BIT, 1985. 25: p. 166-187.

5. Axelsson, O., Iterative Solution Methods. 1994, New York: Cambridge University Press.

6. Balay, S., Gropp, W.D., McInnes, L.C., and Smith, B.F., Petsc Users Manual. 2001, Argonne National Laboratory.

7. Barrett, R., Berry, M., Chan, T.F., Demmel, J., Donato, J.M., Dongarra, J., Eijkhout, V., Pozo, R., Romine, C., and Van der Vorst, H., Templates for the Solution of Linear Systems: Building Blocks for Iterative Methods. 1994, Philadelphia: Society for Industrial and Applied Mathematics.

8. Beall, M.W. and Shephard, M.S., "An Object-Oriented Framework for Reliable Numerical Simulations," Engineering with Computers, 1999. 15(1): p. 61-72.

9. Belytschko, T. and Neal, M.O., "Contact-Impact by the Pinball Algorithm with Penalty and Lagrangian Methods," International Journal for Numerical Methods in Engineering, 1991. 31: p. 547-572.

10. Benzi, M., Szyld, D.B., and Van Duin, A., "Orderings for Incomplete Factorization Preconditioning of Nonsymmetric Problems," SIAM Journal on Scientific Computing, 1999. 20: p. 1652-1670.

11. Biot, M.A., "General Theory of Three-Dimensional Consolidation," Journal of Applied Physics, 1941. 12: p. 155-164.

12. Biot, M.A., "Theory of Finite Deformations of Porous Solids," Indiana University Mathematics Journal, 1972. 21(7): p. 597-620.

13. Botta, E.F.F. and Wubs, F.W., "Matrix Renumbering Ilu: An Effective Algebraic Multilevel Ilu Preconditioner for Sparse Matrices," SIAM Journal on Matrix Analysis and Applications, 1999. 20: p. 1007-1026.

14. Bowen, R.M., "Theory of Mixtures," in Continuum Physics, Eringen, A.C., Editor. 1976, Academic Press: New York. p. 1-127.

15. Chow, E. and Saad, Y., "Experimental Study of Ilu Preconditioners for Indefinite Matrices," Journal of Computational and Applied Mathematics, 1997. 86: p. 387-414.

16. Cohen, B., Anisotropic Hydrated Soft Tissues in Finite Deformation and the Biomechanics of the Growth Plates, in Mechanical Engineering. 1992, Columbia University: New York, NY.

17. Demmel, J.W., Applied Numerical Linear Algebra. 1997, Philadelphia, PA: SIAM.

18. Donzelli, P.S., A Mixed-Penalty Contact Finite Element Formulation for Biphasic Soft Tissues, in Mechanical Engineering, Aeronautical Engineering and Mechanics. 1995, Rensselaer Polytechnic Institute: Troy, NY.

19. Donzelli, P.S. and Spilker, R.L., "A Contact Finite Element Formulation for Biological Soft Hydrated Tissues," Computer Methods in Applied Mechanics and Engineering, 1998. 153: p. 63-79.

20. Duff, I.S., Erisman, A.M., and Reid, J.K., Direct Methods for Sparse Matrices. 1986, New York: Oxford University Press.

21. Eberhardt, A.W., Lewis, J.L., and Keer, L.M., "Normal Contact of Elastic Spheres with Two Elastic Layers as a Model of Joint Articulation," Journal of Biomechanical Engineering, 1991. 113: p. 410-417.

22. El-Abbasi, N. and Bathe, K.J., "Stability and Patch Test Performace of Contact Discretiazations and a New Solution Algorithm," Computers & Structures, 2001. 79: p. 1473-1486.

23. Freund, R.W. and Nachtigal, N.M., "Qmr: A Quasi-Minimal Residual Method for Non-Hermitian Linear Systems," Numer. Math., 1991. 60: p. 315-339.

24. Freund, R.W., "A Transpose-Free Quasi-Minimal Residual Algorithm for Non-Hermitian Linear Systems," SIAM Journal on Scientific Computing, 1993. 14: p. 470-482.

25. Fung, Y.C., "Biomechanics. Its Scope, History, and Some Problems of Continuum Mechanics in Physiology," Applied Mechanics Reviews, 1968. 21(1): p. 1-20.

26. Fung, Y.C., Biomechanics - Mechanical Properties of Living Tissues. Second Edition ed. 1993, New York: Springer-Verlag.

27. Givoli, D., The Top 10 Computational Methods of the 20th Century, in IACM Expression. 2001. p. 5-9.

28. Golub, G.H. and Van der Vorst, H.A., "Closer to the Solution: Iterative Linear Solvers," in The State of the Art in Numerical Analysis, Duff, I.S. and Watson, G.A., Editors. 1997, Clarendon Press: Oxford. p. 62-92.

29. Hasler, E.M., Herzog, W., Wu, J.Z., Muller, W., and Wyss, U., "Articular Cartilage Biomechanics: Theoretical Models, Material Properties, and Biosynthetic Response," Critical Reviews in Biomedical Engineering, 1999. 27: p. 415-488.

30. Hayes, W.C. and Mockros, L.F., "Viscoelastic Properties of Human Articular Cartilage," Journal of Applied Physiology, 1971. 31: p. 562-568.

31. Hayes, W.C., Keer, L.M., Herrmann, G., and Mockros, L.F., "A Mathematical Analysis for Indentation Tests of Articular Cartilage," Journal of Biomechanics, 1972. 5: p. 541-551.

32. Heinstein, M.W., Attaway, S.W., Swegle, J.W., and Mello, F.J., A General-Purpose Contact Detection Algorithm for Nonlinear Structural Analysis Codes. 1993, Sandia National Laboratories: Albuquerque, New Mexico.

33. Hertz, H., "Uber Die Beruhrung Fester Elastischer Korper," Journal fur Mathematik (Crelle), 1881. 92.

34. Holmes, M.H., "A Theoretical Analysis for Determining the Nonlinear Hydraulic Permeability of a Soft Tissue from a Permeation Experiment," Bull. Math. Biology, 1985. 47(5): p. 669-683.

35. Holmes, M.H., "Finite Deformation of Soft Tissue: Analysis of a Mixture Model in Uni-Axial Compression," Journal of Biomechanical Engineering, 1986. 108: p. 372-381.

36. Hou, J.S., Holmes, M.H., Lai, W.M., and Mow, V.C., "Boundary Conditions at the Cartilage-Synovial Fluid Interface for Joint Lubrication and Theoretical Verifications," Journal of Biomechanical Engineering, 1989. 111(1): p. 78-87.

37. Hou, J.S., Mow, V.C., Lai, W.M., and Holmes, M.H., "Squeeze Film Lubrication for Articular Cartilage with Synovial Fluid," Journal of Biomechanics, 1992. 25: p. 247- 259.

38. Hughes, T.J.R., The Finite Element Method: Linear Static and Dynamic Analysis. 1987, Englewood Cliffs: Prentice-Hall, Inc.

39. Huyghe, J.M. and Janssen, J.D., "Quadriphasic Mechanics of Swelling Incompressible Porous Media," International Journal of Engineering Science, 1997. 35(8): p. 793-802.

40. IBM Corporation, Ibm Visualization Data Explorer, Users Guide. Second ed. 1992, Yorktown Heights, NY: IBM Corp.

41. Irons, B.M. and Razzaque, A., "Experience with the Patch Test for Convergence in Finite Elements," in The Mathematical Foundations of the Finite Element Method with Applications to Partial Differential Equations, Aziz, A.K., Editor. 1972, Academic Press: New York. p. 557-587.

42. Johnson, C., Numerical Solution of Partial Differential Equations by the Finite Element Method. 1987, Cambridge: Cambridge University Press.

43. Kelkar, R. and Ateshian, G.A., "Contact Creep Response between a Rigid Impermeable Cylinder and a Biphasic Cartilage Layer Using Integral Transforms," in 1995 Bioengineering Conference, Hochmuth, R.M., Langrana, N.A., and Hefzy, M.S., Editors. 1995, ASME: New York. p. 313-314.

44. Kelkar, R. and Ateshian, G.A., "Contact Creep of Biphasic Cartilage Layers," Journal of Biomechanical Engineering, 1999. 66: p. 137-145.

45. Kempson, G.E., Freeman, M.A.R., and Swanson, S.A.V., "The Determination of a Creep Modulus for Articular Cartilage from Indentation Tests on the Human Femoral Head," J. Biomech., 1971. 4: p. 239-250.

46. Kwan, M.K., Lai, W.M., and Mow, V.C., "A Finite Deformation Theory for Cartilage and Other Soft Hydrated Connective Tissues," Journal of Biomechanics, 1990. 23: p. 145-155.

47. Lai, W.M. and Mow, V.C., "Drag-Induced Compression of Articular Cartilage During a Permeation Experiment," Biorheology, 1980. 17: p. 111-123.

48. Lai, W.M., Mow, V.C., and Roth, V., "Effects of Nonlinear Strain-Dependent Permeability and Rate of Compression on the Stress Behavior of Articular Cartilage.," Journal of Biomechanical Engineering, 1981. 103: p. 61-66.

49. Lai, W.M., Hou, J.S., and Mow, V.C., "A Triphasic Theory for the Swelling and Deformational Behaviors of Articular Cartilage," Journal of Biomechanical Engineering, 1991. 113(3): p. 245-258.

50. Lipshitz, H. and Glimcher, M.J., "In Vitro Studies of the Wear of Articular Cartilage: Ii. Characteristics of the Wear of Articular Cartilage When Worn against Stainless Steel Plates Having Characterized Surfaces," Wear, 1979. 52: p. 297-339.

51. Luenberger, D.G., Linear and Nonlinear Programming. second ed. 1984, Massachusetts: Addison-Wesley.

52. MacConaill, M.A., "The Function of Inter-Articular Fibrocartilages, with Special References to the Knee and Inferior Radio-Ulnar Joints," J. Anat., 1932. 66: p. 210-227.

53. Mak, A.F., "The Apparent Viscoelastic Behavior of Articular Cartilage-the Contributions from the Intrinsic Matrix Viscoelasticity and Interstitial Fluid Flows," Journal of Biomechanical Engineering, 1986. 108: p. 123-130.

54. Mak, A.F., Lai, W.M., and Mow, V.C., "Biphasic Indentation of Articular Cartilage: Part I, Theoretical Analysis," Journal of Biomechanics, 1987. 20: p. 703-714.

55. Mankin, H.J., Mow, V.C., and Buckwalter, J.A., "Articular Cartilage Repair and Osteoarthritis," in Orthopaedic Basic Science: Biology and Biomechanics of the Musculoskeletal System. 2000, American Academy of Orthopaedic Surgeons.

56. McCutchen, C.W., "Mechanism of Animal Joints," Nature, 1959. 184: p. 1284-1285.

57. Mish, K.D., Herrmann, L.R., and Muraleetharan, K., "A Comparison of Biot Formulation Finite Element Models for Two- and Three-Dimensional Transient Soil Problems," in Symposium on Computational Mechanics of Porous Materials and Their Thermal Decomposition, Salamon, N.J. and Sullivan, R.M., Editors. 1992, ASME: New York. p. 69-79.

58. Mow, V.C., Kuei, S.C., Lai, W.M., and Armstrong, C.G., "Biphasic Creep and Stress Relaxation of Articular Cartilage in Compression: Theory and Experiments," Journal of Biomechanical Engineering, 1980. 102: p. 73-84.

59. Mow, V.C., Holmes, M.H., and Lai, W.M., "Fluid Transport and Mechanical Properties of Articular Cartilage: A Review," Journal of Biomechanics, 1984. 17(5): p. 377-394.

60. Mow, V.C., Kwan, M.K., Lai, W.M., and Holmes, M.H., "A Finite Deformation Theory for Nonlinearly Permeable Cartilage and Other Soft Hydrated Connective Tissues," in Frontiers in Biomechanics, Woo, S.L.-Y., Schmid-Schonbein, G., and Zweifach, B., Editors. 1986, Springer-Verlag: New York. p. 153-179.

61. Nakamachi, E., "A Finite Element Simulation of the Sheet Metal Forming Process," International Journal for Numerical Methods in Engineering, 1988. 25: p. 283-292.

62. Oldenburg, M. and Nilsson, L., "The Position Code Algorithm for Contact Searching," International Journal for Numerical Methods in Engineering, 1994. 37: p. 359-386.

63. Oomens, C.W.J., Van Campen, D.H., and Grootenboer, H.J., "A Mixture Approach to the Mechanics of Skin," Journal of Biomechanics, 1987. 20(9): p. 877-885.

64. Papadopoulos, P. and Taylor, R.L., "A Simple Algorithm for Three-Dimensional Finite Element Analysis of Contact Problems," Computers and Structures, 1993. 46(6): p. 1107-1118.

65. Parlett, B.N., Taylor, D.R., and Liu, Z.A., "A Look-Ahead Lanczos Algorithm for Unsymmetric Matrices," Mathematics of Computation, 1985. 44: p. 105-124.

66. Parsons, J.R. and Black, J., "The Viscoelastic Shear Behavior of Normal Rabbit Articular Cartilage," J. Biomech., 1977. 10: p. 21.

67. Pissanesky, S., Sparse Matrix Technology. 1984, Orlando: Academic Press INC.

68. Poole, A.R., Rizkalla, G., Reiner, A., Ionescu, M., and Bogoch, E., "Changes in the Extra-Cellular Matrix of Articular Cartilage in Human Osteoarthritis," in Trends in Research and Treatment of Joint Diseases, Hirohata, K., Mizuno, K., and Matsubara, T., Editors. 1992, Springer Verlag: Tokyo.

69. Saad, Y. and Schultz, M.H., "Gmres: A Generalized Minimal Residual Algorithm for Solving Nonsymmetric Linear Systems," SIAM Journal on Scientific and Statistical Computing, 1986. 7: p. 856-869.

70. Saad, Y., Iterative Methods for Sparse Linear Systems. 1996, New York: PWS.

71. Saad, Y. and Van der Vorst, H., Iterative Solution of Linear Systems in the 20-Th Century. 1999: Technical Report, Department of Mathematics, University of Utrecht.

72. Simon, B.R., Wu, J.S.S., Zienkiewicz, O.C., and Paul, D.K., "Evaluation of U-W and U-P Finite Element Methods for the Dynamic Response of Saturated Porous Media Using One-Dimensional Models," International Journal for Numerical and Analytical Methods in Geomechanics, 1986. 10: p. 483-499.

73. Sonneveld, P., "Cgs, a Fast Lanczos-Type Solver for Nonzymmetric Linear Systems," SIAM Journal on Scientific and Statistical Computing, 1989. 10(1): p. 36-52.

74. Soslowsky, L.J., Ateshian, G.A., and Mow, V.C., "Stereophotogrammetric Determination of Joint Anatomy and Contact Areas," in Biomechanics of Diarthrodial Joints, Mow, V.C., Ratcliffe, T.A., and L-Y.Woo, S., Editors. 1990, Springer-Verlag. p. 243-268.

75. Soslowsky, L.J., Flatow, E.L., Bigliani, L.U., Pawluk, R.J., Ateshian, G.A., and Mow, V.C., "Quantitation of in Situ Contact Areas at the Glenohumeral Joint: A Biomechanical Study," Journal of Orthopaedic Research, 1992. 10: p. 524-534.

76. Spilker, R.L. and Munir, N.I., "The Hybrid Stress Model for Thin Plates," International Journal for Numerical Methods in Engineering, 1980. 15: p. 1239-1260.

77. Spilker, R.L. and Maxian, T.A., "A Mixed-Penalty Finite Element Formulation of the Linear Biphasic Theory for Soft Tissues," International Journal for Numerical Methods in Engineering, 1990. 30: p. 1063-1082.

78. Spilker, R.L. and Suh, J.-K., "Formulation and Evaluation of a Finite Element Model of Soft Hydrated Tissue," Computers & Structures, 1990. 35(4): p. 425-439.

79. Spilker, R.L., Suh, J.K., and Mow, V.C., "A Finite Element Analysis of the Indentation Stress-Relaxation Response of Linear Biphasic Articular Cartilage," Journal of Biomechanical Engineering, 1992. 114: p. 191 - 201.

80. Suh, J.-K., Spilker, R.L., and Holmes, M.H., "A Penalty Finite Element Analysis for Nonlinear Mechanics of Biphasic Hydrated Soft Tissue under Large Deformation," International Journal for Numerical Methods in Engineering, 1991. 32: p. 1411-1439.

81. Taylor, R.L. and Papadopoulos, P., "On a Patch Test for Contact Problems in Two Dimensions," in Computational Methods in Nonlinear Mechanics, Wriggers, P. and Wagner, W., Editors. 1991, Springer: Berlin. p. 690-702.

82. Truesdell, C. and Toupin, R.A., "The Classical Field Theories," in Handbuck Der Physik, Flügge, S., Editor. 1960, Springer-Verlag.

83. Truesdell, C. and Noll, W., The Non-Linear Field Theories of Mechanics. second ed. 1992, Berlin: Springer-Verlag.

84. Ün, K., Donzelli, P.S., Spilker, R.L., Wang, V.M., Ateshian, G.A., and Mow, V.C., "Simulation of Biphasic Tissue Contact in the Human Glenohumeral Joint Using Penetration Data," in Proceedings Of1999 Bioengineering Conference. 1999, ASME: Big Sky, MT.

85. Ün, K., A Penetration-Based Finite Element Method for Hyperelastic Three-Dimensional Biphasic Tissues in Contact, in Biomedical Engineering. 2002, Rensselaer Polytechnic Institute: Troy, NY.

86. Varga, R.S., Matrix Iterative Analysis. 1962, Englewood Cliffs, NJ: Prentice-Hall.

87. Vermilyea, M.E. and Spilker, R.L., "A Hybrid Finite Element Formulation of the Linear Biphasic Equations for Soft Hydrated Tissues," International Journal for Numerical Methods in Engineering, 1992. 33: p. 567-594.

88. Wayne, J.S., Woo, S.L.-Y., and Kwan, M.K., "Application of the U-P Finite Element Method to the Study of Articular Cartilage," Journal of Biomechanical Engineering, 1991. 113(4): p. 397-403.

89. Woo, S.L.-Y., Mow, V.C., and Lai, W.M., "Biomechanical Properties of Articular Cartilage," in Handbook of Bioengineering, Skalak, R. and Chien, S., Editors. 1987, McGraw-Hill: New York. p. 4.1-4.44.

90. Yang, C.T., Rubinstein, R., and Atluri, S.N. "On Some Fundamental Studies into the Stability of Hybrid/Mixed Finite Element Methods for Navier-Stokes Equations in Solid/Fluid Mechanics," in Proceedings of 6th Invitational Symposium on the Unification of Finite Elements - Finite Differences and Calculus of Variations. 1982. Univ. of Connecticut.

91. Young, D., Iterative Solution of Large Linear Systems. 1971, New York: Academic Press.

92. Zienkiewicz, O.C., Qu, S., Taylor, R.L., and Nakazawa, S., "The Patch Test for Mixed Formulations," International Journal for Numerical Methods in Engineering, 1986. 23: p. 1873-1883.

93. Zienkiewicz, O.C. and Taylor, R.L., The Finite Element Method. Fourth ed. Vol. I. 1989, London: McGraw-Hill Book Company.